Metal-Nitrogen-doped Carbon (M-N-C) Catalysts for the Direct Electrochemical Reduction of CO_2 to value-added Chemicals and Fuels - Materials, Mechanisms and Cell Performance

vorgelegt von

M. Sc. Wen Ju

ORCID: 0000-0002-6485-1133

von der Fakultät II - Mathematik und Naturwissenschaften

der Technischen Universität Berlin

zur Erlangung des akademischen Grades

Doktor der Naturwissenschaften

Dr. rer. nat.

genehmigte Dissertation

Promotionsausschuss:

Vorsitzender:	Prof. Dr. Michael Gradzielski
Gutachter:	Prof. Dr. Peter Strasser
Gutachter:	Prof. Dr. Yong Lei (TU Ilmenau)

Tag der wissenschaftlichen Aussprache: 09. April. 2019

Berlin 2019

天之道 损有余而补不足

Acknowledgement

I would like to express my first gratitude to my supervisor Prof. Dr. Peter Strasser, not only for the guidance to study my work but also for the opportunity to learn my world.

I also thank Prof. Dr. Yong Lei and Prof. Dr. Michael Gradzielski, the committee of my defense, for the insightful feedback and valuable advice.

Sincere thank goes to Dr. Ana Sofia Varela for mentoring and advising. These make my research strict but interesting. Same appreciation goes to Dr. Alexander Bagger and Prof. Dr. Jan Rossmeisl, your theoretical contribution leads me to search the in-depth answer. Special acknowledge moves toward Prof. Dr. Guang-Ping Hao, partly for the kind collaboration partly for the warm friendship. I am also grateful to Dr. Ilya Sinev and Prof. Dr. Beatriz Roldan Cuenya, for the fantastic ex-situ- and operando- techniques.

I appreciate the CO_2 team partners - Xingli, Tim, Yulin, Trung, Cheonghee and Jorge. Together with you, I am able to over the challenge. I also like to deliver my thanks to Fang, Julian, Mathias and Nate. During my daily learning, you are always important and great. Much enjoy the time with Huan, Xingli, Xiaojia, and Chengyue - the “Entertaining Gang”, you fill the weekdays with a lot of fun.

Further, I would also like to thank Mrs. Annette Wittebrock and Mr. Benjamin Paul for ordering chemicals and lab wares, Mrs. Astrid Müller-Klauke for measuring ICP-OES and Mrs. Andrea Kluge for managing the lab material especially the gas bottles.

I would like to thank everybody at the Strasser’s group for sharing success and happiness. Being one of you is really my luckiness. I also thank the people aid me during my master study. With your help, every difficulty turns easy.

However, real life could not be always breezy. Besides the days with sunshine, man should pass through the days gloomy. I want to thank Weisen, Lebing, and Li, the friends went along with me. You did light the season of my Rhine-Memory.

Importantly, I would like to thank my family - my parents, my wife and Nova my sweety. Always being with me, making me stronger and better than I can be.

Lastly, I am grateful to the China Scholarship Council (CSC) for financing my Ph.D. study.

Table of Contents

Abstract

In the past decades, the surplus of atmospheric CO_2 concentration has drawn tremendous political and scientific attention for its negative impacts, such as the greenhouse effect and ocean carbonation. To mitigate such CO_2 issues, a combination of various strategies is required. The electrochemical CO_2 reduction reaction (CO_2RR) is a promising alternative to convert CO_2 into carbon-based chemicals and fuels, and electricity generated from the renewable sources (solar and wind) could be employed to sustain this transformation. At the current moment, the technological viability of this process is still contingent on finding affordable and efficient catalysts.

In this thesis, a family of catalyst materials composed of abundant elements, in particular, non-precious metals, nitrogen, and carbon, typically referred to as precious group metal (PGM)-free "M-N-C" catalysts, were synthesized and mechanistically investigated – both experimentally and computationally – as catalyst candidates for the CO_2RR. MNC catalysts feature hemoglobin-like single-site metallated porphyrin moieties with great impact on the catalytic reactivity and selectivity of the CO_2RR. Among our studied M-N-C catalysts, the Ni- functionalized one exhibits great efficiency for CO yielding at high potentials and current densities. In particular, employment of Ni-N-C-based gas diffusion electrodes (GDE) combined with micro flow cells, allowed high CO evolution that could exceed 80% faradaic efficiency at 250 mA cm^{-2} current density, outperforming the industry commonly used Ag benchmark. By coupling our experimental observation and density functional theory (DFT) simulation, the reaction path from CO_2 to CO over this sort single site catalyst could be deduced.

Unlike the Ni-N-C catalyst, the Fe-N-C shows selective CO production only at low potentials. Further, due to relatively strong interaction with CO*, it opens the chance for hydrocarbons formation, yet showing little selectivity. To understand the mechanism behind this kind of selectivity, we carried out a series of studies, discussing catalytic tests, in-operando spectroscopic analysis, and computational modeling. Towards material research, operando-XAFS measurements identified an unusual Fe-N_3, possibly a Fe^{I}-N_3 state, which appears to enable CH_4 evolution. Further mechanistic studies included the electrocatalytic reduction of CO and CH_2O as possible reactive intermediates for CH_4 production. By combining the experimental and computational results, we suggest a reaction network for CO_2 reduction into a variety of carbon-based products over the Fe-N-C catalyst. This contributes to the overall mechanistic understanding of CO_2RR over the M-N-C catalysts and delivers perspectives to evolve and design novel catalysts to produce hydrocarbons of high value.

Zusammenfassung

In den letzten Jahrzehnten ist die atmosphärische CO_2 Konzentration deutlich angestiegen. Wegen seiner negativen Auswirkungen bzw. dem Treibhauseffekt und Versauerung der Meere, zog dieser CO_2-Anstieg enorme politische und wissenschaftliche Aufmerksamkeit auf sich. Um diese CO_2-Problematik zu vermindern, ist eine Kombination verschiedener Strategien vielversprechend. Die elektrochemische CO_2-Reduktionsreaktion (CO_2RR) ist eine potentielle Alternative, um CO_2 in Kohlenstoff-basierte Chemikalien und Kraftstoffe umzuwandeln. Strom aus erneuerbaren Quellen wie Solar und Wind könnte diese Transformation unterstützen. Zum gegenwärtigen Zeitpunkt ist die technologische Durchführbarkeit dieses Verfahrens noch von verfügbaren und effizienten Katalysatoren abhängig.

In dieser Arbeit werden Materialien, die aus häufig vorkommenden Elementen – (Nicht-Edel-) Metall, Stickstoff und Kohlenstoff - (M-N-C) aufgebaut sind, synthetisiert und mechanistisch für und während der elektrokatalytischen CO_2RR untersucht. Dabei beeinflusst das Hämoglobin-ähnliche „Single-Site“ Metall-Stickstoff-Zentrum die katalytische Reaktivität stark. Unter unseren untersuchten M-N-C-Katalysatoren zeigt der Nickel-funktionalisierte Katalysator große Effizienz für die CO-Ausbeute bei hohen Potentialen und Stromdichten. Insbesondere die CO-Entwicklung bei einer Gas-Diffusion-elektroden- (GDE-) Micro-Flow-Cell weist einen Faraday’sche Wirkungsgrad von über 80% bei einer hohen Stromdichte von 250 mA cm^{-2} auf. Durch die Verknüpfung unserer experimentellen Beobachtungen und einer Dichtefunktionaltheorie (DFT) -Simulation konnte der Reaktionsmechanismus von CO_2 zu CO über diesen Katalysator abgeleitet werden.

Im Gegensatz zu Ni-N-C funktioniert Fe-N-C als CO-selektiver Katalysator im niedrigen Potentialbereich. Aufgrund der relativ starken Wechselwirkung mit CO* eröffnet sich außerdem die Möglichkeit der Bildung von Kohlenwasserstoffen, die jedoch nur eine geringe Selektivität aufweist. Wir führen daher eine Reihe von Studien durch, um tiefgreifende mechanistische Einblicke in die Reaktionen nach die CO-Bildung, bzw. zu den Kohlenwasserstoffen zu erhalten. Unsere Operando-XAFS-Messungen zeigen einen ungewöhnlichen Fe-N_3-Zustand, wahrscheinlich Fe^{I}-N_3, der für die Methan-Entwicklung selektiv sein könnte. Bei Zwischenproduktstudien führen wir die Reduktion von CO und CH_2O als mögliche Zwischenprodukte für die CH_4-Produktion ein. Durch die Kombination der experimentellen und rechnerischen Ergebnisse haben wir für den Fe-N-C Katalysator ein Reaktionsnetzwerk der CO_2-Reduktion zu verschiedenen Kohlenstoffprodukten aufgebaut. Dies trägt zum mechanistischen Verständnis der CO_2RR für die M-N-C Katalysatoren bei und bietet Perspektiven für die Entwicklung neuartiger Katalysatoren zur Herstellung von Kohlenwasserstoffen.

Die vorliegende Arbeit wurde unter der Leitung von Herrn Prof. Dr. Peter Strasser in der Zeit vom 01.04.2016 bis zum 09.04.2019 im Fachbereich Chemie am Institut für Technische Chemie der Technischen Universität Berlin angefertigt. Die praktischen Arbeiten wurden unter der Leitung von Herrn M.Sc. Wen Ju.

Chapter 1. Introduction and Motivation

The fossil fuels, namely coal, oil, and natural gas, are playing significant roles on the stage of modern human society. For more than half a century, the fossil energy contributes over 80% of the power to allow the prosperity of the modern society, and, will remain as the dominant power source in the coming decades. On the backside of the profit given by the fossil fuels, the CO_2 emission, due to their combustion, causes the drastic anthropogenic greenhouse gas issue, threatening the climate and ecosystem of our planet.[1,2]

To mitigate these carbon issues, while maintaining our current living standard, a great variety of techniques are needed. By cutting to the source of CO_2 emission, gradual transformation towards low-carbon and high-efficiency energy generation, storage and utilization cycle is necessary. In order to replace conventional fossil fuels, sources of renewable energies, as solar and wind are getting considerable attention, focusing on the challenges of efficient conversion and storage. Thanks to the progress in scientific research and production, usage of renewable energies has significantly increased in the past years and is likely going to pose one major power supply in the upcoming decades.

Besides the energy-related strategies, other techniques to directly reduce the CO_2 are also required, which essentially rely on the technological combination of carbon dioxide capture, storage, and conversion. Apart from the importance of the capture and storage techniques, this work focuses on an electrochemical approach to transform the carbon dioxide into carbon-based fuels and manifold chemicals.[3]

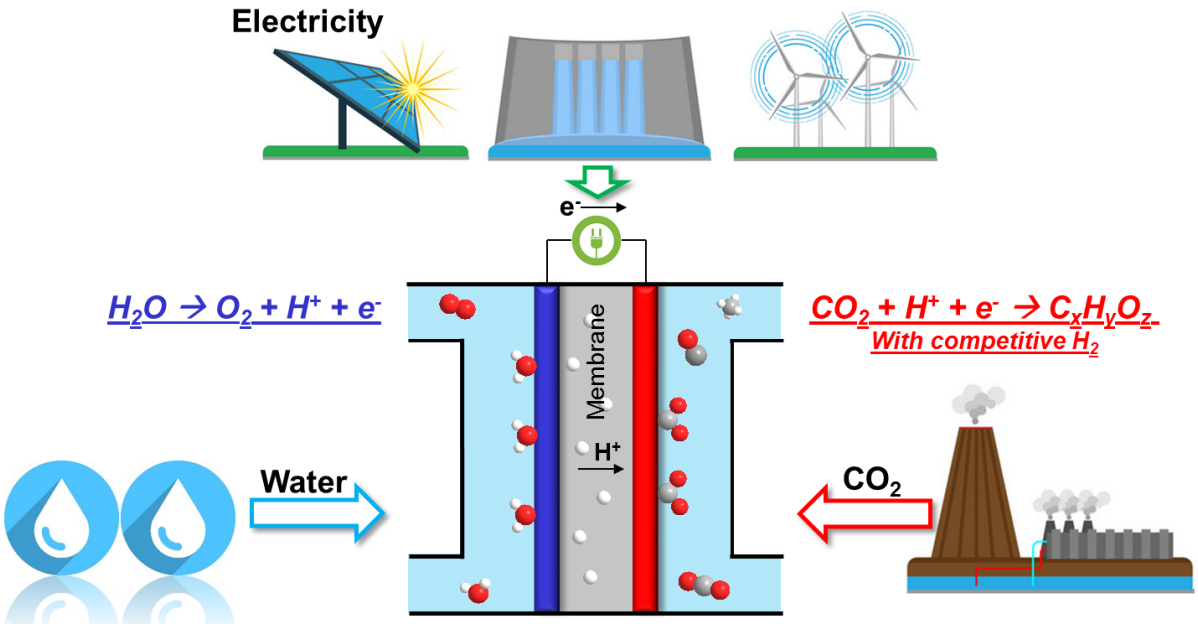

Figure 1- 1 Schematic electrochemical CO_2 reduction accompanied with industrial plants and renewable electricity.

The investigation on electrochemical CO_2 reduction (CO_2RR) could be traced back to 80s last century. Hori et. al. utilized typical metals as the electrocatalysts for CO_2RR and found, this reaction allows to convert waste CO_2 into useful carbon-based chemicals.[4] Technologically, the CO_2RR could be accompanied with industrial CO_2 plants, water, and renewable electricity (see Figure 1-1), which could provide this eco-

beneficial transformation in a sustainable manner. However, knowledge on CO_2 electrolysis is still at a very preliminary stage, and its technologic viability meets multiple distinct limitations. One of the key-factors relies upon affordable, efficient, and scalable catalysts to sustain this electrochemical process, which could be potentially fulfilled by a sort of functionalized carbon materials.

In this dissertation, a novel single site coordinative metal and nitrogen co-doped carbon-based (M-N-C) materials are synthesized and employed as the catalyst for the electrochemical CO_2 reduction. One of the main goals of this work is to determine the relation between the catalytic CO_2RR performance (selectivity / activity) and the nature of the coordinative metal-nitrogen (M-N_x) site. This contribution could 1) help to select the optimal M-N_x active motifs, as well as the operation conditions for CO_2 electrolysis; 2) deliver in-depth mechanistic understanding of CO_2 reduction into CO and other carbon-based products; 3) provide ideas to up-scale the electrolysis to meet the industrial level; 4) offer perspective to evolve and design novel M-N-C catalysts for producing hydrocarbons. This work is structured as follows.

In Chapter 2, the theoretical background and state-of-knowledge of the electrochemical CO_2 reduction are stated. The single site M-N-C catalysts, as well as their function for CO_2RR are discussed. In addition, basic knowledge referred to the synthesis and characterization of the M-N-C catalysts is presented. This section aims to put the results from this work into perspective to the broader scientific context.

In Chapter 3, the experimental procedures of this work, including material synthesis and important physicochemical characterization are listed. Moreover, Online Gas-Chromatograph (Online-GC) test-station for CO_2RR products quantification, equipment as liquid-GC, HPLC for liquid products analysis are shown. Further, the density functional theory (DFT, performed by Prof. Rossmeisl's group at University Copenhagen) calculation method is presented.

In Chapter 4, a fundamental work to determine the impact of the coordinative M-N_x site of the M-N-C catalysts on CO_2RR catalytic reactivity is shown. In this work, five M-N-C catalysts (M: Mn, Fe, Co, Ni, Cu. Materials are synthesized by Dr. Guang-Ping Hao in Prof. Kaskel's group at TU Dresden) were prepared as the catalysts for CO_2 reduction. Experiments, in a homemade H-cell, deliver the faradaic activity / efficiency for CO evolution, whereas DFT calculation predicts the corresponding reaction steps. Correlating the experimental and computational data, we contribute the first-of-its-kind mechanistic insight into the rate- and selectivity- determining processes on the single-site M-N_x centers. We show that the binding energies of intermediates to the M-N_x moieties provide excellent descriptors to describe, predict, and understand the mechanistic details of the CO_2RR activity and selectivity of this family of catalysts over a wide potential range.

In Chapter 5, we utilize a Ni-N-C Gas Diffusion Electrode (GDE) combined Micro-Flow-Cell (MFC) to technologically up-scale the CO_2 electrolysis achieving industry relevant current densities. Unlike the performance in regular H-type cell, the catalyst poses a faradaic efficiency exceeding 80% even at elevated currents of 250 mA cm^{-2}, which result in a partial current of above 200 mA cm^{-2} for CO yielding. This study

displays the potential of the earth abundant and affordable Ni-N-C materials to replace precious metal catalyst in industrial scale electrolyzers for the electrochemical CO_2RR to CO.

In Chapter 6, we perform a special synthesis strategy to improve the site density of the iron-based catalysts, since the Fe-N-C catalyst show superior CO_2RR performance in the low potential range. A secondary chemical N-source is added in the poly-aniline (PANI) derived Fe-N-C, which make the catalyst not only catalytically more active, but allow a variation of the physico-chemical properties of the resulting Fe-N-C materials. Particular emphasis is given to the chemical state and local structure of the coordinative Fe-N_x center during the CO_2 electrolysis. In collaboration with Prof. Roldan Cuenya's group, Operando X-ray absorption spectroscopy is applied to identify the active Fe-N_x motif under the CO_2 electrolysis condition and an unusual Fe(I)-N_3 state is found, which is suggested to be responsible for the formation of CH_4.

In Chapter 7, we further unravel the mechanistic details of CH_4 evolution from CO_2RR over the Fe-N-C catalyst, since it provides the possibility of converting CO_2 into hydrocarbons. Analogous reduction reactions involving distinct reactants, namely, CO_2, CO, CH_2O, CH_3OH and formate, are systematically conducted to investigate the reactivity of these molecules. By linking our experimental results and DFT prediction under consideration of our previous results, we establish a full and deep reaction network from CO_2 into various carbon-based outputs over the Fe-N-C catalyst with clarifying the mechanistic role of the proton in these key reactions.

In Chapter 8, the results of this work are summarized, and general conclusions are drawn. Additionally, perspectives for further investigations on the basis of the findings of this work and their integration into the state-of-knowledge are given.

Chapter 2. Candidates for CO_2RR: from metals to M-N-Cs

In this chapter, the fundamental principles of electrochemical CO_2 reduction are described. First, the reaction mechanism of catalytic CO_2RR is stated. For this, descriptors for the faradaic selectivity are discussed. Thereafter, a sort of novel single-site coordinative M-N-C catalyst as the candidate of CO_2 reduction is introduced. Furthermore, the state-of-art knowledge of M-N-C catalysts preparation, characterization and their application as CO_2RR electrocatalysts are stated.

2.1 Fundamental background

The CO_2 electrolysis, as cathodic reactions, are normally coupled with the electrochemical water splitting (eq. 2-1). Oxygen Evolution Reaction (OER, eq. 2-2) occurs at the anodic side, whereas the Hydrogen Evolution Reaction (HER, eq. 2-3) emerges as a competitive cathodic reaction.

$$2H_2O \leftrightarrows O_2 + 2H_2 \qquad E_0 = +1.23\ V_{RHE} \qquad \text{eq. 2-1}$$

$$2H_2O \leftrightarrows O_2 + 4e^- + 4H^+ \qquad E_0 = +1.23\ V_{RHE} \qquad \text{eq. 2-2}$$

$$2H^+ + 2e^- \leftrightarrows H_2 \qquad E_0 = 0.0\ V_{RHE} \qquad \text{eq. 2-3}$$

To date, a vast range of catalysts, such as metals, metal oxides, metal (oxide) nanoparticles, and molecular catalysts, have been investigated for the electrochemical CO_2 reduction. The first ground-laying work was achieved by Hori et. al.. They pioneered this field by testing a number of metals as the electrocatalysts for CO_2 reduction and found the products distribution of CO_2RR is highly dependent on the nature of the metals.[4] In detail, as well being agreed in other studies, metallic Pt, Fe, and Ni are primarily active for HER (thus should be avoided as the candidate for CO_2RR), while noble metals as Ag and Au could preferentially yield CO as the major product.[4-11] Ultimately, the metallic Cu was particularly interesting due to its unique capability of producing a broader range of carbon-based products (eq. 2.4 to 2.9), including formate, CO, hydrocarbons, and alcohols.[4,12] Therefore, numerous works were implemented on Cu-based catalysts to enhance the yield for value-added products as hydrocarbons and oxygenates. [4,12-25]

$$CO_2 + 2(H^+ + e^-) \leftrightarrows HCOOH \qquad E_0 = -0.17\ V_{RHE} \qquad \text{eq. 2-4}$$

$$CO_2 + 2(H^+ + e^-) \leftrightarrows CO + 2H_2O \qquad E_0 = -0.11\ V_{RHE} \qquad \text{eq. 2-5}$$

$$CO_2 + 8(H^+ + e^-) \leftrightarrows CH_4 + 2H_2O \qquad E_0 = +0.17\ V_{RHE} \qquad \text{eq. 2-6}$$

$$2CO_2 + 12(H^+ + e^-) \leftrightarrows C_2H_4 + 4H_2O \qquad E_0 = +0.08\ V_{RHE} \qquad \text{eq. 2-7}$$

$$2CO_2 + 12(H^+ + e^-) \leftrightarrows C_2H_5OH + 3H_2O \qquad E_0 = +0.08\ V_{RHE} \qquad \text{eq. 2-8}$$

$$3CO_2 + 18(H^+ + e^-) \leftrightarrows C_3H_7OH + 6H_2O \qquad E_0 = +0.09\ V_{RHE} \qquad \text{eq. 2-9}$$

To understand the specific catalytic selectivity of Cu towards hydrocarbons, A.A. Peterson and co-workers utilizes density functional theory (DFT) to simulate the reaction path from CO_2 to CH_4. Their contribution pinpoints that the carboxyl (COOH*) is the first key intermediate of CO_2 reduction into CO (and formate), while the further adsorption and protonation of CO are relevant for hydrocarbons formation, which is allowed on the metallic copper surface.[13] This implies, free energy of COOH* and CO* are crucial factors to determine the reactivities of the CO_2RR candidates.

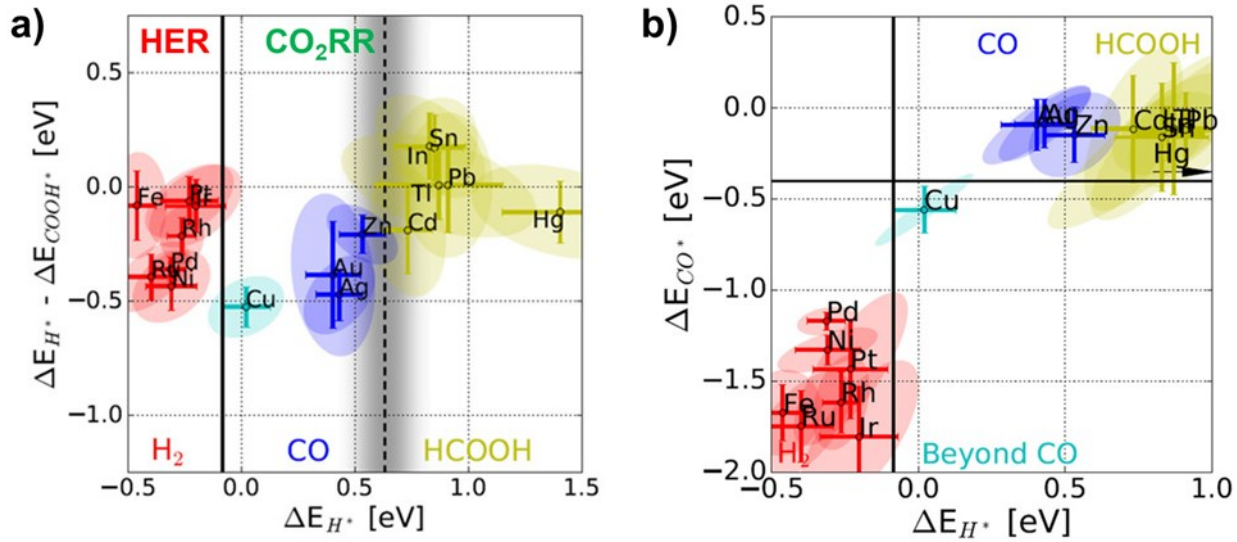

Figure 2- 1 a) The CO_2RR products spectrum classified by ΔE_{H*} descriptor. Metals prefer HER (marked in red) due to strong H* binding (having H_{UPD}), while metals favor CO_2RR owing to weak H* binding (not having H_{UPD}). b) The binding strength diagram of CO* and H*. Hydrocarbons formation occurs via protonation of intermediate CO (CO*), which require moderated binding energy to CO* and H* as Cu. Figures are adapted from reference [15] with the permission of copyright 2017, John Wiley and Sons. Products spectrum is obtained from reference [4].

To further understand other metallic surfaces, establishing a theoretical "selectivity criteria", the adsorption energy of H*, the key intermediate for the competitive HER is taken into consideration. Recently, a computational study was done by Bagger et. al. utilizing the binding strength towards H* as the descriptor to traditionally classify the typical metals into four distinct groups according to their main products, namely, hydrogen, CO, hydrocarbons, and formate.[15] Here, we simply refer them as two general classes, either selective for HER, or for CO_2RR. Figure 2-1a shows the products map as a function of hydrogen binding (ΔE_{H*}). Strong binding towards H* leads to hydrogen underpotential deposition (H_{UPD}), resulting in the HER favoring catalysts. On the contrary, CO_2RR is preferred on the metals with weak H* interaction. Figure 2-1b models the free energy map for hydrocarbons. Based on Peterson's prediction,[13] three critical factors are claimed, 1) proper binding to H* to avoid H_{UPD}, 2) proper binding strength enabling the CO* adsorption while avoiding CO* poisoning, 3) proper binding strength enabling CO* protonation. This leads to a very narrow room to select the hydrocarbons favoring catalyst (the region is marked as "Beyond CO" in Figure 2-1b.[15]

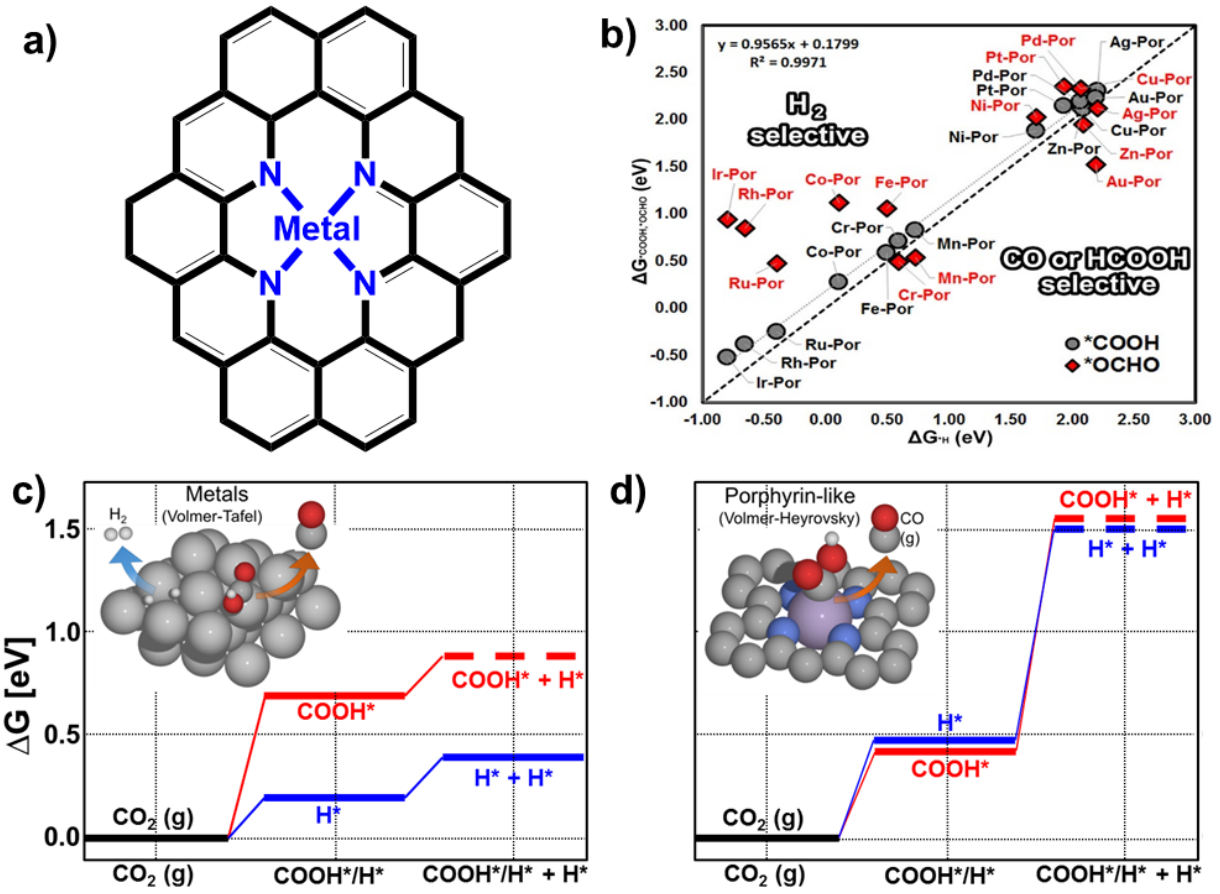

Figure 2- 2 a) Illustration of proposed active M-N_4-C motif. b) Relation between free energy of H* (ΔG_{*H}) and COOH* (ΔG_{*COOH}) (gray circles) as well as H* (ΔG_{*H}) and OCHO* (ΔG_{*OCHO}) (red diamonds) on various metal-Porphyrins. The diagonal line (black dashed) separates selectivity towards HER and CO_2RR (into CO). Figure b) is adapted with permission from [26], Copyright 2017, American Chemical Society. c-d) Free energy diagram of first binding via COOH* (red) or H* (blue) and then binding a second H* at a nearby site for the relevant c) Cu metal surface and d) Fe-porphyrin like motif. Figures are reproduced according to reference [15]. Copyright 2017, Elsevier.

The aforementioned predictions indicate that ΔE_{H*}, ΔE_{COOH*}, and ΔE_{CO*} pose as relevant selectivity criteria of the CO_2 electrolysis, which is also valid to investigate other types of CO_2RR candidates. Recently, a sort of metal functionalized porphyrin-like M-N_x motifs is predicted as the responsible active site for CO_2 reduction. The proposed active M-N_4-C motif is illustrated in Figure 2-2a. Taking these descriptors (binding energies to H*, COOH*, OCHO*, see Figure 2-2b) into consideration, both CO_2RR and HER are allowed on this type catalysts,[26] and the further CO reduction towards various oxygenates and hydrocarbons are predicted in Tripokovic's study.[27] Additionally, in comparison to typical metallic catalysts, the coordinative M-N_x moieties hold the structural advantage to prevent the competitive hydrogen evolution, further benefiting the faradaic selectivity towards CO_2RR (see Figure 2-2 c and d).[15] Above is the preliminary predictions on M-N-C catalysts. We thereby move forward to discuss the practical strategies to investigate this type catalyst.

2.2 The M-N-C catalysts

The metalorganic complex is an optional candidate for CO_2 reduction. Since the 1980s, various complexes, like the metal- macrocyclics,[28] cyclams,[29] bipyridines,[30,31] as well as various porphyrins[32-35] have been reported for their catalytic performance. CO and formate were found as the major product over these molecular catalysts. However, in practice, these molecular complexes are commonly utilized as homo-catalysts or immobilized on the electrode surface, thus suffer the drawbacks such as mass / electron transfer limitation. Their technologic applicability is therefore restricted by low working current densities.[36]

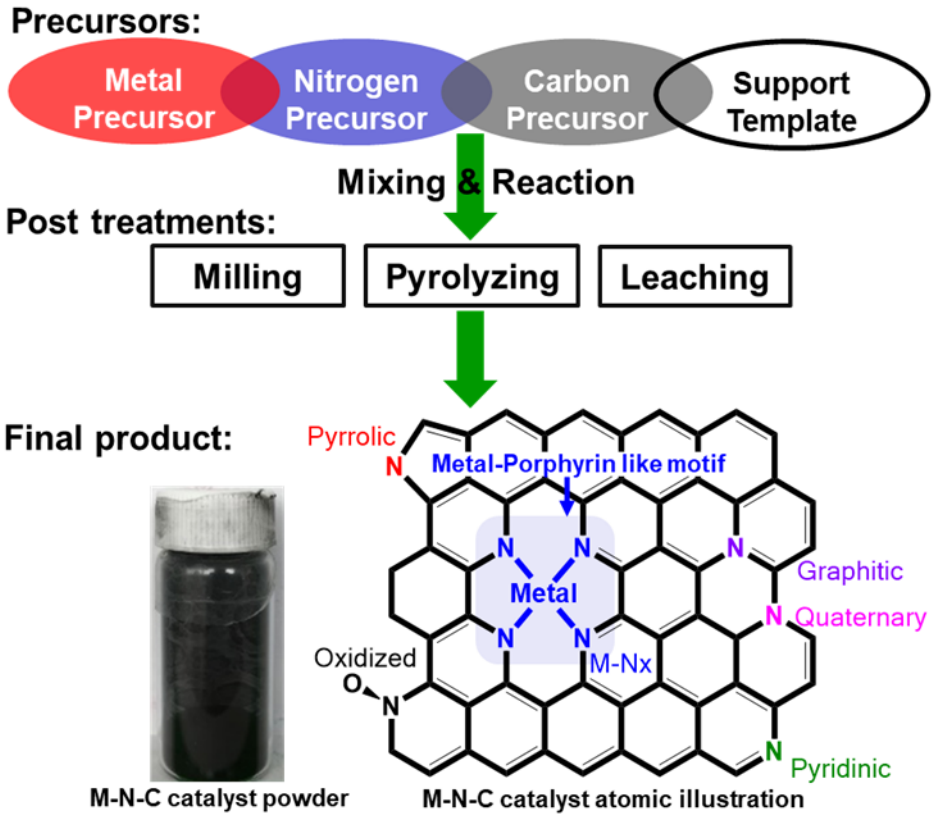

Figure 2- 3 Synthesis strategy of metal nitrogen-doped carbon (M-N-C) catalysts.

Inspired by this metal-contained complexes, a sort metal and nitrogen functionalized carbon (M-N-C) was designed and performs as a promising alternative to the Pt catalyst for oxygen reduction reaction (ORR).[37-42] Recent studies show their potential for CO_2RR utilization.[43,44] Compare to the original metal-complex, these functionalized carbon catalysts own excellent conductivity, large surface, mechanical stability, low-cost and especially good scalability, thus hold the great promise for industrial level applications.[36] Regular synthesis approach of these catalysts generally is shown in Figure 2-3. Usually, by mixing and carbonizing the carbon, nitrogen and metal precursors, man could formulate and embed nitrogen functionalities (including pyrrolic, pyridinic, metal-coordinated, quaternary, graphitic and oxidized ones, see Figure 2-3) in the carbon structure. Other procedures are also of importance during specific synthesis approaches. For instance, using a soft template allows to control the structure and surface area of the final product, accordingly, the leaching procedure is necessary to remove the remaining template material.

In previous studies, the nitrogen coordinated metal ions (M-N_x) are demonstrated as the active sites for CO_2RR,[26,27,43,44] although the metal free N-C catalysts were also reported for their CO_2RR performance.[45,46] In practice, following the normal M-N-C synthesis procedure, various functionalities could exist in the obtained material, such as the inorganic particles and a number of nitrogen moieties (see Figure 2-3). For the purpose to identify the coordinative M-N_x motifs that we expect, a combination of characteristic methodologies is required. Based on the state-of-knowledge, the X-ray absorption spectra (XAS, including XANES and XAFS, usually performed in synchrotron facilities for intense and tunable beam source) is able to accurately determine the electronic structure of the matter. To characterize the M-N-C catalysts, the coordination number and bond distance could be analyzed. Reported in previous studies, the XAFS profile of the M-N-C (FeN_4,[42,47] CoN_4[48] and NiN_4[48]) catalysts could nicely match the fingerprint of the porphyrin type references, and coordination number of metal center is roughly 4 with bond-length around 1.93 Å. This confirms that the M-N_x motif is the dominant state of the metal composition. Beside the XAS technique, the X-ray photoelectron spectra (XPS) is more widely used to analyze the state of the sample surface. Recently, Atanassov's group focused on the M-N-C catalysts to address the assignments - electron binding energy (BE) - of various distinct nitrogen functionalities. In particular, the nitrogen 1s electron holding binding energy around 399.7 eV is reported as metal-coordinated ones, which is the evidence of M-N_x motifs.[49,50]

2.3 CO_2RR over M-N-Cs

Previously predicted using the DFT calculations, the metal-porphyrins and porphyrin-like metal-nitrogen motifs in M-N-C catalysts play as the active centers for CO_2 reduction, controlling the intrinsic activity and selectivity.[26,27] However, these simulations remain preliminary, and the free energy of the key intermediates (H* vs. COOH*) strongly scale with each other. Hence, corresponding experimental demonstrations are of high importance, and linking those with the computational trends could deliver in-depth perspectives to achieve practically effective catalysts for CO_2 electrolysis.

Selectivity criteria (HER versus CO_2RR)

On metallic CO_2RR candidates, the binding strength towards H* plays as a key descriptor to determine the catalytic CO_2RR selectivity, since HER occurs as the predominate catalytic process due to H_{UPD}.[15] Towards M-N-C catalysts, such rule also makes sense.

Ju et al. carried out the CO_2 electrolysis on a series pyrolyzed M-N-C catalysts in presence of the first row transition metals (Mn, Fe, Co, Ni, Cu), bringing insight to this issue by combining their experimental and theoretical investigations (which is in detail described in chapter 4 of this thesis).[51] As found by them, the coordinative Ni-N_x sites, who possess weak interaction with protons, could deny the unwanted HER, further benefiting the selectivity to CO evolution. Thus, among these series catalysts, the Ni-N-C shows the best maximum selectivity for CO_2RR into CO. On the contrary, the cobalt sites with strong H* adsorption, accordingly incline to better HER performance. Others stand in between, and selectivity to CO_2RR order is

given as Ni > Fe > Mn > Co = Cu. In a more recent study, Jiang et al. compared the CO_2RR performance of various M-NG (metal atom coordinated in N doped graphene vacancies) using gas diffusion layer, and the same selectivity trends (Ni > Fe > Mn > Co = Cu) is shown.[52] Hu et al. reported the use of pyrolyzed Fe-, Co- and Ni- functionalized nitrogen-doped porous carbon for CO_2 electrolysis. In particular, selectivity for CO_2-to-CO conversion in water was found to be Ni > Fe ≫ Co.[52] Hence, the interaction to H* could be used as a descriptor to control CO_2RR selectivity, and the superior CO selectivity on Ni-based ones is attributed to prohibited H* binding.

Moreover, Zn based M-N-Cs are also studied, showing impressive CO selectivity. The remarkable CO selectivity of Zn-N_4 motifs might be due to the weak H* interaction since its "E_{COOH*} versus E_{H*}" free energy diagram stands close to that of Ni-N_4 motif with respect to Wannakao's DFT calculation [26] (see Figure 2-2b). Experimentally performed by Yang et al,[53] single site Zn-N_x-C catalyst was prepared by pyrolyzing the mixture of urea and Zn-acetate, and faradaic efficiency to CO could reach 95 % at -0.43 V_{RHE}. Similar performance (FE_{CO} = 91 % at 0.39 V overpotential) was observed on the Zn-N-C catalyst in another work using a different synthesis procedure.[54]

Other transition metal centers have also been tested to expand the knowledge on M-N-C catalysts. Roy et al. synthesized a set of M-N-C catalysts for the CO_2RR, and in this contribution, the transition metals Cu, Mo, Ce, and Pr were studied.[55] Interestingly, the Cu-, Mo- containing catalysts were highly selective to the competing HER process, whereas the Ce-, Pr- based catalysts perform slightly better towards CO production, but provide no advances than their metal free reference one. Furthermore, in Birdja's work, porphyrin-comprised In, Sn and Rh were tested for their CO_2RR performance and formate was found to be the major product.[34]

The Cu-N_x motifs should be specially discussed, since the free energy simulation of copper-nitrogen site could fulfill the binding strength requirements (comparable to Ni-N_x), however, considerable performance was not observed.[51,55,56] This could be presumably attributed to poor chemical stability of the Cu-N_x sites under cathodic conditions, as the d-orbit of Cu^0 / Cu^{1+} / Cu^{2+} is filled by 9 (one SOMO) or 10 (fully occupied) electrons, therefore the ionic copper could be reduced into nano-particles and therefore contribute low reactivity in their studied working potential regime.

Selectivity criteria (towards hydrocarbons)

Methane could also be formed over M-N-C catalysts during the CO_2 electrolysis, however, showing extremely low selectivity. In normal reaction conditions (ambient pressure, neutral solution) only Fe- and Mn- based NC catalysts enable the CH_4 production due to strong CO* binding energy[13,27,44,51]. Moreover, it has also been reported the presence of Fe-N_x centers facilitates CH_4 production even in the presence of other heteroatoms.[57] On the contrary, CH_4 evolution is hard to happen on Co-N_4[33] and Ni-N_4[58] sites, since the CO* is more likely to be released due to its weak binding. This is a clear indication that the CO* binding is crucial for methane formation over M-N-C catalyst. Despite Fe-N-C catalysts' ability to produce

hydrocarbons, it should be noticed that the selectivity is dramatically lower than that observed on copper catalysts, which will be discussed in Chapter 7 on the fine structure of these single-site motifs.

Activity descriptor

According to the Arrhenius equation, $k = A * \exp(-Ea/RT)$, the activation energy Ea is the key factor determining the reaction rate at a certain pressure and temperature (applied potential as well). Given that the CO_2 reduction to CO is via the path: $CO_2(g) \rightarrow COOH^* \rightarrow CO^* \rightarrow CO(g)$, thus the free energy of the key transition states, such as COOH* and CO*, could in principle be seen as the descriptor to determine the CO formation activity.[51,56,59]

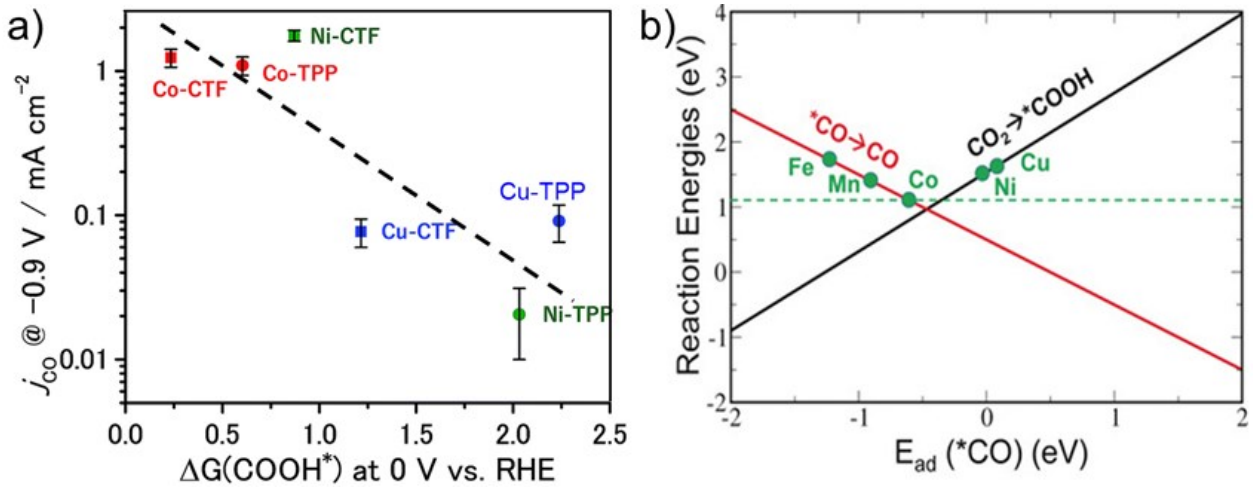

Figure 2- 4 a) Relation of CO formation current densities at -0.9 V_{RHE} and COOH* binding at 0 V_{RHE}. Figure is reproduced from reference[56] with Copyright permission 2018, Royal Society of Chemistry. b) Fitted *CO desorption (*CO→CO, red line) and *COOH formation (CO_2→*COOH, black line) trends as a function of CO* binding energy over all five Metal-Pc electrodes. Figure is adapted from reference [59], Copyright 2018, John Wiley and Sons.

In a recent work carried by Su et. al., two types ligand bases, CTF (covalent-triazine-framework) and TPP (tetraphenylporphyrin), were employed to hold the ionic metal (Co, Ni, Cu) sites for the further CO_2RR utilization.[56] Apart from the ligand effects given by the CTF and TPP, the partial CO formation current densities at -0.9 V_{RHE} clearly elevated when the COOH* binding energy turned stronger, which is an indication that adsorbing the COOH* on the active sites is of high importance to determine the reactivity of CO yielding (see Figure 2-4a). Further in the work done by Zhang et al., binding energy of both CO* and COOH* were taken into account to fit the reactivity of CO_2RR (into CO) over metal phthalocyanines (Pc) complexes (Mn, Fe, Co, Ni, Cu).[59] It is suggested that for Fe-, Mn-, and Co- Pcs, the *CO desorption is the most endergonic step that determines the overall reaction rate for a strong CO* interaction. On the contrary, on Ni- and Cu- Pcs, the *COOH formation becomes the most endergonic and thus limits the overall reaction rate (shown in Figure 2-4b).

The binding energy to COOH* and CO* were evaluated in Ju's work based on a wide range of M-N-Cs (M: Mn, Fe, Co, Ni, Cu, Chapter 4 of this dissertation). In their fitting, three distinct reaction dynamics were found in different potential ranges.[51] In low potential range, the onset of CO evolution relies on the free energy of COOH* transition state. Further in the middle potential regime, the reaction dynamic is controlled by the CO* binding. Finally, in the high potential region, the CO* interaction causes a desorption issue. For this reason, the CO production on Fe-N-C meets a drastic downhill. On the contrary, the Ni-N_x motifs do not suffer the CO* desorption issue, simultaneously denies the competitive HER due to weak H* binding, thus holds the promise as the candidate to selectively yield CO at high overpotentials and current densities.[48,51,52,58,60,61]

Briefly summarizing this section, the binding energies of the active M-N_x motifs towards H*, COOH* and CO* control the faradaic reactivity for CO_2 electrolysis. Weaker H* interaction is beneficial for the CO_2RR selectivity, and relatively strong COOH* binding benefits the activity. In particular, the CO* binding plays a special role during the electrochemical CO_2RR process. It, on one hand provides, the positive effect to boost the dissociation of hydroxide group from COOH* into CO* and further release the CO, but on the other hand turns to a limiting factor, causing the mass transfer issue. The DFT computation also shows that the binding strength of CO* could be tuned by electrode potential. Therefore, not only the catalytic active sites, but the applied potential window should also be taken into account to avoid the CO* desorption barrier.[51,56,58]

Chapter 3. Experiment section

3.1 Synthesis of M-N-C catalyst

The Non-PGM coordinative metal nitrogen functionalized carbon (M-N-C) has been widely utilized for electrochemical CO_2RR in recent years. The general preparation strategy involves 1) mixing and the reaction of the precursors, 2) carbonization (heat treatment) and 3) leaching steps. In this dissertation, two types of synthesis approaches are used to prepare the M-N-C catalysts. CO_2RR study in Chapter 4 is done on copper-MOF derived M-N-Cs, while the works in Chapter 5 to 7 are based on PANI-family. In this section, the respective synthesis procedures of each series catalysts are described in Table 3-1.

Table 3- 1 Amount of chemical substances used in the synthesis protocols to prepare the M-N-C catalysts and the corresponding synthesis protocols for the respective studies described, investigated and discussed later on in Chapters 4-7.

Precursors	Chapter 4	Chapter 5, 6 and 7
Carbon	Co-Bpys derived Cu-Bpys	Ketjen 600
Nitrogen		PANI (2^{nd} Nitrogen is tuned in Chapter 6)
Metal	Mn, Fe, Co, Ni, Cu- Cl_x	$FeCl_3$ ($NiCl_2$ is used in Chapter 5)
1^{st} Heat treat	500 °C for 2 h in Ar	900 °C for 1 h in N_2
1^{st} Acid washing	4M HNO_3 for 24 h	2M H_2SO_4 for overnight
2^{nd} Heat treat	900 °C for 2 h in Ar	900 °C for 1 h in N_2
2^{nd} Acid washing	2M H_2SO_4 for 24 h	2M H_2SO_4 for overnight
3^{rd} Heat treat	900 °C for 2 h in Ar, 1 h in H_2	900 °C for 1 h in N_2
Special Note	N/A	Ni-N-C takes an additional AW-HT

3.2 Physiochemical characterization

Powder X-ray diffraction (PXRD) was employed to analyze the crystallinity of the samples based on the reflection of the ordered lattice. In our contribution, the XRD patterns were recorded on a Bruker D8 Advance instrument with Cu Kα radiation ($\lambda = 1.54056$ Å) in the 2θ range of 10° ~ 90°. Normally, the non-PGM M-N-C catalysts involve no significant ordered crystal phases, thus rarely showing broader diffraction peaks at 25° and 43° for carbon plane (002) and (100), respectively.

N_2 physisorption (BET) measurements using Brunauer–Emmett–Teller (BET) theory are conducted on Autosorb-1 (Quantachome Instruments) to determine the specific surface area of the catalysts. The Pore size distributions were calculated from a nonlocal density functional theorem (NLDFT) pore model based on carbon pores with both slit and cylindrical geometries.

The morphologies of the catalysts were investigated using microscopy techniques. Scanning Electron Microscope (SEM) was done using JEOL 7401F, for resolution between 10 and 100 µm. For higher resolution (5 ~ 50 nm) images, Transmission Electron Microscopy (TEM) was performed using a FEI Tecnai G2 Microscope 20 S-Twin with a LaB6-cathode at 200 kV accelerating voltage (ZELMI Centrum, Technical University of Berlin, carried out by Ms. Xingli Wang). The TEM samples were sonicated in ethanol solution and drop-dried onto Cu-grids and the analysis was done using software from ImageJ.

Inductively Coupled Plasma (ICP) was done to determine the overall metal content in the as-prepared catalysts. 50 mg catalyst powder was firstly dispersed in aqua-regia and then solved using a microwave at 180 °C for 20 mins. The residual mixture was diluted to 50 ml and tested using a Varian 715-ES-inductively coupled plasma (ICP) analysis system with optical emission spectroscopy detection (OES). Elemental Analysis (EA) was used for the determination of bulk elemental distribution (mostly the non-metallic species).

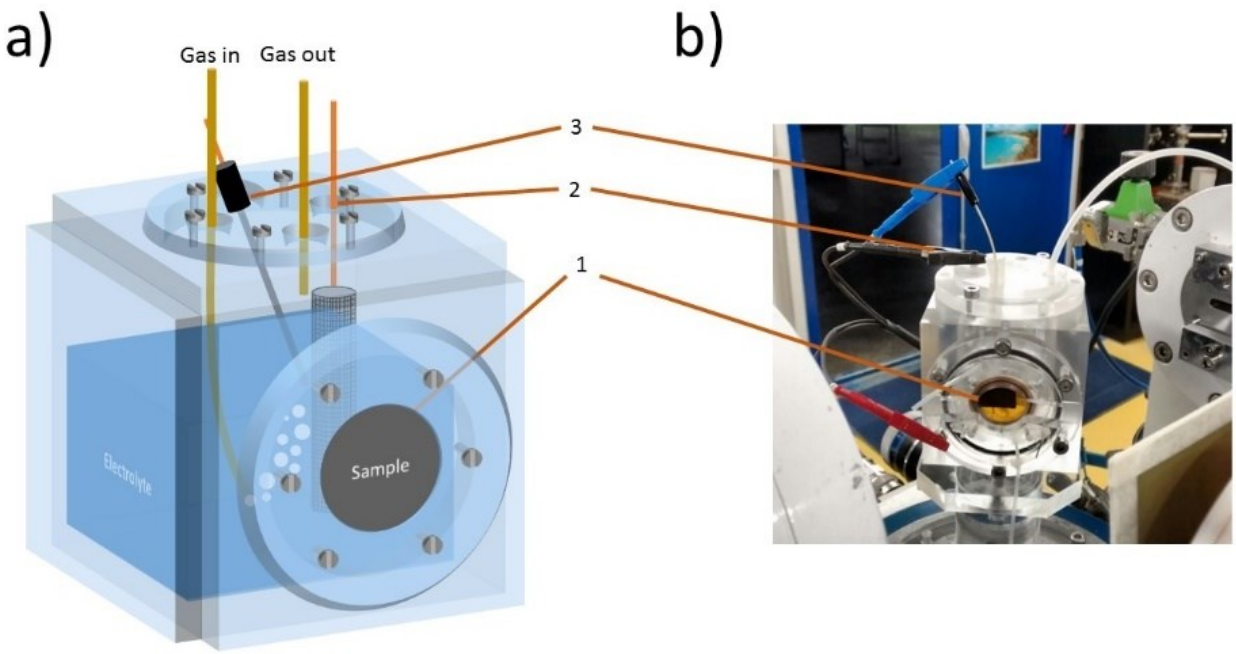

Figure 3- 1 Operando XAS cell used in this work: a) schematic illustration of the cell, 1 – working electrode (GDE with the ink sample) sealed with Kapton tape, 2 – Pt gauze counter electrode, 3 – leak-free Ag/AgCl reference electrode. Designed by Roldan Cuenya's Group at FHI. b) The cell during measurements at SAMBA beamline of SOLEIL synchrotron light source (Paris, France).

X-ray absorption fine-structure (XAFS) spectroscopy is carried in collaboration with Prof. Beatriz Roldan Cuenya's group at Fritz Haber Institute. The data were acquired at the undulator beamline P65 of PETRA III storage ring (DESY, Hamburg, Germany) operating at 6 GeV in top-up mode. All XAS measurements are performed in collaboration with Prof. Beatriz Roldan Cuenya's group at Fritz Haber Institute. The experiments were carried out in transmission mode at the Fe K absorption edge (7112 eV). Operando XAFS measurements were performed in fluorescence mode at the SAMBA beamline of the SOLEIL synchrotron (Saint-Aubin, France) using a 35-element solid-state Ge detector. A home-built operando electrochemical

cell was used, with Pt gauze (MaTek) serving as a counter electrode and a leak-free Ag/AgCl reference electrode (Innovative Instruments Inc, shown in Figure 3-1, built up by Roldan Cuenya Group, FHI). CO_2-saturated $KHCO_3$ was employed as the electrolyte. Raw data reduction was performed using the program Athena.[62] Analysis of extended X-ray absorption fine structure (EXAFS) spectra was conducted in Artemis by using the FEFF8 code to extract the coordination numbers (CN), interatomic distances (r), disorder parameters (Debye-Waller factor, σ^2), and edge energy shift ΔE.[63]

X-ray photoelectron spectroscopy (XPS) was measured in an ultrahigh vacuum (UHV) system equipped with a monochromatic Al Kα source ($h\nu$ = 1486.5 eV) operated at 14.5 kV and 300 W, and Phoibos 150 (SPECS GmbH) analyzer. For each sample, a survey and high-resolution C 1s, O 1s, N 1s, Fe 2p, and S 2p regions were measured. The C 1s signal of graphitic-like carbon was used for binding energy calibration and assigned to 285 eV. The CasaXPS software with pseudo-Voight Gaussian-Lorentzian product functions and Shirley background was used for peak deconvolution. Atomic ratios were calculated from XPS intensities corrected by the corresponding sensitivity factors provided by the manufacturing company (SPECS). In this work, most of XPS analysis was done in collaboration with Dr. Ilya Sinev and Prof. Beatriz Roldan Cuenya.

CO chemisorption measurements were carried out to quantify the Fe-N_x sites per mass of the as-prepared Fe-N-C catalysts (Thermo Scientific TPD/R/O 1110). Each experiment was performed on 100−150 mg of the as-prepared catalyst in helium condition (He flow: 20 ccm). As a cleaning pretreatment step, the sample was heated up to 600 °C and kept for 15 min. After the sample was cooled down to -80 °C, 6 times CO pulses were carried out to perform the CO chemisorption. The CO-uptake mole amount per gram of catalyst obtained from this measurement could be utilized to evaluate the FeN_x site density (μmol g^{-1}) of each Fe-N-C catalyst.

3.3 Electrochemical Methods

Electrochemical characterization methods such as double layer capacitance measurements for Electrochemical Surface Area (ECSA), Potentiostant Electrochemical Impedance Spectroscopy (PEIS), Linear Sweep Voltammetry (LSV) and Chronoamperometry (CA) are of fundamental importance for this work as they allow the evaluation of overall faradaic reactivity of as-prepared materials for during the electrochemical operation.

For electrochemical characterization, an ink was produced containing 15 mg catalyst, 150 µl isopropanol, 800 µl deionized water, and 50 µl 5 wt.% Nafion perfluorinated resin solution (Sigma Adlrich). The ink was sonicated for 8 minutes using an ultrasonic horn, and 50 µl of ink were dropped cast onto a 1 cm^2 glassy carbon electrode resulting in loading of 0.75 mg cm^{-2}. The procedure is presented in Figure 3-2a).

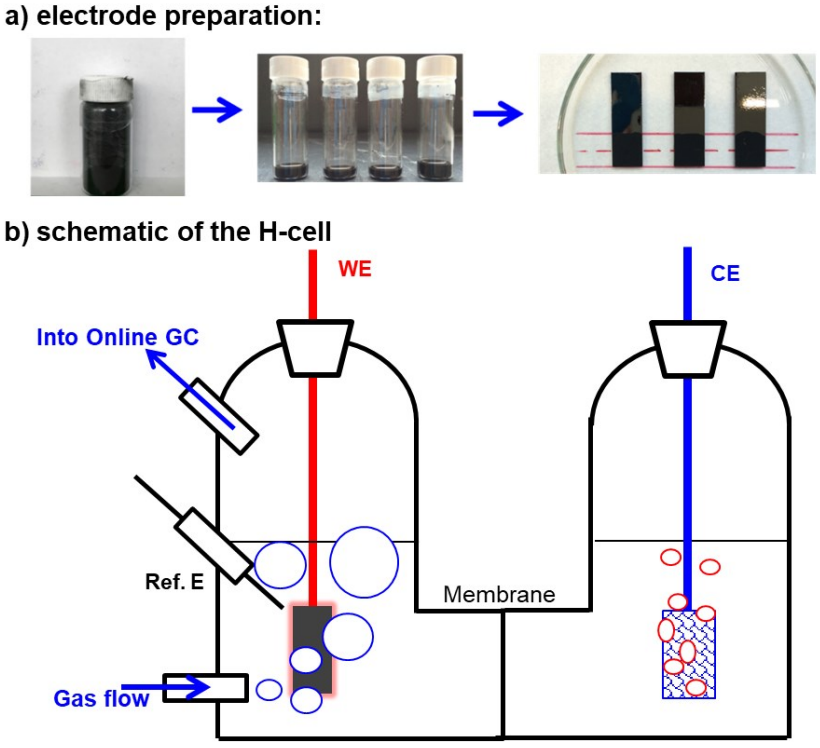

Figure 3- 2 a) Preparation of the electrode: from catalyst powder via ink to layer. Catalyst loading: ~0.75 mg cm^{-2} on GC plate. b) Schematic H-type two compartments cell divided by a polymer membrane. In operation, the CO_2RR as well as other cathodic reactions occur at the WE (working electrode), whereas the OER happens at the CE (count electrode).

The resulting electrode was inserted into a CO_2-saturated, 0.1 M $KHCO_3$ solution. The electrochemical reduction of CO_2 was carried out in a two compartments cell (see Figure 3-2b) divided by a polymer electrolyte membrane (NR212, NR117, and Selemion were used, showing no performance difference). The electrochemical data were acquired using a SP-300 potentiostat (Biologic).

Cyclic voltammetry was firstly carried out on the Fe-N-C catalysts in CO_2-saturated 0.1 M $KHCO_3$ at various scan rates ($\frac{dV}{dt}$, 20 mV s^{-1}, 15 mV s^{-1}, 10 mV s^{-1}, 5 mV s^{-1}, 1 mV s^{-1}) to estimate the double layer capacitance (C_{DL}), which is in principle proportional to the Electrochemical Surface Area (ECSA).

$$j_{DL} = \frac{dQ_{DL}}{dt} = C_{DL} * \frac{dV}{dt} \qquad \text{eq. 3-1}$$

and

$$C_{DL} \propto ECSA \propto BETSA \qquad \text{eq. 3-2}$$

The potential cycling was performed between -0.1 and +0.42 V_{RHE} to avoid the faradaic process. By extracting the double layer current densities (j_{DL}) at +0.16 V vs. RHE (middle of the E scanning range), we were able to quantify the double layer capacitance of each catalyst under electrochemical conditions, see eq. 3-1. In principle, the ECSA should be in agreement with the BET surface area.

A catalyst ink was produced with 15 mg catalyst, 150 µl isopropanol, 800 µl DI water, and 50 µl 5 wt.% Nafion perfluorinated resin solution (Sigma Adlrich). After the dosing and mixing, the ink suspension was sonicated using an ultrasonic horn for 8 minutes. 50 µl of ink were deposited onto glassy carbon with 1 cm^2 area resulting in a catalyst loading of 0.75 mg cm^{-2}. The prepared electrode was inserted into a CO_2-saturated, 0.1 M $KHCO_3$ solution (Honeywell) in a two-compartments home-made H-cell, divided by an anion exchange membrane (Selemion AMV, AGC Engineering Co., LTD). The electrochemical reduction reaction is controlled using a SP-300 potentiostat (Biologic). 50% of the ohmic drop was automatically corrected and the rest was corrected manually (see eq. 3-3). Before the bulk CO_2 electrolysis, a Linear Sweep Voltammetry step (LSV) was performed at the scan rate 5 mV s^{-1} from -0.1 V vs. RHE towards the desired working potential and then kept the potential constant for 60 minutes.

Applied working potential against reversible hydrogen electrode

$$E_{RHE} = E_{Ref} + E_{Ag/AgCl} + 0.059 * pH - R * I \qquad \text{eq. 3-3}$$

E_{RHE}: Working potential against reversible hydrogen electrode/ V_{RHE}
E_{Ref}: Applied potential against the reference electrode / V
$E_{Ag/AgCl}$: Potential of reference electrode measured against normal hydrogen electrode (0.21 V) / V
pH: pH-value of the electrolyte
R: Ohmic resistance between working and reference electrode / Ω
I: Total Current of the experiment / A

Measurements at high current densities were performed by Mr. Tim Möller (TU Berlin) in a commercial Micro Flow Cell (MFC) supplied by ElectroCell. In all Flow-Cell experiments, a commercial Ir-MMO plate (ElectroCell) was used as anode. The catalyst-inks were spray-coated on the microporous layer (MPL) of a Freudenberg C2 gas diffusion layer (GDL) on an area of 3 cm^2 to achieve a catalyst loading 1 mg cm^{-2}.

Nafion (Sigma-Aldrich, 5 wt% resin solution) was used as binder and for ionic conductivity of the catalyst-layer. For usual fabrication of the catalyst inks 15 mg of the M-N-C powders were dispersed with 60 µl Nafion solution in a mixture of Milli-Q water and isopropanol. An aqueous solution of 1 M $KHCO_3$ was used as anolyte and catholyte, which were separated by an anion exchange membrane (Selemion AMV, AGC Engineering Co., LTD.). Both electrolytes were cycled through each respective compartment at 100 mL min^{-1}. The CO2 feed was supplied at rate of 50 mL min^{-1} to the cathode and was flown from the back of the carbon paper through the catalyst-layer. Measurements were performed galvanostatically for two hours at each respective current during the catalytic tests, sweeping the current from low to high values.

3.4 Products quantification

Online gas products quantification. The gas flow was continuously purged into the cell and the exhaust was directly introduced in the Online GC (Shimadzu GC 2014, shown in Figure 3-3) for H-Cell experiments, whereas the catholyte/gas mixture was returned to the catholyte reservoir first, in the Flow-Cell, from where sampling was performed. Gas products were detected at a certain time (using H-Cell) or every 30 min (using Flow-Cell) of bulk electrolysis.

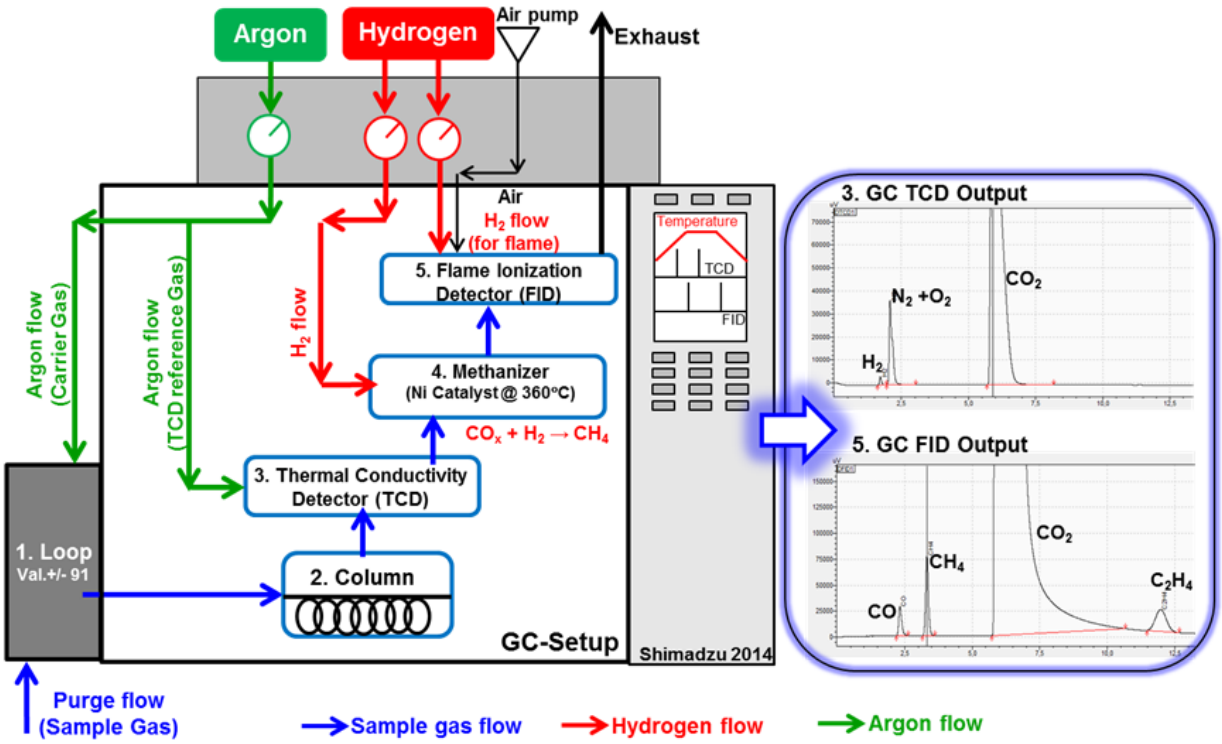

Figure 3- 3 Schematic of online gas chromatograph testing platform. Detailed schematic of each part, 1. Loop valve, 2. Column, 3. Thermal conductivity detector, 5. Flame ionization detector, is displayed in Figure 3-4 below.

During the testing procedure, the gas purge out from the electrolyzer is continuously flowing in the GC, and controlled by a 10-Valve, see Figure 3-4 a and b. At the valve setting "-91", the gas sample fills in, and passes through the Loop (sample loading), and then leaves from the GC setup as exhaust. By setting the Valve from "-91" to "+91", the gas sample in the Loop is carried by the carrier gas argon (sample dosing), flowing into the column for separation. Thereafter, the valve is turned back to "-91" for the next set.

The gas sample, the mixture of various compounds, is carried by the argon flow. Different mobility (due to polarity, mass, and size) leads to different retention time in the column. Usually, small and light compounds like H_2 could pass the column quickly, whereas the larger ones like CO_2, take longer moving in the column. The movements of these three compounds in the column as a function of retention time is illustrated in Figure 3-4c.

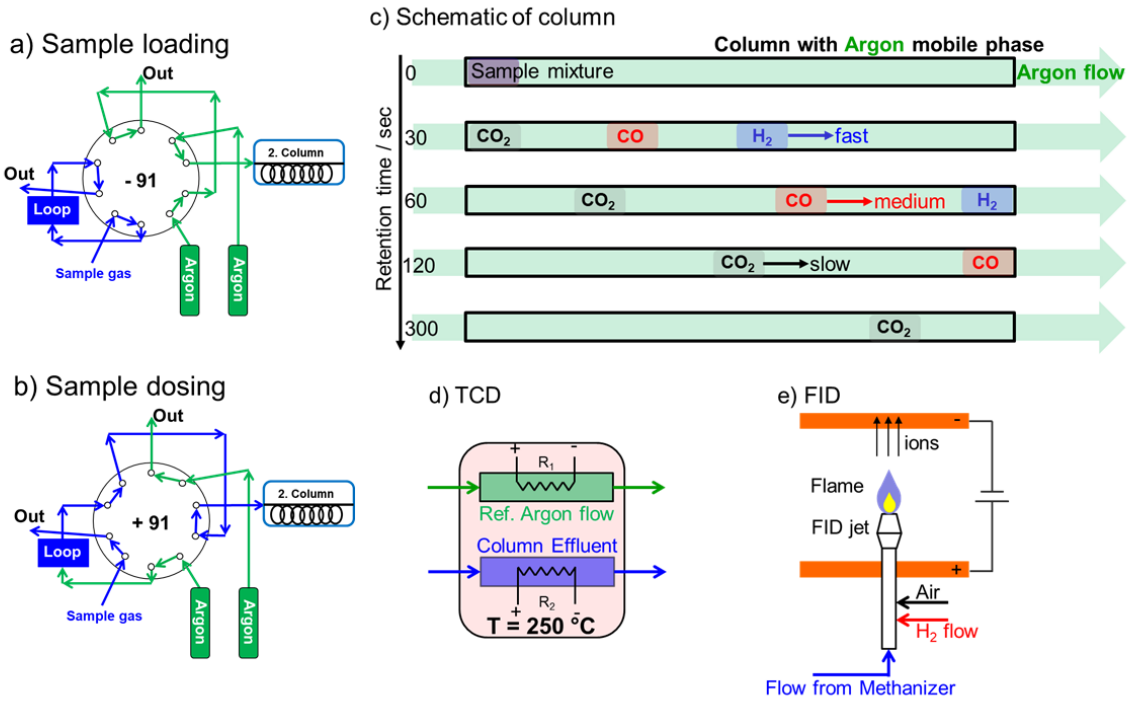

Figure 3- 4 a) and b) Schematic of the 10-Valve for gas sampling in the GC, a) loading the sample in the loop and b) dosing and transporting the loaded sample into the column. c) Schematic of gas sample (mixture of various compounds) carried by Argon flow, flowing in the column (colored in green). For instance, H_2 (blue) with better mobility, moves faster in the column and accordingly takes less retention time, therefore could be detected as the first compound. On the contrary, CO_2 molecules (grey) with lower mobility, suffers longer retention time in the column. Schematic of the detectors e) thermal conductivity detector, and e) flame ionization detector.

Thermal Conductivity Detector (TCD) is equipped to analyze the column effluent by sensing the thermal conductivity changes (marked in blue, shown in Figure 3-4d) using the constant Argon flow as a reference (marked in green, shown in Figure 3-4d). Application of the TCD consists of an electrically heated filament in a temperature-controlled cell. Under normal conditions, the reference Ar flow and Ar carrier gas (as column effluent) flow by the filaments, holding a constant filaments temperature and accordingly constant resistance (R_1 and R_2). Once other gas, like H_2, N_2, and CO_2, exists in the column effluent, the temperature of the filament changes, causing the resistance (R_2) shift, and this resistance change could be sensed by a Wheatstone-bridge, further quantifying the sample amount.

To detect the carbon-based gases, such as the hydrocarbons, a more sensitive detector, flame ionization detector (FID) is applied. As shown in Figure 3-4 e), the gas sample flows through the FID jet and into a flame maintained by the hydrogen and air. The flamed ions could be collected by the electric field, delivering a current signal. It is notable that the FID is rarely available for hydrocarbons and alcohols. To detect carbon-oxygenates (CO or CO_2), a methanizer is needed to first convert them into methane (see part 4 shown in Figure 3-3).

Data given by the GC is the volume percentage of one individual gas compound in the mixture sample purge. Thus, the production rate of each is calculated with eq. 3-4. The respective faradaic efficiency and partial current density are obtained using eq. 3-5 and eq. 3-6.

Reaction rate of gas products

$$\dot{n} = \frac{\dot{V} * C}{A * V_M} \qquad \text{eq. 3-4}$$

$\dot{n}$: Generation rate of the product / mol s^{-1} cm^{-2}

$\dot{V}$: CO_2 gas flow rate / L s^{-1}

C: Concentration of the product detected by GC / Vol%

A: Geometric area of the electrode / cm^{-2}

V_M: Ideal gas molar volume / 22.4 L mol^{-1}

Faradaic efficiency of gas Products

$$FE = \frac{\dot{n} * z * F}{j_{total}} * 100\% \qquad \text{eq. 3-5}$$

$\dot{n}$: Generation rate of the product / mol s^{-1} cm^{-2}

FE: Faradaic Efficiency of the product / %

z: Charge transfer of each product

F: Faradaic Constant / 96500 C mol^{-1}

j_{total}: Total current density during CO_2 bulk electrolysis / A cm^{-2}

Partial current density

$$j_x = FE_x * j_{total} \qquad \text{eq. 3-6}$$

j_x: Partial current density of individual gas product / A cm^{-2}

FE: Faradaic Efficiency of the product / %

j_{total}: total current density / mA cm^{-2}

Liquid products quantification. After a certain period of electrolysis, the remained electrolyte was injected in HPLC (Agilent 1200, Detector: RID, for formate and aldehydes) and liquid GC (Shimadzu 2010 plus, Detector: FID, for alcohols) for liquid products quantification. Faradaic efficiency of each is calculated using eq. 3-7.

Faradaic efficiency of liquid Product

$$FE = \frac{V * \Delta C * z * F}{Q} * 100\% \qquad \text{eq. 3-7}$$

FE: Faradaic Efficiency of the liquid product / %

V: Volume of the electrolyte / L

ΔC: Accumulated concentration of the product detected by HPLC or liquid GC / mol L^{-1}

z: Charge transfer of each product

F: Faradaic Constant / 96500 C mol^{-1}

Q: Total charge transfer during the electrolysis / C

3.5 Density functional theory (DFT) calculation

In this thesis, all theoretical works are contributed by Mr. Alexander Bagger and Prof. Jan Rossmeisl at University Copenhagen. The M-N-C model was created in ASE[64] by a 3 × 5 unit cell of graphene with a functionalized Fe-N_4 site by removing carbon atoms. The outmost carbon atoms were fixed in position and periodic boundaries were applied. Further, the metal (111) model was built by a standard 3 x 3 x 4 slab including a vacuum region and the two lower layers fixed. The electronic calculations were carried out with the GPAW software[65] with the projector augmented wave method, spin polarization (Fe-N-C) and the revised Perdew–Burke–Ernzerhof (RPBE) functional.[66] In detail, the DFT free energy (chemisorption energy) of each species is calculated according to equation 3-8. ΔG_A displays the chemisorption energy of matter A on M surface. E_A and E_M represent the energy of the isolated adsorbate and free surface, whereas E_{AM} stands as the total energy of the adsorbed system.

$$\Delta G_A = E_{AM} - E_A - E_M \qquad \text{eq. 3-8}$$

ΔG_A: Binding energy of A species on M surface / eV

E_{AM}: Total free energy of A species and M surface under adsorption condition / eV

E_A: Free energy of un-adsorbed free A species / eV

E_M: Free energy of clean M surface / eV

We applied a 0.18 grid spacing together with a (2 × 2 × 1) k-point sampling for M-N-C and (3 x 3 x 1) k-point sampling for Cu(111) and all the structure were relaxed to a force below 0.1 eV/Å. The free energy diagrams were calculated using the hydrogen electrode[67] and thermodynamic values from reference.[68] The functional error of the calculated CO_2 RPBE energy was corrected by 0.45 eV together with a -OH water correction of 0.25 eV and a *CO water correction of 0.1 eV.[13]

Chapter 4. Understanding activity and selectivity of metal-nitrogen-doped carbon (M-N-C) catalysts for electrochemical reduction of CO_2

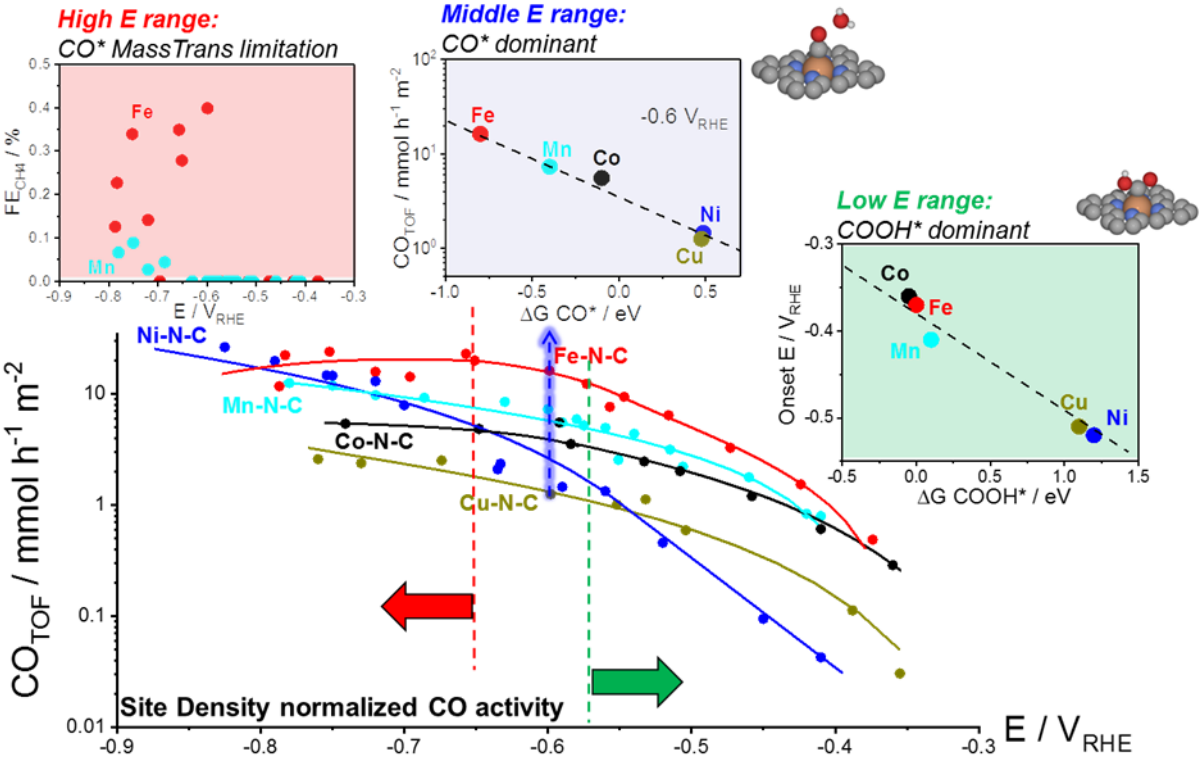

Most parts of this chapter are reproduced from the journal article:

Understanding activity and selectivity of metal-nitrogen-doped carbon catalysts for electrochemical reduction of CO_2

Link: https://doi.org/10.1038/s41467-017-01035-z

with permission from Nature Communications, 2017, 8, 944, as Reference [51] in this dissertation. Copyright 2017 Springer Nature (CC BY 4.0).

Author list: Wen Ju, Alexander Bagger, Guang-Ping Hao, Ana Sofia Varela, Ilya Sinev, Volodymyr Bon, Beatriz Roldan Cuenya, Stefan Kaskel, Jan Rossmeisl and Peter Strasser

Contributions: P.S., W.J. and A.S.V. conceived and designed the experiments. J.R. and A.B. performed the DFT calculation. S.K., B.R.C., G-P.H., I.S. and B.V. carried out the chemical synthesis, microscopic and spectroscopic characterization of the carbon-based materials and subsequent in depth data analysis. W.J. and A.S.V carried out the electrocatalytic tests and analyzed the results. G-P.H., P.S. and W.J. aggregated the figures and co-wrote the manuscript. All authors discussed the results, drew conclusions and commented on the manuscript.

Au and Ag the noble metals showing great performance of selectively producing CO as the major product during the electrochemical CO_2 reduction, however, due to high-cost and low-abundance, the precious metals could hardly be considered as the top-prior candidate for industrial scale investment. Thanks to the progress in Non-Platinum-Group-Metal (Non-PGM) for ORR investigation, a sort of non-precious metal, nitrogen doped carbon (M-N-C) catalysts was designed, exhibiting excellent catalytic property for the fuel cell utilization. Recent studies proof their great potential for CO_2RR, outperforming the Ag/Au candidates in CO yielding. Nonetheless, fundamental understanding in depth is still needed for further catalyst-materials optimization.

In this contribution, we present advances in the understanding of trends in the CO_2 to CO electrocatalysis of the metal- and nitrogen–doped porous carbons containing catalytically active M-N_x moieties (M=Mn, Fe, Co, Ni, Cu). We investigate their intrinsic catalytic reactivity, CO turnover frequencies, CO faradaic efficiencies and demonstrate that Fe-N-C and especially Ni-N-C catalysts rival Au- and Ag-based catalysts. We model the catalytic active M-N_x moieties using Density Functional Theory and correlate the theoretical binding energies with the experiments to give reactivity-selectivity descriptors. This gives an atomic-scale mechanistic understanding of potential-dependent CO and hydrocarbon selectivity from the M-N_x moieties and it provides predictive guidelines for the rational design of selective carbon-based CO_2 reduction catalysts. [51]

4.1 Synthesis and characterization

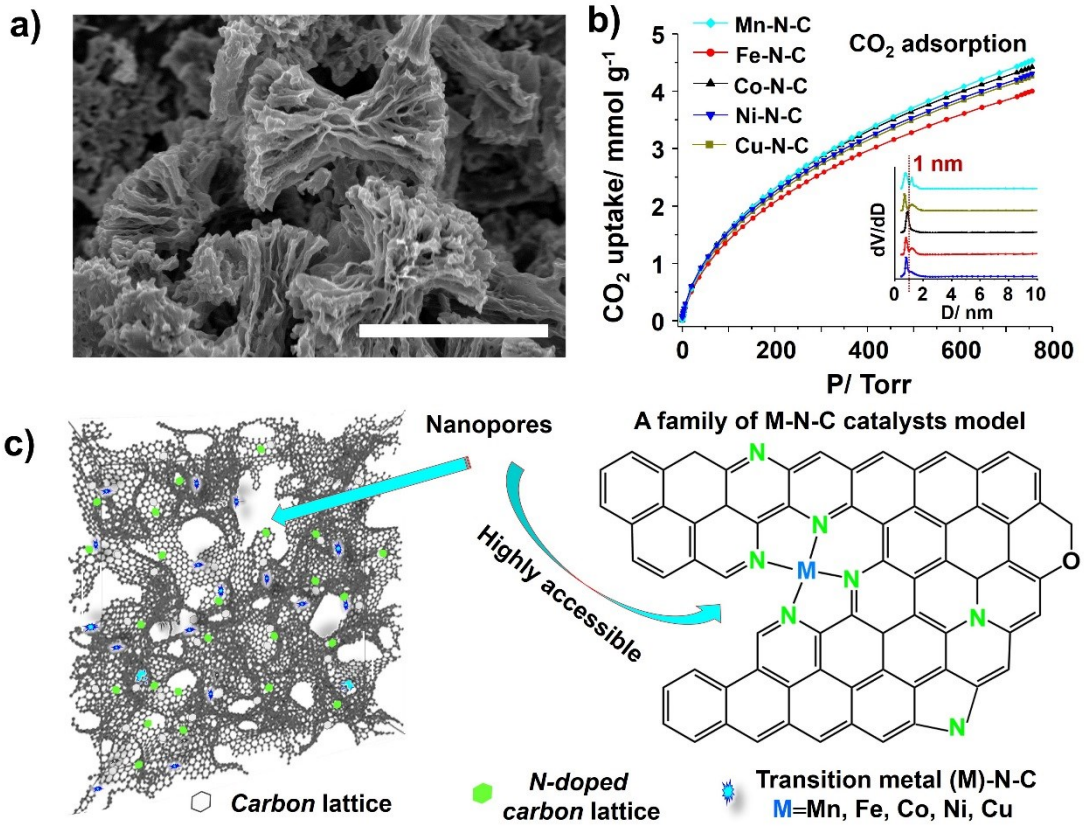

Figure 4- 1 Visualization, porosity and illustration of the M-N-C catalyst. a) Typical SEM image of the family of Nitrogen-coordinated metal-doped (M-N-C) carbon electro-catalysts, scale bar: 4 μm; b) CO_2 physisorption isotherm (273 K); inset: the pore size distribution; c) Materials model and a schematic local structure.

We have synthesized a family of M-N-C electrocatalysts starting with bipyridine-based coordinated polymers and a variety of transition metals such as Mn, Fe, Co, Ni, and Cu. All chemicals were used as received. Typically, 4,4′-Dipyridyl hydrate (bipy, 1.114 g, Sigma-Aldrich Co.) was dissolved in 100 mL ethanol solution. A certain amount of $CoCl_2 \cdot 6H_2O$ (1.2 g) was dissolved in 900 mL DI water solution. Then the bipy solution was mixed with a $CoCl_2 \cdot 6H_2O$ solution and left standing for 24 h without stirring. Then, 50 mL $CuCl_2 \cdot 2H_2O$ (0.1 M) solution was rapidly mixed with the bpy-Co^{2+} solution and aged for 4 h. Subsequently, the resultant product was collected by centrifugation with the speed of 4200 rpm for 12 min. After drying, the polymer product was carbonized at 500 °C for 2 h at a heating rate of 60 °C h^{-1} in Ar atmosphere. Finally, hydrophilic N-doped porous carbons (N-C) with trace amounts of Cu were obtained after leaching in 4 M HNO_3 for 24 h.

Subsequently, additional transition metal species (M=Mn, Fe, Co, Ni) were introduced in N-C through incipient impregnation of MCl_x solutions. The nominal weight concentration of M respective to N-C was set to 25 wt%. The dried M-N-C composite was re-pyrolyzed at 900 °C for 2 h at a heating rate of 2.0 °C min^{-1} in Ar atmosphere. The carbonized M-N-C was dispersed in aqueous sulfuric acid (ca. 2.0 mol L^{-1})

and refluxed at 100 °C for 1 day. The leached sample was collected and washed with DI water until pH value close to neutral. Finally, the leached sample was treated at 900 °C first in Ar for 2 h, and change to H_2 for another 1 h, then change back to Ar, let it cool down and harvest the final M-N-C electrocatalysis (M=Mn, Fe, Co, Ni). The Cu-N-C material was obtained directly after the reductive annealing procedure without any additional acid leaching.

Materials characterization started with morphological and gas adsorption experiments (Figure 4-1a,b). The M-N-C electrocatalysts showed hierarchical chemical structures with visible macropores (Figure 4-1a, Figure S1-1). The pore size distribution peaks narrowly at ca. 0.7-0.8 nm (2.5-2.9 times of the dynamic diameter of CO_2 molecules, Figure 4-1b inset), enabling this family M-N-C materials a remarkable 4.0-4.5 mmol g^{-1} capacity for CO_2 capture at atmospheric pressure (Figure 4-1b) due to their high adsorption potential to trap CO_2 molecules.[69] This could result in CO_2 enrichment within a local environment despite the low CO_2 solubility in the working electrolyte. Figure 4-1c displays a structural illustration of the interconnected macropore walls, composed of thin carbon branches with highly accessible micropores, all over which the coordinated metal sites as well as N-containing carbon lattice are homogeneously distributed.

The N_2 physisorption isotherms (Figure S1-2) are essentially type I for Cu, Co, Ni, or Mn-N-C samples, indicating their microporous nature, while the visible hysteresis of Fe-N-C material reveals the presence of a small fraction of mesopores in addition to micropores. Notably, a significant increase of gas uptake was observed at higher relative pressure (P/P_0>0.9) for all M-N-C samples, indicating their rich macroporosity, which is consistent with the SEM images (Figure 4-1a). The specific surface area based on Brunauer–Emmett–Teller (BET) theory is in range of 615-938 m^2g^{-1}, while the Ni-N-C and Mn-N-C show the lowest and the highest BET surface area, respectively, and the others are in between (Table S1-1). This shows a roughly linear relationship with the double layer capacity under the electrochemical condition (Figure S1-3, Table S1-1). The M-N-C samples showed a moderate hydrophilic character (Figure S1-4). The XRD patterns (Figure S1-5) reflect the predominant amorphous carbon support, particularly for Mn, Co, Ni or Cu-N-C; while the presence of Fe, to some extent, led to graphitic domains. Some residual Fe, Co, Ni in a metallic state was detectable after the H_2 reduction at 900 ^oC. The STEM elemental mappings (Figure S1-6) are fully consistent with the XRD findings showing presumably carbon-encapsulated metal particles as well as coordinated metal ion sites for the three catalysts.

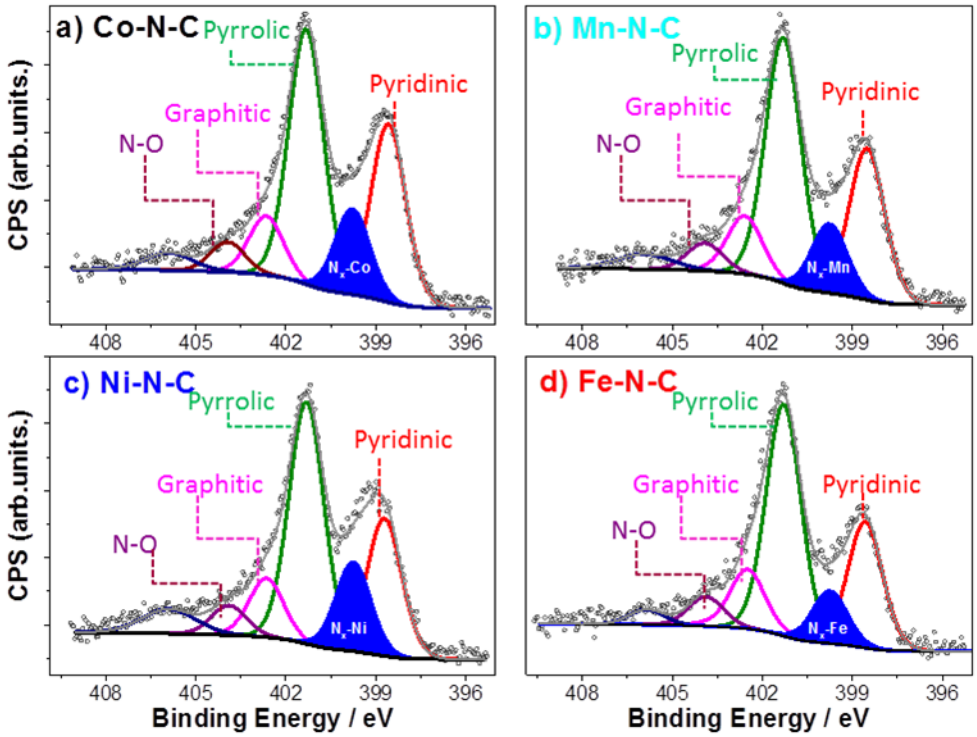

Figure 4- 2 High-resolution XPS characterization. N-1s XPS core level region of (a) Co, (b) Mn, (c) Ni and (d) Fe doped M-N-C catalyst. The 2p3/2 spectra of the corresponding metal peaks (Co-2p, Mn-2p, Ni-2p, Fe-2p) is shown in Supplementary Figure S1-8.

The catalyst surface chemical composition and state were investigated using X-ray photoelectron spectroscopy (XPS). Fitted high-resolution N1s spectra (Figure 4-2 for Co, Mn, Ni, Fe, and Figure S1-7 for Cu, detailed fitted parameters in Table S1-2) evidenced the presence of the porphyrin-like metal-coordinated M-N_x moieties (399.7 eV), as well as pyrrolic (401.3 eV), pyridinic (398.6 eV), graphitic (402.5 eV), and N-O_x (403.9 eV) species (Figure 4-2).[49,50] Additionally, a weak and broad peak can be fitted at higher binding energies, centered at 405.9 eV, which is likely assigned to trace amounts of non-decomposed nitrogen precursors.[70] The N1s spectra of all samples are dominated by pyrrolic nitrogen (see Table S1-2), whereas the M-N_x moiety gives rise to the most intense core level for the Ni-doped sample. A detailed analysis of the metal $2p_{3/2}$ shake-up photoemission lines (marked in Figure S1-8) offers insight in the chemical state of the metallic species. Combined, our materials characterization confirmed the prevalent presence of N-coordinated metal single-site moieties, M-N_x, near the surface in all catalyst samples, except for the Cu sample that exhibited evidence of near-surface metallic Cu particles (Figure S1-7a).

Better understanding of the type of metallic species present in these samples can be obtained by a detailed analysis of the corresponding $2p_{3/2}$ photoemission lines, shown as insets in Figure S1-8. Due to the low metal loading in our samples, we cannot fit the data with the multiple splitting features typical for oxides and hydroxides.[71] Instead, in order to gain insight into whether oxidized metal species or nitrogen-ligated metals prevail in our samples we have compared the main $2p_{3/2}$ photoemission peak positions with data reported for divalent metal species and metalloporphyrins, and a ratio of its area to the area of the shake-up

satellites, which serves as a fingerprint of 3d metals in 2+ state. Muralidharan and Hayes have reported shake-up structures for Co(II), Ni(II) and Cu(II) porphyrins to be significantly weaker than the corresponding satellites of simple oxides of the same elements.[72] Thus, Ni(II) porphyrin exhibits an XP spectrum with $2p_{3/2}$ peak centered at 854.8 eV, which is similar to $Ni(OH)_2$, but unlike the latter it has a shake-up structure of only 11% intensity as compared to the main line. In fact, the Ni-N-C sample in our study has the main Ni $2p_{3/2}$ photoemission peak at 854.9 eV and a shake-up peak just 18% of its area, suggesting a dominant presence of Ni bound to nitrogen in our samples. In contrast, the Co-N-C sample displayed a significantly more intensive shake-up structure, ca. 20% of the main Co 2p3/2 peak area, which is considerably higher than a value reported for Co(II) porphyrin (6.5%), but also clearly lower than CoO and $Co(OH)_2$ (38% and 54% correspondingly). Mn $2p_{3/2}$ of Mn-N-C has its maximum at 641.7 eV, similar to MnO, and lower than compounds with Mn^{3+} and higher oxidation states.[73] At the same time, the shake-up structure is as high as 11% of the main photoemission peak, which is slightly higher than the one reported for MnO (9%). Unfortunately, there is no reliable XPS reference for the manganese porphyrin structure. One can speculate however that Mn-N-C clearly contains divalent Mn species with a ligand structure different from common Mn^{2+} compounds. The Cu 2p XP spectrum (Figure S1-7a) shows a clear presence of divalent copper, as evident from the well-developed shake-up. Cu $2p_{3/2}$ XP spectrum shows two sharp peaks at 932.7 and 934.8 eV and a shake-up satellite structure between 938.4 and 947.3 eV. A binding energy of 934.8 eV is similar to the value reported by Biesinger at al[71] for $Cu(OH)_2$, but also to Cu porphyrin.[72,73] The observed intensity of the shake-up satellite structure is 59% of the main line, which is only slightly higher than the 53% for both, Cu-porphine[72] and $Cu(OH)_2$ reported by Biesinger[71]. The peak at 932.7eV can be assigned either to metallic copper or to Cu_2O, however a detailed analysis is not possible due to weak CuLMM Auger line.[71] It appears however reasonable to assign this peak to the Cu^+ state, since metallic copper in the near-surface region is unlikely to remain after multiple acid treatments. The Fe $2p_{3/2}$ spectrum of the Fe-N-C sample shows a broad peak at 710.8 eV with a shoulder at ca. 708 eV. The position of the former and absence of distinct satellite structure points out the presence of significant amount of Fe_2O_3, while the latter is in an agreement with the values reported earlier for iron phthalocyanine.[74] According to Fe $2p_{3/2}$ XP spectrum deconvolution, the nitrogen-coordinated iron comprises only 1.6% of the total Fe content observed by XPS.

4.2 Electrochemical CO_2RR over various M-N-C catalysts

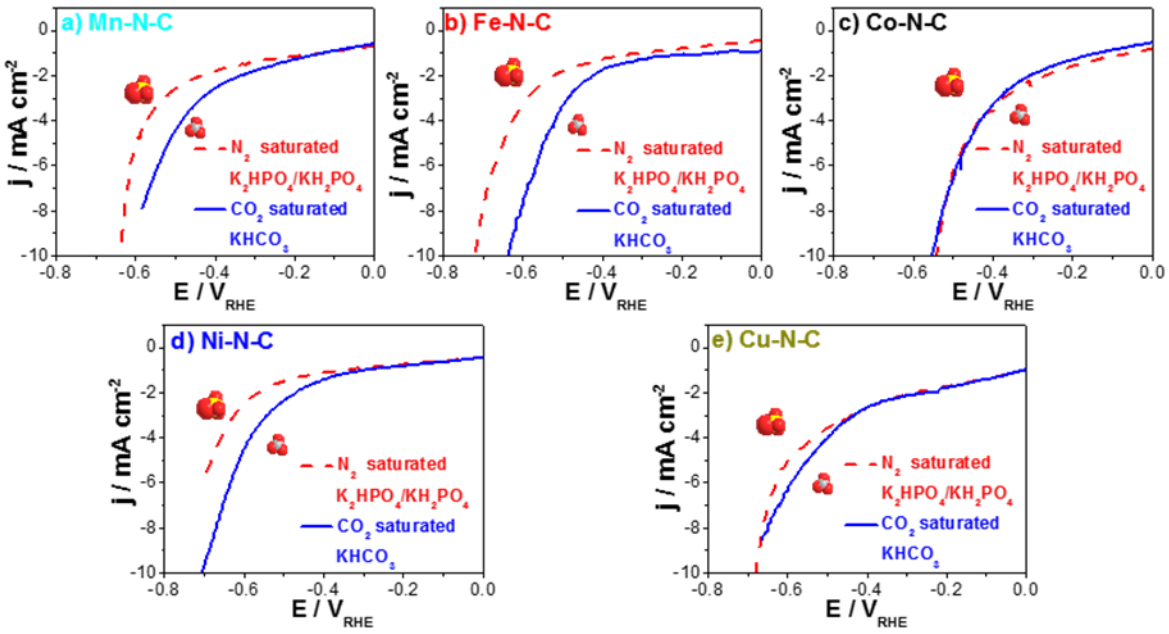

Figure 4- 3 CO_2 reduction reaction activities. Linear sweep voltammetry of a) Mn-N-C, b) Fe-N-C, c) Co-N-C, d) Ni-N-C and e) Cu-N-C in CO_2-saturated 0.1 M $KHCO_3$ (solid lines) and in N_2-saturated 0.1 M KH_2PO_4/K_2HPO_4 (dashed lines) with a catalyst loading of 0.76 mg cm^{-2} at 5 mV s^{-1} in cathodic direction.

As a first test of the total faradic reactivity of our single-site solid catalysts in CO_2-saturated 0.1 M $KHCO_3$, comprising both the HER and CO_2RR, Linear Sweep Voltammetry (LSV) were performed between 0.0 and -0.7 V vs. RHE, blue solid curves in Figure 4-3. Comparison with LSVs performed in absence of CO_2 (red dashed curves) revealed substantial CO_2RR activity of the Mn, Fe, Ni and Cu-doped catalysts. Furthermore, the Mn, Fe, Ni and Cu -doped samples exhibited an earlier onset (smaller overpotential) for the CO_2RR than HER, suggesting that, at least in a small potential window, they are selective towards CO_2RR. By contrast, Co-N-C presented a comparable activity suggesting that the HER may be the dominant faradic process over the investigated potential range.

Longer-term catalytic performance testing was conducted using potential-controlled 1 hour electrolysis. The geometric electrode area-normalized (j_{geo}) and the active interfacial area-normalized (double-layer capacity-normalized) faradaic currents (j_{DL}) after 15 min and 60 min are compared in Figure S1-9. The Co-N-C catalyst generated the most overall faradaic current, while the Cu-N-C displayed the poorest overall reactivity at larger overpotentials, in accordance with Figure 4-3.

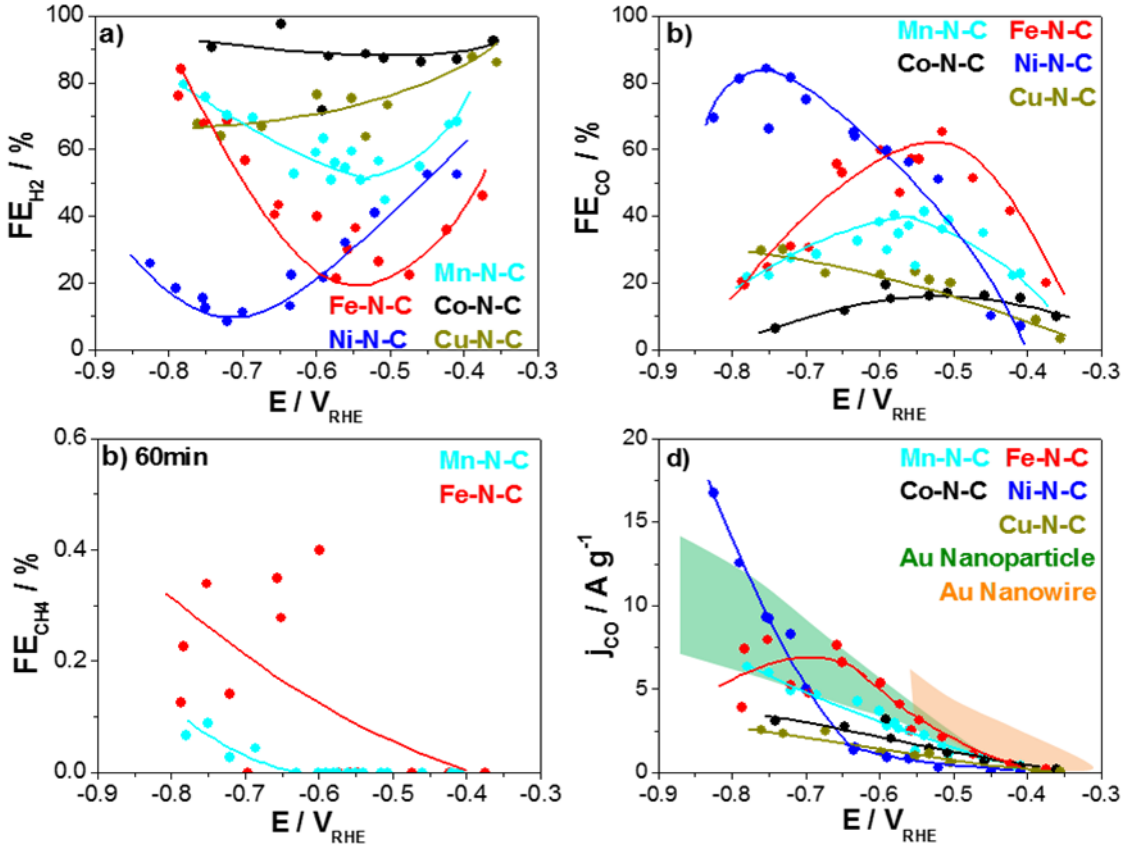

Figure 4- 4 Catalytic performance and product analysis. (a-c) Faradaic Efficiencies (FE) vs. applied, iR-corrected electrode potential of a) H_2, b) CO and c) CH_4. d) Catalyst mass-normalized CO partial currents (mass activity) vs. applied potential for the five M-N-C catalysts compared to state-of-art Au catalysts (performance ranges of Au-nanoparticle and Au-nanowires are shown by filled areas [10,11]. Lines to guide the eye. Conditions: 60 min at constant electrode potential in CO_2-saturated 0.1 M $KHCO_3$ with 0.76 mg cm^{-2} M-N-C catalysts loading. Faradaic efficiencies and CO yields after 15 min are shown in Figure S1-10.

The stationary faradaic efficiencies (FE) of the three principal CO_2RR products after 60 min electrolysis are displayed in Figure 4-4. H_2 and CO accounts for up to 95% of the transferred charge on the single-site catalysts. Remarkably, small amounts of methane were detected, however only on Fe and Mn catalysts, while no liquid product could be detected. Despite the low number of active surface single-sites on the M-N-C catalysts, their mass-based partial CO currents (production rate) towards CO meets and are comparable to that of Au-based catalysts[10,11], especially at technologically interesting higher currents (Figure 4-4d). These results highlight the significance of this family of compounds as non-precious, earth-abundant low-cost and efficient CO_2RR catalyst alternatives for the electrochemical production of CO in CO_2 -consuming electrodes.

To arrive at a fundamental mechanistic understanding of the CO_2 catalysis on the single-site materials, we focus on reactivity trends among the M-N-C catalysts at different applied overpotentials. The CO_2RR performance exhibits a strong dependence on the nature of the transition metal, not only in terms of the molar CO/H_2 ratio, but also in the experimental overpotential at maximum CO efficiency (see Figure 4-4 a

and b). H_2 FE on Co-N-C remains above 80% over the entire electrode potential range, making it a catalyst with poor selectivity towards CO_2RR. On the other hand, Fe-N-C and particularly Ni-N-C catalysts clearly act as highly promising catalyst for selective CO production, however, the maximum CO FE is obtained at a smaller overpotential on Fe-N-C (V_{RHE} = -0.55V, FE_{CO} = 65%) than on Ni catalyst (V_{RHE}=-0.78V, FE_{CO}=85%). Note that the selectivity of these two single site catalysts is drastically different from that of metallic Ni and Fe catalysts, which yield H_2 as virtually the only major product.[4] We have conducted a number of control measurements to confirm that the M-N_x site is indeed the most significant active center for CO_2 reduction into CO. First, the Nitrogen Free M-C as well as the polymer precursor before pyrolysis (Cu-Bpy) contributes negligibly to the CO activity during the CO_2RR process. Secondly, we could not exclude some catalytic activity of the Nitrogen functionalities. However, based on their finite CO_2RR catalytic reactivity and the rough similarity of the distribution in the M-N-C catalysts, their effect could be seen as a known weak background signal for all cases (Supplementary Table S1-2, Figure S1-11 and Figure S1-12). This finding strongly suggests that the CO_2RR (into CO) reactivity trends purely originate from the differences in intrinsic catalytic activity of the various M-N_x moieties.

4.3 Correlating the theoretical prediction and experiments

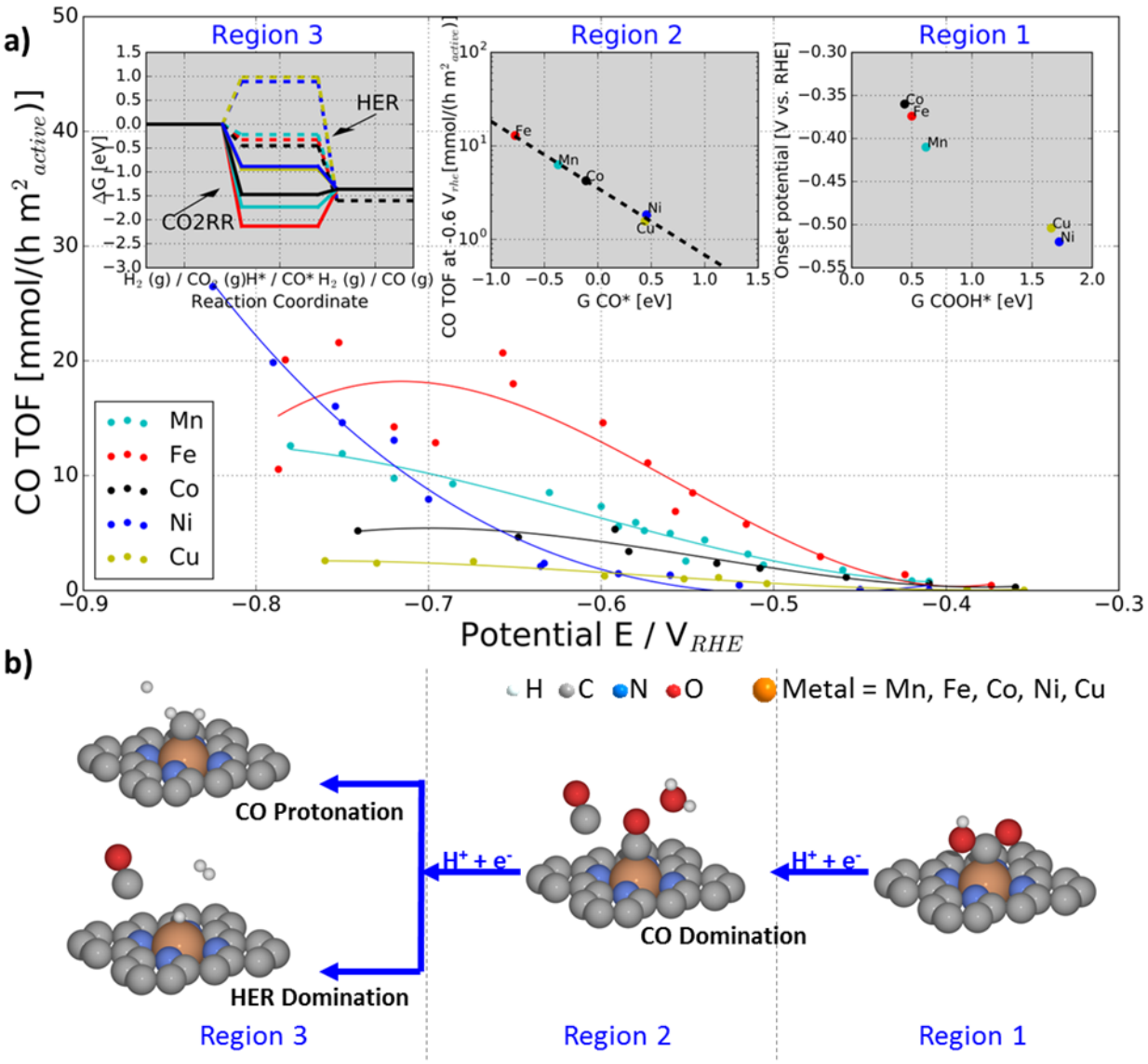

Figure 4- 5 Experimental correlation to simulations. Experimental CO production turnover frequency (TOF) of the M-N-C catalysts versus applied iR-corrected electrode potential. The a) catalytic reactivity trends and b) reaction pathway split into three potential regions with distinctly different rate-determining mechanistic features. Free energy diagrams for HER and CO_2RR at 0.0 and -0.6 V_{RHE} are given in Figure S1-13. Insets: Region 1: Low overpotentials, the experimental onset potentials of CO production (better seen on the log (CO TOF) – E plot in Figure S1-14) correlate with the binding energy of the reaction intermediate COOH* taken from Figure S1-13. Region 2: Intermediate over-potentials, CO production TOF at -0.6 V_{RHE} correlates with the free energy of adsorbed CO, CO* taken from Figure S1-13; Region 3: High overpotentials, free energy diagrams for the HER (dashed paths) and CO_2RR (solid paths) at -0.8 V_{RHE} for each M-N-C catalyst. HER barriers are high for Ni and Cu, while CO_2RR is downhill making these materials favorable CO producing catalysts.

To bring theoretical mechanistic insight, DFT simulations pertaining to the CO_2 reduction process on N-coordinated metal-doped M-N-C catalysts were carried out. For this purpose, we took the single-site motif M-N_4 as active site to calculate the binding energy of the different reaction intermediates (see Figure S1-13). We note that there exist other M-N_x functionalities[75-77], however, previously we computationally found the metal be the dominating factor compared to other M-N_x functionalities.[78] Thus, the M-N_4 site appears to be a reasonable single active site model for our analysis here. For the model we calculate the binding energies without electrolyte, which is reasonable for the trends and conclusions drawn here. While activity can often be associated with a single descriptor, selectivity can obviously not, as it is related to competition between different possible reaction paths. The different reaction paths show different dependence on metal center and potential.

Figure 4-5 compares the trends in the experimental CO-specific turnover frequencies (TOF) of the five M-N-C catalysts. The TOF values were derived from the absolute CO production rates normalized by the respective BET surface area-weighted surface M-N_x concentration (see Equation 4-1).

$$\mathrm{TOF} = \frac{\dot{V} * C}{R * M * A_{BET} * x_{Metal-N}} \qquad \text{eq. 4-1}$$

TOF: BET Area and XPS Surface Metal-Nitrogen mole fraction Normalized CO generation rate

$\dot{V}$: CO_2 gas flow rate / L s^{-1}

C: Concentration of the product detected by GC / Vol%

R: Ideal Gas Volume / 22.4 L mol^{-1}

M: Catalyst loading / g m^{-2}

A_{BET}: N_2 physiosorption BET surface area/ m^2 g^{-1}

$x_{Metal-N}$: XPS surface Mole fraction of Metal-Nitrogen

By correlating the experimental TOF trends and predicted DFT theoretical energy diagrams, we were able to identify three regions of distinct reaction dynamics that control the electrocatalysis. Firstly, region 1, a dynamic regime at low overpotentials near the onset of the CO production, then, region 2, a dynamic regime at intermediate overpotentials and finally, Region 3, at larger overpotentials where the CO_2 reduction current densities approach technologically relevant levels. The reason for this division is that the order in catalytic activity change in the different regions indicating that the rate in the different regions is determined by a distinctly different surface chemistry.

The low overpotential regime around -0.45 V_{RHE} (Region 1). Defining the CO production onset potential to be the applied electrode potential at which the CO TOF exceeds 0.2 mmol h^{-1} m^{-2}_{active}, the Fe, Mn and Co-N-C catalysts start producing CO at around -0.4 V vs. RHE, while the Cu and Ni samples require considerable higher overpotentials, see Region 1 insert in Figure 4-5. The onset potential is determined by the mechanistic elementary step that is the last to become exergonic as the overpotential is increased

(limiting potential). Simulations suggest that this potential-determining step is the first proton-coupled electron transfer reduction of CO_2 to adsorbed COOH* according to:

$$CO_2 + H^+ + e^- \leftrightarrows COOH^* \qquad \text{eq. 4-2}$$

In agreement with electrochemical measurements, in the simulations the catalyst falls into two groups: Co, Fe and Mn requiring only a small overpotential, whereas Cu and Ni need a larger thermodynamic driving force for that step.

The intermediate overpotential regime around -0.6 V_{RHE} (Region 2). Here, the Fe- and Co-N-C catalysts approach their maximum CO_2RR reactivity, while the Ni-N-C catalyst has barely passed above its CO production onset. With the electrode potential being now past the limiting electrode potential, the overall CO_2 reduction reaction invariably becomes limited by a non-faradaic chemical reaction step. The larger the thermodynamic driving force of this step, the faster the overall reaction rate. Correlating experiments to DFT calculations reveals that the logarithm of the experimental CO TOF is now linearly related to the CO* binding energy descriptor, see Region 2 insert in Figure 4-5. This suggests that the rate-controlling intermediate has shifted from COOH* to CO*. As a result of this, the overall reaction rate appears limited by the process

$$COOH^* + H^+ + e^- \leftrightarrows CO(g) + H_2O \qquad \text{eq. 4-3}$$

While DFT predictions do not allow us to unambiguously pinpoint the exact rate-limiting point along the reaction coordinate of step (2), we hypothesize that it is the chemical dissociative formation of H_2O according to

$$COOHH^* \leftrightarrows CO^* + H_2O \qquad \text{eq. 4-4}$$

The stronger CO* binds, the more driving force is available for this step. An evidence for the hypothesis can be considered by comparing the Fe- and Mn-N-C, which have almost similar COOH* and H* binding. However, these descriptors cannot explain the experimental different CO TOF from the two, while the logarithm to the CO* descriptor can. (Figure S1-14)

The large overpotential regime < -0.7 V_{RHE} (Region 3). Here, the experimental CO formation TOF in Figure 4-5 as well as the faradaic CO efficiencies of the Fe-N-C and Co-N-C catalysts have passed their maximum and trend downward (see Figure 4-4b). That of Mn-N-C is levelling off, while the Ni-N-C catalyst continues to increase its CO production rate at a very high faradaic CO efficiency, significantly outperforming all other single-site catalysts as well as Au catalysts.

Our mechanistic DFT analysis shown in inset, Region 3, of Figure 4-5 is able to consistently explain all these experimental findings. The free energy diagrams of the HER (dashed) and CO_2RR (solid) evidences that the Fe-, Co- and Mn-based catalysts start to strongly catalyze the hydrogen evolution (H^++e- → H* →

H_2(g)) illustrated by the all downhill reaction energy pathway. Among them, Co-N-C is the most efficient HER catalyst and, thus, displays the highest faradaic efficiency for hydrogen evolution, see Figure 4-4a. In contrast, the Ni- and Cu-based catalysts exhibit very weak binding of H* which makes the HER thermodynamically unfavorable at -0.8 V_{RHE}, giving rise to low faradaic hydrogen efficiencies.

The DFT predictions of the CO_2RR pathway ($CO_2 \rightarrow CO^* \rightarrow CO_{(g)}$) at -0.8 V_{RHE} complete the mechanistic picture. While the Ni-N_x and Cu-N_x moieties stand out as the single sites with the weakest binding to COOH* and therefore with the largest overpotential to start CO_2 reduction (see Region 1), their weak binding of CO* prevents the potential-independent chemical CO-desorption process ($CO^* \rightarrow CO(g)$) to become rate-limiting. This is in contrast with the Mn, Fe, Co-N_x sites whose CO TOF is controlled by the $CO^* \rightarrow CO(g)$ step due to their strong CO* binding (solid pathways in Region 3) leading to a positive ΔG of CO desorption. Indeed, experimentally, the CO TOF values of the Mn, Co and Fe-N-C level off or slow down, while the hydrogen evolution accelerates.

We note that the relatively strong binding of CO* on Fe-N_x and Mn-N_x single sites predicted for Region 3 is fully supported by the experimentally confirmed exclusive ability of these two catalysts to produce the hydrocarbon CH_4, see Figure 4-4c. In simple terms, one could say that to produce subsequent reaction products from CO during the CO_2RR, the CO molecule must be bound strong and long enough to undergo subsequent dissociation and hydrogenation steps to arrive at CH_4. For the Ni and Cu catalysts, the CO* detaching is energetically all downhill reaction which prevents further transformations. This makes Ni-N_x and Cu-N_x single-site catalysts ideal electrochemical CO producers. We note that the experimentally observed reactivity trend of the Cu-N_x catalysts in region 3 does not closely follow that of Ni. This is due to a DFT-predicted thermodynamic instability (not shown) of the Cu-N_x moiety under the strongly reducing conditions of $< -0.7 V_{RHE}$ in region 3. As a result of this, the N-coordinated Cu ions spontaneously reduce to metallic Cu nanoparticles – as confirmed by our XPS results – which show lower CO efficiency and lower TOF values at electrode potentials of region 3.[12]

4.4 Discussion

In this work, we found a family of solid, single site, N-coordinated transition metal-functionalized nanoporous carbons that show very high electrocatalytic reactivity and selectivity with respect to the direct CO_2 reduction to CO (CO_2RR). A technical challenge in these M-N-C catalysts is to achieve a high density of active M-N_x sites, while minimizing effects of other nitrogen moieties and inorganic metal impurities, which, for this class of materials cannot be completely excluded. However, based on our experimental observation, we could confirm that the M-N_x site play the dominant role during the CO_2RR process into CO. For instance, the Co-N_x sites were efficient hydrogen producers whereas the Fe- and Ni-N_x single site catalysts showed a unique reactivity and faradaic efficiency for reducing CO_2 into CO, meeting and exceeding the mass-based activity of state-of-art Au catalysts at a fraction of their cost.

To understand the trends in reactivity and selectivity of the single site catalysts we have correlated our experimental results with DFT simulations of the energetics of the competing reaction pathways involved. Our results demonstrate that the binding energies can be used as descriptors to predict the CO_2RR activity and selectivity of this class of catalysts. This is why we find a good agreement between the DFT predictions and the catalytic experiments offering a detailed mechanistic understanding of the role of the metal centers in the considered catalytic processes.

Consistent with experiments, Co-N_x sites displayed all-downhill energetics for hydrogen, but severe energetic barriers to CO formation. By contrast, the low H* and CO* binding energy of the Ni-N_x single site required larger overpotentials to jump start the reactions. At larger overpotentials, however, Ni-N_x catalysts displayed all-downhill energetics toward CO, while hydrogen evolution is hindered.

The high CO efficiency at medium and large overpotentials of the Fe-N-C and Ni-N-C materials combined with their earth-abundant constituents, compared to standard Au catalysts, makes them attractive catalysts for deployment in future industrial CO_2-consuming CO cathodes for use as counter electrode process in the chlorine production industry. The choice of catalyst thereby becomes a tradeoff between voltage efficiency (Fe produces most CO at lower potentials) and turnover frequency/current density (Ni makes most CO at higher overpotentials). In particular for Ni-N-C catalysts, high CO efficiencies at current densities approaching industrial levels make them suitable candidates for CO_2-consuming gas-diffusion cathode (CCC) designs to be deployed in next-generation chloralkaline electrolyzers. By eliminating the need for fossil fuel-based steam reforming toward purified CO feed streams in the Chlorine-mediated polymer industry, CO_2 reuse in chlorine–CO co-electrolyzers would significantly contribute to a lowering of industrial CO_2 emissions worldwide.

Chapter 5. CO evolution at industrial current densities on Ni-N-C derived gas diffusion electrode

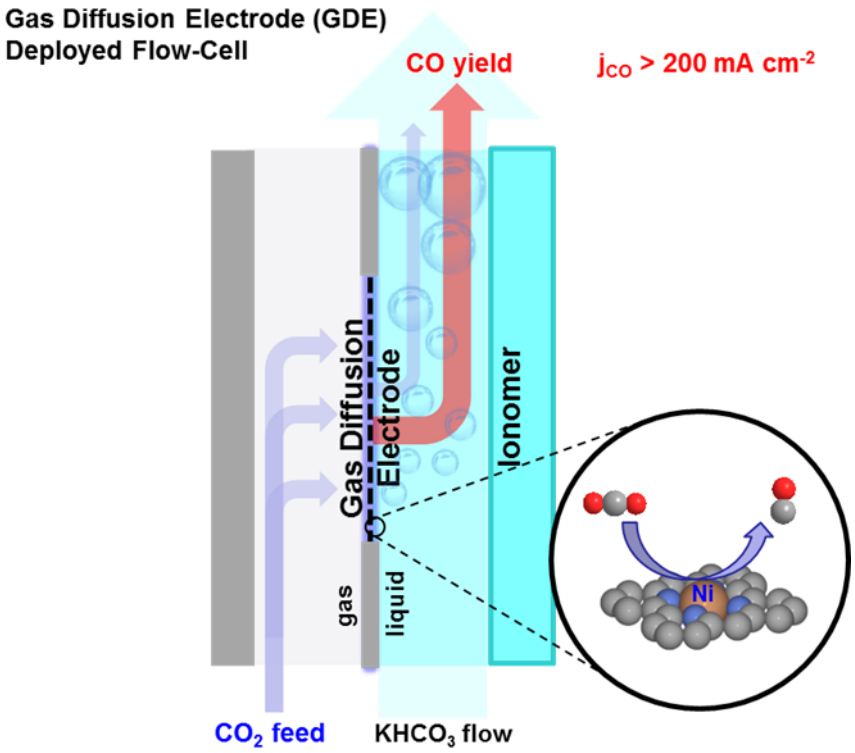

Most parts of this chapter are reproduced from the journal article:

Efficient CO 2 to CO electrolysis on solid Ni–N–C catalysts at industrial current densities

Link: https://doi.org/10.1039/C8EE02662A

with permission from Energy Environ. Sci., 2019, as Reference [58] in this dissertation. Copyright 2019 Royal Society of Chemistry.

Author list: Tim Möller, Wen Ju (co-first), Alexander Bagger, Xingli Wang, Fang Luo, Trung Ngo Thanh, Ana Sofia Varela, Jan Rossmeisl and Peter Strasser

Contributions: T.M, and W.J. conceived and designed the experiments. A.B. performed the DFT calculation. W.J. and F.L. carried out the synthesis and regular characterization. X.W. carried out the HRTEM measurements and data analysis. Electrochemical CO_2RR tests were done by T.M. (GDE-MFC) and W.J. (H-cell). All authors discussed the results, drew conclusions and commented on the manuscript.

The electrochemical CO_2 reduction reaction (CO_2RR) to pure CO streams in electrolyzer devices is posed to be the most likely process for near-term commercialization and deployment in the polymers industry. Delivered by the work presented in Chapter 4, the Ni-N_x and Fe-N_x hold the promise to convert CO_2 into CO at high- and low- overpotentials, respectively. We thus employ the PANI-based M-N-C candidates and, initiate the electrochemical testing in regular small-scale CO_2-saturated liquid electrolyte H-cell screening, and obtain parallel performance of that given by the Cu-MOF derived M-N-C catalysts. However, electrolysis conducted in normal H-type electrolyzer only provides limited current densities below 50 mA cm^{-2}, which is far not sufficient to commercializing level.

To overcome this bottleneck, we deploy a type of Gas Diffusion Electrode (GDE) combined Micro-Flow-Cell (MFC) to drive the CO_2 electrolysis on M-N-C catalysts, the catalytic performance of Ni-based one rivals or exceeds the state-of-art electrocatalysts under industry equivalent conditions. tests and moved to larger-scale CO_2 electrolyzer cells, where the catalysts were deployed as GDEs to create a reactive three-phase interface. We compared the faradaic CO yields and CO partial current densities of Ni-N-C catalysts to a Ag-based benchmark, and to its Fe-containing Fe-N-C analogue under ambient pressures, temperatures and neutral pH bicarbonate flows. Prolonged electrolyzer tests were conducted at industrial current densities of up to 700 mA cm^{-2}. Ni-N-C electrodes are demonstrated to provide CO partial current densities above 200 mA cm^{-2} and stable faradic CO efficiencies around 85 % for up to 20 hours (at 200 mA cm^{-2}), unlike their Ag benchmarks. Density Functional Theory-based calculations of catalytic reaction pathways help offer a molecular mechanistic basis of the observed selectivity trends on Ag and M-N-C catalysts. Computations lend much support to our experimental hypothesis as to the critical role of a N-coordinated metal ion, Ni-N_x, motifs as the catalytic active site for CO formation. Apart from being cost effective, the Ni-N-C powder catalysts allows flexible operation under acidic, neutral, and alkaline conditions. This study demonstrates the potential of Ni-N-C and possibly other members of the M-N-C materials family to replace precious group metal catalysts in CO_2-to-CO electrolyzers. [58]

5.1 Catalysts synthesis and characterization

In this approach, a series of poly aniline (PANI) derived M-N-C catalysts are synthesized as the candidates for electrochemical CO_2 reduction. The synthesis is done by mixing and pyrolyzing PANI as the Nitogen-precursor and a high surface area Ketjen 600 as the carbon source (hard template), whereas Fe- and Ni-chloride are used as metal precursors. High-temperature pyrolysis of the precursor mixtures is performed in pure N_2 atmosphere at 900°C for 1 hour, after which residual metal species were leached with H_2SO_4. This catalyst synthesis is based on a proven recepie for solid PGM-free metal/nitrogen doped carbon powder catalysts previously tested for the oxygen reduction reaction.[37,39,41] Synthesis procedure of the regarding M-N-C catalysts is listed below (schematic is shown in Figure 5-1).

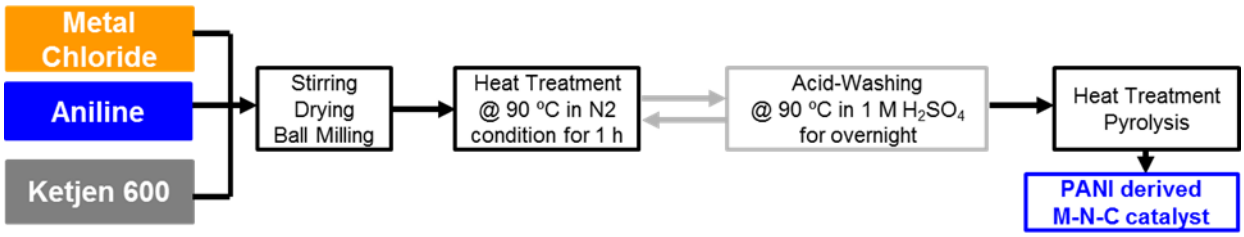

Figure 5- 1 Synthesis procedure of our studied polyaniline (PANI) based M-N-C catalysts.

Preparation of carbon support. Treated Ketjen EC 600JD (AzkoNobel) was used as the hard template of the PANI based catalyst. It was firstly stirred in 0.5 M HCl for 24 hours and then rinsed with DI water to reach neutral pH. Afterwards, the dried carbon was refluxed in concentrated nitric acid for 8 hours at 90 °C followed by rinsing with DI water till the pH value turned to 7. After drying at 90 °C in the oven, the carbon will be referred as carbon support. Before the further utilization for catalyst synthesis, the carbon support was sonicated in 50 mL DI-water till homogenously dispersed.

Synthesis of Fe-N-C. Preparation of the Fe-N-C follows a procedure published in Ref[97]. 3 ml of aniline, 5 g iron chloride ($FeCl_3$) and 5 g ammonium persulfate (APS, $(NH_4)_2S_2O_8$) was added to 0.5 L of 1 M HCl and stirred for one hour. Then, the suspension was stirred for 48 hours along with 0.4 g of dispersed carbon support. Afterwards, the suspension was dried at 95 °C for 24 hours. After drying, the solid mixture was ball-milled in a Zr_2O_3 container with Zr_2O_3 balls (ball diameter 1 cm). Heat treatment (HT) was performed in a furnace with a ramp of 30°C min^{-1} to 900 °C and kept at this temperature for 1 hour within N_2 atmosphere (flow rate: 30 ccm). After cooling down, the material was washed in 2 M sulfate acid (AW) overnight and rinsed to neutral pH by use of vacuum filtration. Usually, to obtain high purity active M-N_x coordinative moieties, multiple times acid-washing is a necessary process to remove the excessive inorganic species and the XRD profiles in terms of acid washing amount is recorded in Figure S2-1. An HT-AW-HT-AW-HT-procedure was performed for to obtain the final Fe-N-C catalyst.

Synthesis of Ni-N-C. The synthesis of Ni-N-C is analogous to the Fe-N-C preparation but $NiCl_2$ is used as metal precursor and one additional AW-HT cycle is performed compared to Fe-N-C. It is necessary to note

that the metallic nickel is distinct and has a special interaction with carbon species. This is why nickel is commonly used as a catalyst for nanotube growth.[79,80] Taking this into consideration, Ni particles formed during the synthesis are likely to be further covered and encapsulated by the carbon matrix. This results in the formation of acid-unsolvable Ni particles, protected by a carbon layers and strong signals in the XRD from a crystalline phase (Figure S2-2). In Figure S2-3, we measured that the thickness of the dense carbon layer is over 10 nm, denying the corrosion by the acid-treatments during the synthesis steps, while simultaneously blocking any catalytic reactivity of such particles as well as the XPS detection (on the crystalline).

Synthesis of metal free N-C. The synthesis of the metal free PANI (N-C) starts with an identical route to the Fe-N-C preparation but does not involves any metal precursor. The N-C catalyst is obtained after the first HT and does not involve any AW steps.

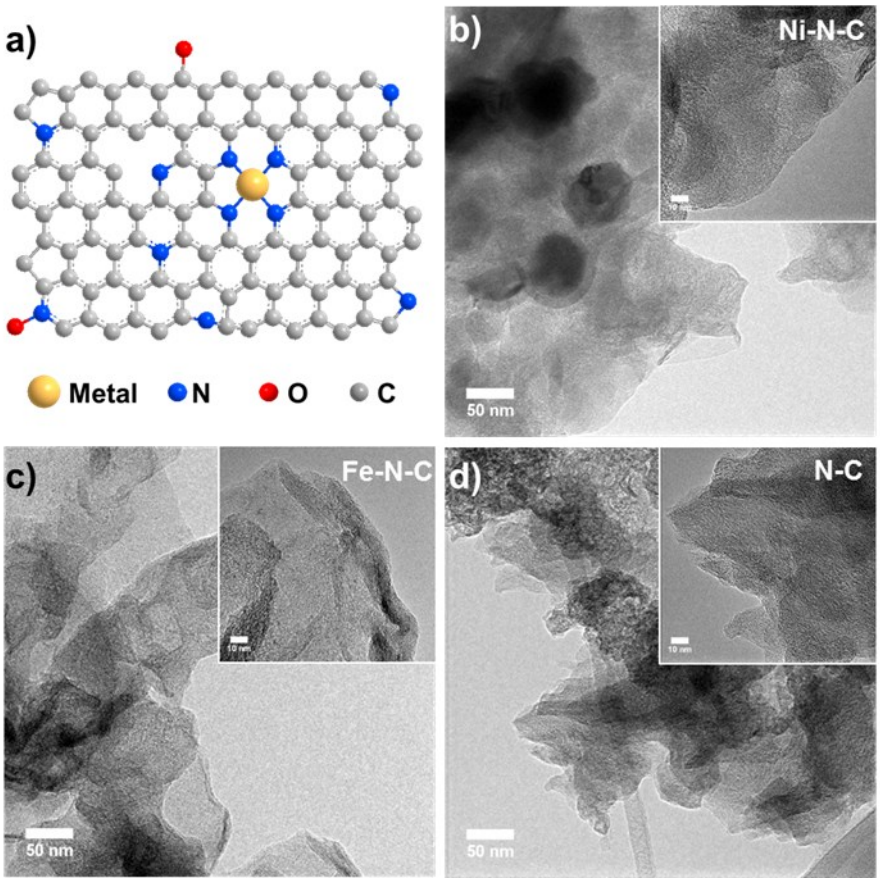

Figure 5- 2 Illustration of M-N-C catalysts. Representative TEM images of a) N-C, b) Fe-N-C and c) Ni-N-C catalysts. Inserts: HR-TEM images of as-prepared catalysts. Figure S2-3 represents the thickness (over 10 nm) of carbon layers encapsulating the inorganic Nickel species.

Figure 5-2a schematizes the typical various chemical states of carbon-embedded nitrogen atoms as reported in decade-long past work, including pyridinc, pyrrolic, quaternary, graphitic, oxidized nitrogen, and the Metal-N_4 moiety. A metal-free nitrogen-doped carbon powder catalyst (referred to as "N-C") was synthesized as control. Physico-chemical characterization of the degree of crystallinty and crystalline

phases was carried using X-Ray Diffraction (XRD). Experimental patterns in Figure S2-2 reflect a largely amorphous character of the N-C and Fe-N-C catalysts, whereas residual crystalline inorganic Ni species were detected for the Ni-N-C. The Tranmission Electron Microscopy (TEM) images (Figure 5-2 b-d) and the bulk compositional analysis by ICP-OS (see Table S2-1) agree with our XRD findings, revealing a predominantly amorphous character of the N-C and Fe-N-C catalysts, while carbon-encapsulated particles were visible in the Ni-N-C powder (Figure S2-3). Specific surface areas of the three catalysts were assessed by N_2 physiosorption isotherms (see Figure S2-4). Table S2-1 compares the experiment-derived, calculated Brunauer-Emmett-Teller (BET) surface areas: Fe-N-C displayed more than $600\,m^2\,g^{-1}$, almost 3 times larger than that of the Ni-N-C and metal free N-C catalysts. A significant rapid N_2 uptake at relative pressures above 0.9 for the Fe-N-C sample (see Figure S2-4a) suggested rich mesoporosity confirmed by the calculated pore distribution (Figure S2-4b). All these ex-situ surface area tests stand in line with the in-situ electrochemical double layer capacity measurements used to independently confirm the trend in the real surface areas among the three carbonous catalysts (see Figure S2-5). Chemical analysis and nitrogen speciation of the catalyst's surface was conducted using X-Ray photoeelectronmission spectroscopy (XPS) using survey scannings (Figure S2-6a) and high resolution analysis (Figure S2-6 b-d). The surface atomic mole fractions of metal M, nitrogen, oxygen, sulphur, and carbon are given in Table S2-1. It is noteworthy that even though more than 10wt.% Ni was detected in the bulk, XPS data evidence that the Ni species show a molar fraction of only 0.38% in the catalyst surface, confirming the succees of the acid leaching. This also suggests that the residual encapsulated Ni particles that have resisted the repeated acid leaching procedure, must be densely encapsulated by $\geq$ 10 nm thick carbon overlayers, indeed as shown by the experimental micrograph in Figure S2-3. These Ni particles are therefore unlikely, probably completely unable to participate in the catalytic CO_2-to-CO reaction process, apart from the fact that Ni particles due to their electronic surface structure are unable to reduce CO_2 to CO.[4] Looking at the high resolution photoemission spectra, the N1s core level region (Figure S2-6b for Ni-N-C) evidenced the presence of the porphyrin-like N-coordinated Ni-N_x moieties at 399.7 eV.[50,61,81]

5.2 Liquid-electrolyte H-Cell screening tests

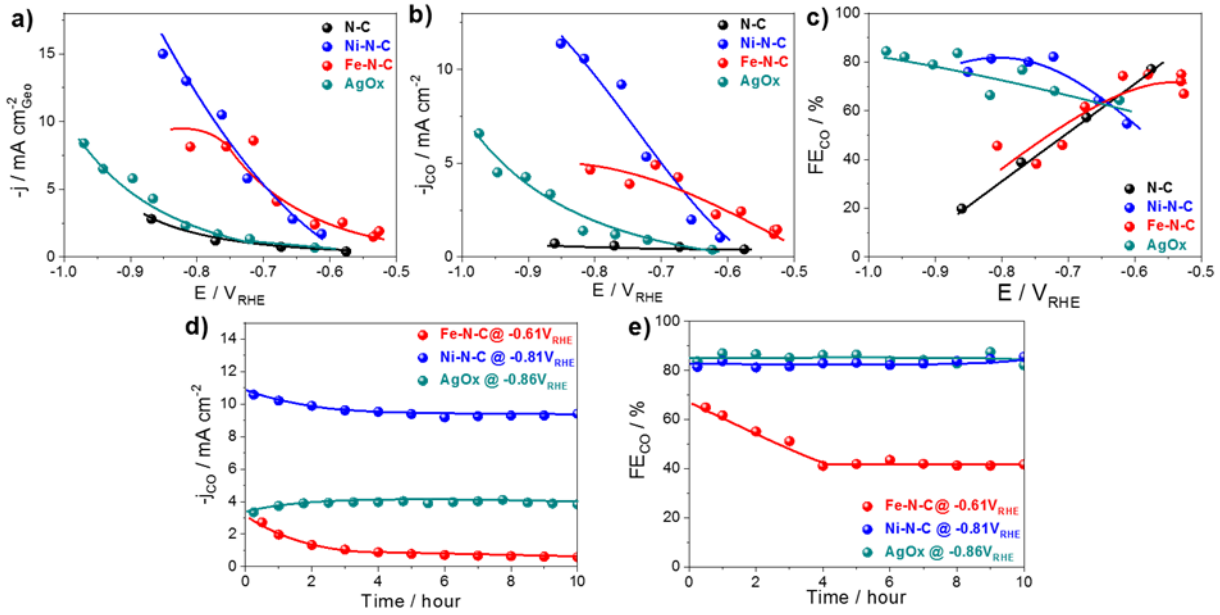

Figure 5- 3 Catalytic performance and product analysis on N-C (black), Fe-N-C (red), Ni-N-C (blue) and AgO_x (Cyan) catalysts. a) Absolute geometric current densities; b) geometric CO production current densities; c) CO faradaic efficiency as a function of applied iR-corrected electrode potential at 15 min of each electrolysis (CO partial current densities and faradaic efficiency at 60 min and faradaic CH_4 yield are shown in Figure S2-7, S2-8). d) Geometric CO production current densities and e) CO faradaic efficiency during the long-term stability testing as a function of stationary electrolysis time. Lines to guide the eye. Conditions: CO_2-saturated 0.1 M $KHCO_3$ (pH 6.8) with 0.75 mg cm^{-2} catalysts loading.

The catalytic performance of the three Metal Nitrogen co-doped carbon electrocatalysts with respect to the electrochemical CO_2 reduction was first evaluated in a three-electrode, two-compartment liquid-electrolyte H-Cell equipped with an ion exchange membrane between anode and cathode chamber. The catalyst was immobilized on a mirror-flat glassy carbon plate with a geometric loading of 0.75 mg cm^{-2}. Additionally, a commercial AgO_x powder (Sigma Aldrich, 223638) catalyst was measured under identical electrochemical conditions as a state-of-art metallic benchmark. We note that we continue to refer to this benchmark catalyst as "AgO_x" even though we are aware that the surface of this catalyst reduces to metallic Ag under reaction conditions. The total CO_2RR current densities as a function of iR-corrected working electrode potentials after 15 minutes of stationary constant-potential electrolysis are reported in Figure 5-3a. These curves compare and contrast the overall catalytic activity of the four catalysts. Clearly, Fe-N-C and Ni-N-C electrocatalysts exhibited much larger overall current densities over the entire potential range. Online Gas Chromatography was used to quantify gaseous products and to assess the faradaic product efficiencies. Without exception, CO was the major detectable CO_2RR product, while all residual faradaic charge contributed to the HER process. Due to stronger chemisorption of CO on the Fe-N_x moieties[51] compared to Ni-N-C, only the Fe-N-C samples catalyzed the consecutive protonation of CO to methane, as evidenced in Figure S2-8. This makes Fe-N-C one extremely rare example of a non-Cu based CO_2RR catalyst with

the capability to reduce CO_2 into "beyond CO" products such as hydrocarbons. No measurable liquid products were found in the electrolyte using High Performance Liquid Chromatograph (HPLC) and liquid GC.

Figure 5-3 b and c plot the partial CO current density and the CO efficiency as a function of iR-free potential. The Fe-N-C carbon catalyst showed good CO_2RR reactivity at lower potentials up to -0.6 V_{RHE} and approached a efficiency maximum[43,51] By contrast, the metal-free N-C catalyst showed only negligible CO_2RR reactivity, again, indicating that the M-N_x moieties played a dominating mechanistic role in the catalytic reactions. Despite comparable CO efficiencies of the Ni-N-C and the AgO_x benchmark catalyst at electrode potentials up to -1.0 V_{RHE}, the CO production on Ni-N-C reached 12 mA cm^{-2} at -0.85 V_{RHE}, which was more than twice that of the AgO_x catalyst (7 mA cm^{-2} at -0.97 V_{RHE}).

To investigate the durability of the catalysts in the H cell configuration, 10-hour electrolysis tests were carried out using the Fe-N-C, Ni-N-C and AgO_x catalysts, each at the electrode potentials where their respective maximum CO efficiency was observed. Partial CO currents and CO efficiency over time data are plotted in Figures 5-3 d and e. Both CO partial currents and CO efficiency of the Ni-N-C catalyst showed only a minor drop, maintaining more than 90% of its initial performance values. This behavior was comparable to the AgO_x catalyst, which, however, displayed a much lower absolute CO yield (see Figure 5-3d). In contrast, the Fe-N-C catalyst started to produce more and more hydrogen until its FE value stabilized after 4 hours. Its absolute CO yield was lower than that of the AgO_x catalyst. We conclude from the screening tests in our H-Cell that the Ni-N-C catalyst met or exceeded the AgO_x benchmark in terms of CO yield, efficiency and stability.

5.3 DFT prediction of CO_2RR into CO over various Ni-N_x-C motifs

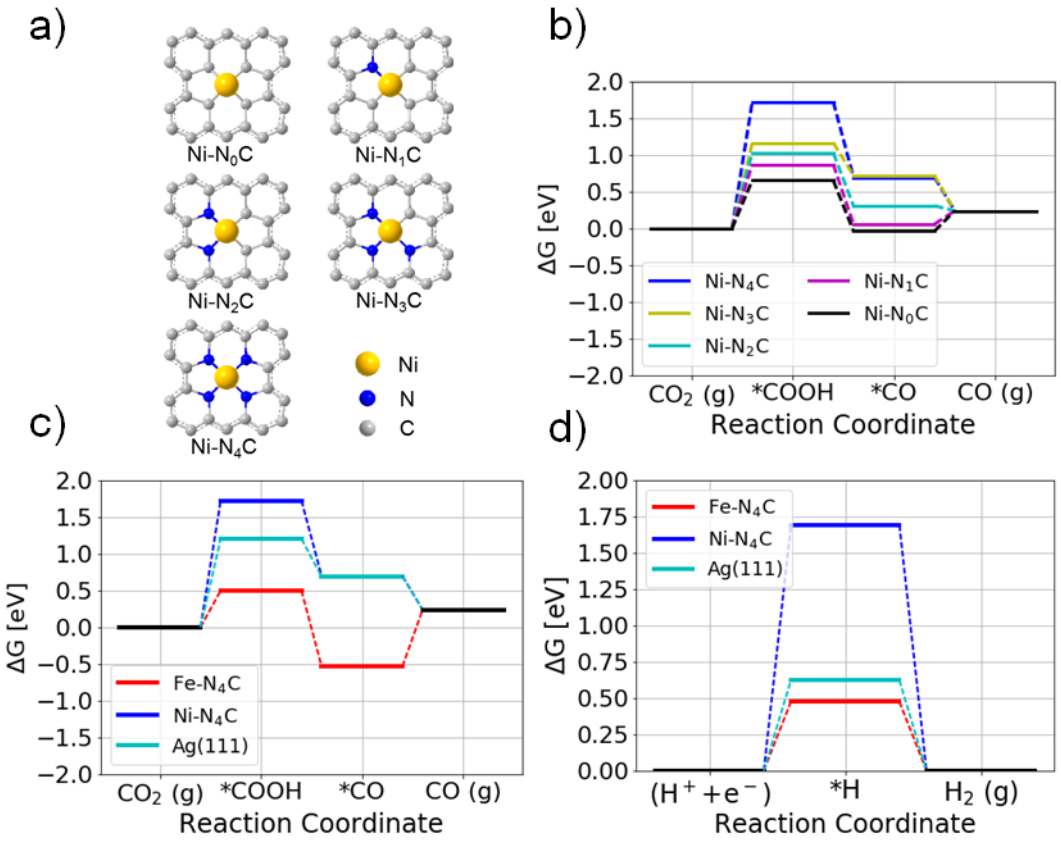

Figure 5- 4 Free energy diagram of CO_2 reduction to CO on Ni-N-C and Fe-N-C catalysts. a) Chemical structure of the M-N_x moieties considered, b) influence of the Ni-coordination on the binding strength for the *COOH and *CO intermediates, c) Free energy diagram of CO_2 reduction to CO and d) hydrogen evolution reaction, d) on Fe-N_4-C (red), Ni-N_4-C (blue) and Ag (111) catalyst (cyan).

To understand the experimental activity-selectivity trends, Density Functional Theory (DFT) simulations were carried out for the catalytic reaction process on well-defined Fe-N_4-C and Ni-N_4-C moieties, and were compared to results obtained with a single crystalline Ag (111) surface. The various metal-nitrogen binding schemes of the moieties are illustrated in Figure 5-4a. Their corresponding free energies are plotted in Figure 5-4b. Finally, a comparison of the free energy diagrams for the CO_2RR and the competing HER pathways on the single-site Metal-N_4 motifs and the Ag (111) metal facet are displayed in Figure 5-4 c and d.

Three considerations can help to understand the performance of a catalyst for the CO_2RR to CO in aqueous conditions. First, the initial selectivity can be evaluated by comparing the intermediate binding energy for *COOH (CO_2RR) and *H (HER). Here, Ni-N_4-C and Fe-N_4-C are quite comparable, while Ag(111) shows a relatively stronger *H binding, agreeing with previous theoretical observations.[15] Second, the desorption of *CO from the active site has to be fast in order to achieve high rates for CO_2RR, therefore *CO binding has to be weak. Both Ag (111) and Ni-N_4-C do not bind *CO (Figure 5-4c), while *CO binds strongly on

Fe-N_4-C, indicating problematic kinetics for the Fe catalyst, but potentially enabling further reduction[15]. Finally, in order to reduce the required overpotential, binding of *COOH needs to be strong, which is the strongest on the Fe-N-C, intermediate for the Ag(111) and weakest on the Ni-N-C. While we do acknowledge the influence that the detailed coordination (Figure 5-4a) or hydrogenated environment (Figure S2-9) could have on the binding properties of the M-N-C, we believe the M-N_4 motif and the (111) metal facet models are appropriate for discussing our experimental observations. In our H-Cell experiments the Fe-N-C material showed the lowest onset-potential for CO formation, agreeing with the calculated strong *COOH binding, and a decrease of FE_{CO} with ongoing time, which can be indicative of a *CO correlated poising caused by strong *CO binding. In contrast, the remarkably high and stable partial current of CO formation on the Ni-N-C catalyst is likely to originate from the readily desorption of CO and sufficiently weak binding of *H, exacerbating HER. Both, the DFT calculation and initial H-Cell tests indicate the Ni-N-C motif to be a fine catalyst for the CO_2RR to CO.

5.4 CO_2RR electrolysis using GDE combined MFC

To assess the technological potential of the Ni-N-C catalysts for industrial CO_2 co-electrolysis, we then turned to single two- and three electrode electrolyzer tests in multi-chambers cell set-ups allowing for pressurized gas flow and circulated electrolyte flows in the cathodic chamber (see Figure 5-5a).

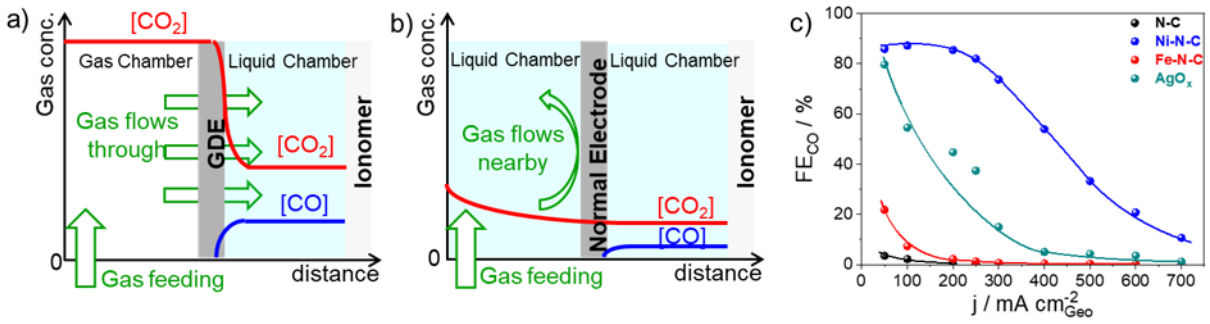

Figure 5- 5 Schematic of a) Ni-N-C Gas Diffusion Electrode (GDE) and b) typical H-type liquid cell. c) Experimental faradaic CO efficiency as function of the applied electrolyzer current density in CO_2 saturated (50 ccm) 1 M $KHCO_3$ solution. Prolonged flow cell CO_2RR testing at 200 mA cm^{-2} working current density is presented in Figure S2-10.

Little solubility of CO_2 is a commonly problematic for CO_2RR in regular CO_2-saturated liquid electrolytes, which cause mass transfer limitation of CO_2 reactant (schematic of GDE and H-cell for CO_2 / CO transfer are presented in Figure 5-5 a and b).[82] To minimize this drawback, the M-N-C catalysts are immobilized in a Gas Diffusion Electrode (GDE) to be able to approach industrial current densities of hundreds mini ampere per geometric electrode area, with a loading of 1 mg cm^{-2}. In principle, the porous nature of the GDE material enables to create a three-phase interface between gaseous CO_2, catalyst layer, and ionic electrolyte.

The electrochemical testing is operated in a current density range between 50 and 700 mA cm^{-2}. Constant current density was held for 2 h for the gaseous products quantification. Shown in Figure 5-5c, the experimentally tested CO faradaic efficiency show distinct dependence on the operated working current densities. Remarkably, the Ni-N-C catalyst GDE reached a maximum FE_{CO} of nearly 90% between 100 to 250 mA cm^{-2}, delivering an over 200 mA cm^{-2} CO evolution activity. Furthermore, such impressive catalytic performance could be maintained for over 20 hours at 200 mA cm^{-2} current density (see Figure S2-10), clearly outperforming the commercial AgO_x control sample.

However, neither the metal-free N-C catalyst nor the Fe-doped one show efficient behavior under the identical operating conditions, which perform parallel with our observation referred to the liquid electrolyte H-Cell tests presented in Figure 5-3. Both catalysts contribute reasonable faradaic efficiency towards CO, but remain in limited working potential of positive than -0.6 V_{RHE}. Predicted by DFT simulation, the Fe-N-C, who have strong interaction with CO, probably poses a CO poisoning. The inferior CO_2RR activity over the metal-free one could be attributed to the absence of active M-N_x functionalities.

5.5 Discussion

In comparison to the regular liquid H-cell, the flow cell coupled with GDEs allows to create 3 phase catalyst interfaces, minimizing mass transfer limitation of the CO_2 reactant. Moreover, a fast CO desorption owing to large interfacial CO_2 could be proposed. Referred to the electrochemical cell design, we suggest utilize the GDE combined MFCs for CO_2 electrolysis, which could realize its commercialization.

Referring to the catalyst benchmark, AgO_x, which reduces to catalytically active metallic Ag at the surface under reaction conditions, is the most commonly deployed catalyst material for alkaline CO_2 to CO electrode. Schmid and co-workers utilized commercial silver-based gas diffusion electrodes and reported FE_{CO} values of up to 90 % (50 to 300 mA cm^{-2}), consistent to data presented in the Summary table 5-1 below.[83] Kenis and co-workers have used a Ag catalyst ink to fabricate GDEs at high catalyst loadings. In their investigations, they achieved 87 % of FE_{CO} at -0.91 V vs. RHE, however, the total current density of 50 mA cm^{-2} remained relatively low.[84] In direct comparison to earlier studies, the Ni-N-C CO_2RR catalysts presented here meet or exceed previous reports of Ag-based catalysts in terms of faradaic CO yield. This demonstrates the great potential of the family of non-metallic M-N-C carbon catalysts, in particular Ni-N-C, for replacing expensive precious group metal catalysts as the benchmark in CO_2 to CO electrolyzers.

Table 5- 1 Summary table of the catalytic performance towards CO_2RR referred to Gas Diffusion Electrode.

Catalysts	Electrolyte	Reported condition	Potential (V_{RHE})	Product efficiency	Reference
NOBLE METAL REFERENCE: Ag-based GDE Cat. Loading: Not given	1.5M $KHCO_3$/ 0.1 M K_2SO_4	300 mA cm^{-2} Working current		FE_{CO}: ~80 % j_{CO}: 240 mA cm^{-2}	[83]Schmid
NOBLE METAL REFERENCE: CD-Ag/PTFE Cat. Loading: Not given	1 M $KHCO_3$	Over 150 mA cm^{-2} Working current	-1.2	FE_{CO}: 90 %	[85] Sargent
	1 M KOH		-0.8	FE_{CO}: 90 %	
M-N-C Candidates: Ni-GS Cat loading: 0.2 mg cm^{-2}	0.5 M $KHCO_3$	-0.75 V vs. RHE Working current below 50 mA cm^{-2}	-0.75	FE_{CO}: 90% j_{Geo}: 60 A g^{-1}	[60] Jiang et al.
M-N-C Candidates: Ni-PANI Cat loading: 1 mg cm^{-2}	1 M $KHCO_3$	50 to 700 mA cm^{-2} Working current	-0.9	CO: ~85% j_{CO}: > 200 mA cm^{-2} (> 200 A g^{-1})	This work

Chapter 6. Tuning the active site density of poly anlinie derived Fe-N-C catalyst using a secondary Nitrogen precursor

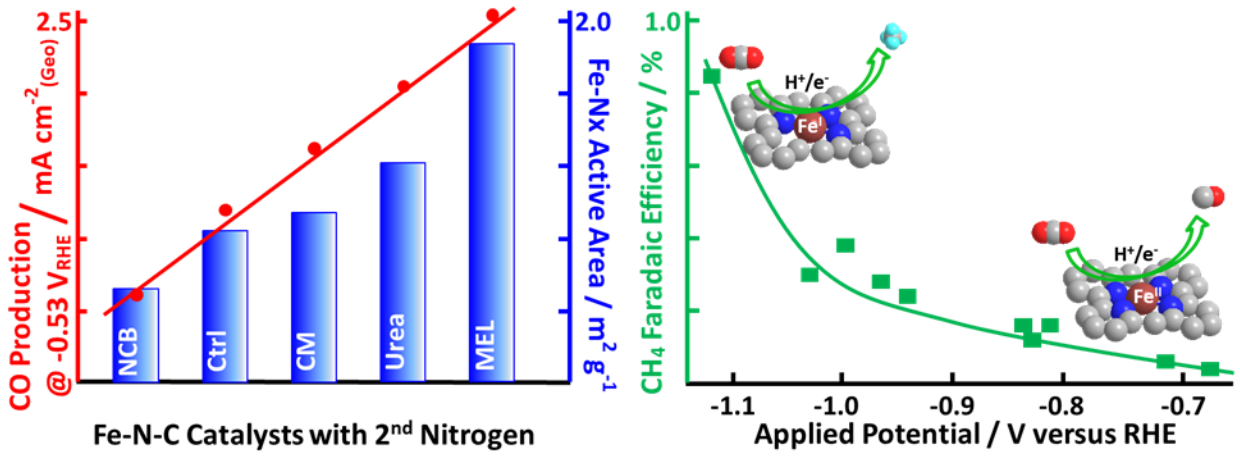

Most parts of this chapter are reproduced from the journal article:

The chemical identity, state and structure of catalytically active centers during the electrochemical CO_2 reduction on porous Fe–nitrogen–carbon (Fe–N–C) materials

Link: https://doi.org/10.1039/C8SC00491A

with permission from Chemical Science, 2018, 9, 5064-5073, as Reference [47] in this dissertation. Copyright 2018 Royal Society of Chemistry (CC BY 3.0).

Author list: Nathaniel Leonard, Wen Ju (co-first), Ilya Sinev, Julian Steinberg, Fang Luo, Ana Sofia Varela, Beatriz Roldan Cuenya, and Peter Strasser

Contributions: N.L., W.J. and I.S. designed the experiments, synthesized and characterized (regularly) the catalysts. I.S. and B.V. carried out the advanced characterization as XPS, ex-situ / operando XAS and subsequent in-depth data analysis. W.J. carried out the electrocatalytic tests and analyzed the results. N.L, W.J. and P.S. aggregated the figures and co-wrote the manuscript. All authors discussed the results, drew conclusions and commented on the manuscript.

Rather than the Ni-N-C catalysts, which could industrial level CO_2 electrolysis, the Fe-N-C based one allows to selectively reduce CO_2 into CO in a lower potential range. In this scenario, we locate our attention on Fe- based M-N-C catalysts and report novel findings. Here, the structure–activity relationships, the chemical state and fine structure of catalytically active sites under operando conditions during the electrochemical CO_2 reduction reaction (CO_2RR) catalyzed by a series of porous iron–nitrogen–carbon (Fe-N-C) catalysts are investigated.

The Fe-N-C catalysts were synthesized from different nitrogen precursors and, as a result of this, exhibited quite distinct physical properties, such as BET surface areas and distinct chemical N-functionalities in varying ratios. The chemical diversity of the Fe-N-C catalysts was harnessed to set up correlations between the catalytic CO_2RR activity and their chemical nitrogen-functionalities, which provided a deeper understanding between catalyst chemistry and function. XPS measurements revealed a dominant role of porphyrin-like Fe–N_x motifs and pyridinic nitrogen species in catalyzing the overall reaction process. Operando EXAFS measurements revealed an unexpected change in the Fe oxidation state and associated coordination from Fe^{2+} to Fe^{1+}. This redox change coincides with the onset of catalytic CH_4 production around −0.9 V_{RHE}. The ability of the solid state coordinative Fe^{1+}–N_x moiety to form hydrocarbons from CO_2 is remarkable, as it represents the solid-state analogue to molecular Fe^{1+} coordination compounds with the same catalytic capability under homogeneous catalytic environments. This finding highlights a conceptual bridge between heterogeneous and homogenous catalysis and contributes significantly to our fundamental understanding of the Fe-N-C catalyst function in the CO_2RR. [47]

6.1 PANI based Fe-N-C catalysts synthesis using a 2nd Nitrogen precursor

In this contribution, the synthesis of the carbon precursor is identical with that presented in Chapter 5, Ketjen EC 600JD (AzkoNobel) was stirred in 0.5 M HCl for 24 hours and vacuum filtered with DI water till completely neutralized. The washed and dried carbon was refluxed in HNO_3 for 8 hours at 90 °C and again vacuum filtered with DI water to neutral pH.

Similar synthesis approach as Chapter 5 is proceed, and 3 ml of Aniline are added into 0.5 liter of 1 M HCl along with 5 g $FeCl_3$ and 5 g Ammonium Persulfate. Specific behavior was done at this point. A secondary nitrogen precursor was added for the purpose to tune the C-N_x cavities amount, to further increase the Fe-N_x site density. For the control catalyst (referred as CTRL), no secondary nitrogen precursor was added during the synthesis steps. The quantity of the secondary precursor is calculated to add 0.333 moles of nitrogen. Various secondary nitrogen precursors (presented in Table 6-1) were chosen to represent common nitrogen precursors[86-93] with varying size and nitrogen contents as summarized in Table 6-1 in the supplemental information. This resulted in 7 g melamine (MEL) or cyanimide (CM), 10 g Urea (UREA), or 23.6 g Nicarbazin (NCB). After one hour of stirring, 0.4 g of pretreated carbon was added. This pretreated carbon has been ultrasonically dispersed in 50 ml of DI water. The resulting mixture was stirred for 48 hours and then dried. After drying, the mixture was ball-milled and heat treated with a ramp of 30°C per minute to 900 °C and kept at this temperature for one hour in a nitrogen atmosphere. After heat treatment, the material was refluxed in 2 M H_2SO_4 overnight and rinsed to neutral via vacuum filtration. After this acid wash, a second identical heat treatment was performed. At least a second acid wash and third heat treatment were performed on each sample. After this third heat treatment, XRD was used to determine whether the sample had been cleaned of excess residual Fe (usually in the form of FeS). If the sample is not clean, a third acid wash and fourth heat treatments were performed (this was the case for CTRL and NCB). These materials have also been explored as oxygen reduction catalysts in a related paper.

Table 6- 1 Characteristics of Secondary Nitrogen Precursors Used in this Work

Nitrogen Precursor	Formula	MW / g mol^{-1}	N/C
Cyanamide	CH_2N_2	42	2/1
Melamine	$C_3H_6N_6$	126	6/3
Urea	CH_4N_2O	60	2/1
Nicarbazin	$C_{19}H_{18}N_6O_6$	426	6/19

6.2 Physiochemical Characterization

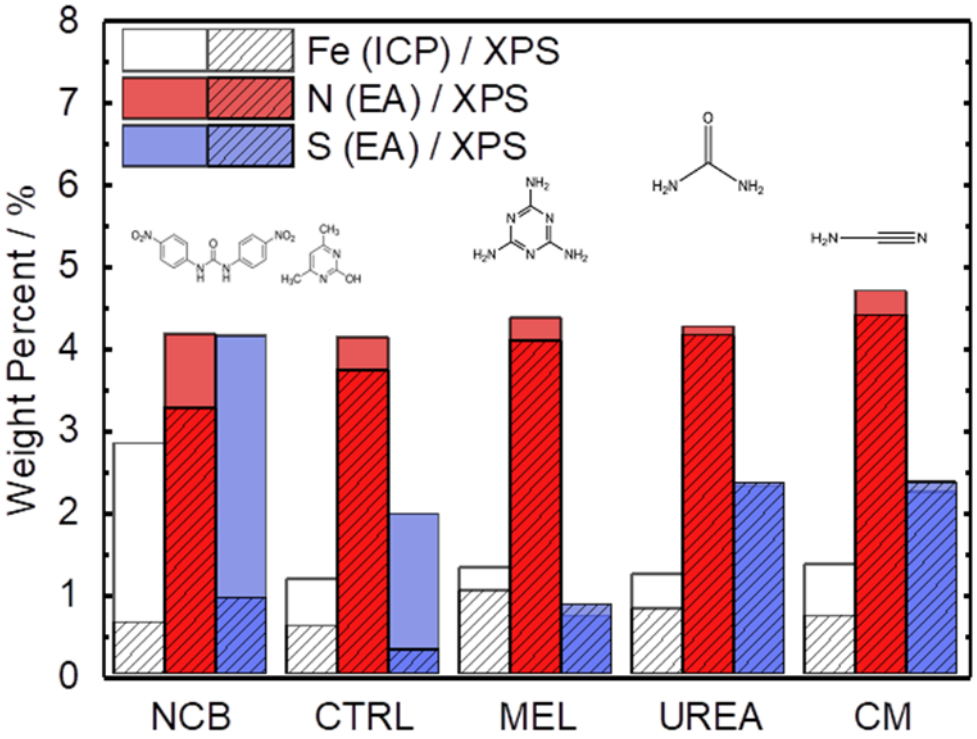

Figure 6- 1 Comparison of Fe-N-C catalysts based on different secondary nitrogen precursors showing bulk iron, nitrogen, and sulfur content as measured by ICP and Elemental Analysis and surface content (ca. 2-3 nm) as measured by XPS. Catalysts ordered by increasing surface nitrogen content (XPS).

This range of PANI-derived Fe-N-C catalysts were synthesized by varying the secondary nitrogen precursor while keeping the iron, carbon, and primary nitrogen precursor (polyaniline, PANI) the same. The secondary nitrogen precursors investigated were melamine (MEL), cyanimide (CM), urea (UREA), and nicarbazin (NCB). These secondary nitrogen precursors cause slight differences in chemistry and morphology. The basic chemical compositions can be seen in Figure 6-1, with a comparison of bulk (EA and ICP) and surface (XPS) measurements. By comparing the bulk (open) and surface (hashed) bars, the surface chemistry can be contrasted with that of the bulk. In general, catalysts tend to be surface sparse in Fe, N, and S. This suggests that the surface is rich in carbon. The only exceptions to this observation are the sulfur content of MEL, UREA, and CM. This difference suggests significant sulfur surface functionalization for these catalysts. It is also interesting that these catalysts also contain the highest surface nitrogen contents. For the other two catalysts (NCB and CTRL), the large discrepancies between bulk and surface iron and sulfur contents are ascribed to FeS that can be detected even after an additional acid wash by XRD (Figure S3-1). These particles cannot be easily washed because they lie below the catalyst surface. The small, bulk/surface discrepancy regarding the nitrogen content may also be attributed to similar iron nitride particles below the catalyst surface. SEM images of MEL and CTRL are shown in Figure S3-2, indicating the similarity of the catalyst morphology. Ex-situ BET measurements and in-situ double layer capacitance of this series catalysts are carried out, and the both techniques nicely agree with each other (Figure S3-3 to S3-5). Further, we performed the CO chemisorption

to quantify Fe-Nx site density in the as-prepared Fe-N-C catalysts, and the data stands in line with the XPS detection (Figure S3-6) according to eq. S3-1 and eq. S3-2. the Analysis of S 2p spectra (Figure S3-7, table S3-1) however shows three doublets at 164.1, 166.5 and 167.7 eV (for $2p_{3/2}$), which can be assigned to thiol,[94] sulfoxide,[95] and sulfone[96] species correspondingly, indicating thus exclusive presence of organic sulfur on the surface formed during acid washing.

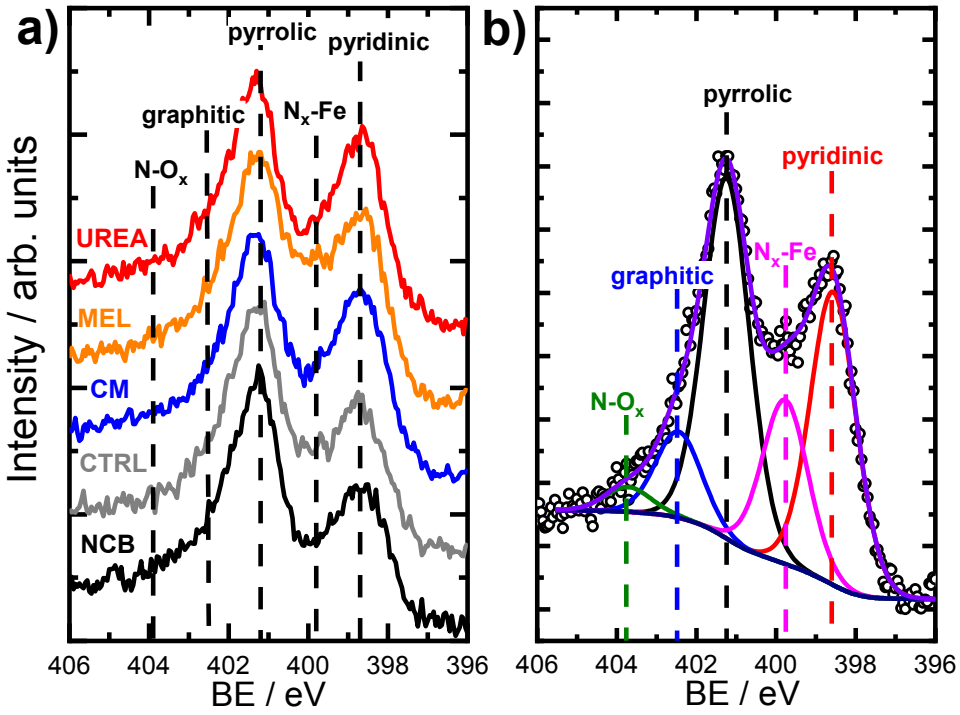

Figure 6- 2 (a) High resolution N 1s XPS data of various PANI-derived Fe-N-C samples with different N precursors. (b) Example of the deconvolution of a N 1s spectrum acquired for the MEL sample. N1s assignment of Fe-PP ref. sample is presented in Figure S3-8, showing identical BE (399.8eV) as the N_x-Fe moiety in MEL sample.

Table 6- 2 Distribution of nitrogen species (in at%) in PANI samples as seen from N 1s XPS spectra deconvolution.

sample	Pyridinic	N_x-Fe	pyrrolic	graphitic	N-O_x
NCB	25.0	12.8	44.1	13.0	5.1
CTRL	28.4	12.6	45.9	10.5	2.6
CM	33.8	12.7	42.1	8.6	2.8
MEL	31.8	17.7	36.9	10.1	3.5
UREA	32.7	12.4	40.3	10.7	3.9
Fe-PP(Sigma-Aldrich)	--	100	--	--	--

Nitrogen 1s XPS region scans are shown in Figure 6-2a. All samples show a similar structure with two dominating peaks at 398.7 and 401.3 eV, indicating prevalence of pyridinic and pyrrolic nitrogen in the structure. A spectral valley between those peaks, where N_x-Fe species are reported,[81] is shallower in the PANI-

MEL sample, pointing to a higher concentration of Fe-porphyrin moieties in those samples. Indeed, a more detailed analysis of the N 1s regions, exemplified by the PANI-MEL sample in Figure 6-2b is summarized in Table 6-2. The N1s spectra of Fe-Protoporphyrin from Sigma-Aldrich is shown in Figure S3-8. Fe 2p spectra of all PANI samples show a similar structure with Fe $2p_{3/2}$ having an intense peak centered at 711 eV and a weak satellite observed around 715.5 eV (Figure S3-9). The structure detected is similar to the shape of Fe $2p_{3/2}$ previously reported for ferrous oxide (FeO).[97,98] It is noteworthy that there are no hints of Fe-N moieties reported at 708 eV (Figure S3-10).[74] Altogether, the analysis of the Fe $2p_{3/2}$ spectra indicates that the most iron seen by XPS is oxidize state Fe(II), while Fe-N_x species, probed indirectly in N 1s spectra (Figure 6-2b and Figure S3-9), must be lying either in the deeper layers or in pores, not accessible to XPS at Fe 2p due to the lower value of the corresponding inelastic mean free path of photoelectrons.[99]

As discussed previously, the discrepancy between surface and bulk iron contents (detected by ICP and XPS as shown in Figure 6-1) indicates the presence of iron species not seen by surface sensitive techniques, e.g. covered by a carbon layer or isolated in pores of the support. To investigate the nature of those species, X-ray absorption spectroscopy (XAFS) measurements were carried out ex situ. X-ray absorption near edge structure (XANES) spectra of selected samples (Figure 6-3a) indicate similar chemical state and coordination of iron. The spectra show a pre-edge feature at ca. 7114 eV, corresponding to a 1s → 3d electronic transition typical for Fe^{3+} in an octahedral local environment. An intense feature above the absorption edge, between 7126 and 7159 V (so-called white line) has however no similarities with the most common iron oxides (Figure S3-11 for comparison), but is well in line with the results published for similar materials.[42,100] The EXAFS spectra plotted on Figure 6-3b, despite looking somewhat alike, have distinct differences in both, peak positions and intensities. The first peak, originating from a light backscatterer, is observed at 1.46 Å (uncorrected for a phase shift) in the PANI-MEL sample and shifts towards shorter distances in PANI and PANI-CM, 1.42 and 1.39 Å (uncorrected) correspondingly. At the same time, the peak intensity is similar in PANI-MEL and PANI-CM samples, while the PANI sample shows a considerably smaller peak. The second backscattering feature between ca. 2.0 and 3.0 Å (uncorrected) is worth special attention. Its location is somehow similar to Fe-Fe backscattering in both common iron oxides with bcc structure (Figure S3-11b), although neither matches exactly in peak position. Zitolo et al assigned a similar structure to crystalline Fe_2N, formed during pyrolysis in NH_3.[42] In our case, formation of nitrides was not observed by any other method. To obtain further details on the local Fe environment, the EXAFS spectra were fitted using an Fe-porphyrin structure[101] as model and the results are summarized in Table 6-3. It is seen that the first coordination shell around Fe can be well described by the FeN_4 moiety. Slight deviations from 4-fold coordination are explained by the interference with iron oxide species which were detected by our surface sensitive XPS method and should be present in the as-prepared ex situ measured samples. The second next neighbor peak observed at ca. 2.4-2.5 Å (uncorrected) is indeed well described by carbon from a porphyrin structure with the real bond distance close to the reference of 3.0 Å. The corresponding coordination number however is significantly lower than 8 in crystalline porphyrin, indicating a highly disordered structure. The latter is also supported by the substantially higher Debye-Waller factors obtained for the PANI samples as compared to the reference iron protoporphyrin sample.

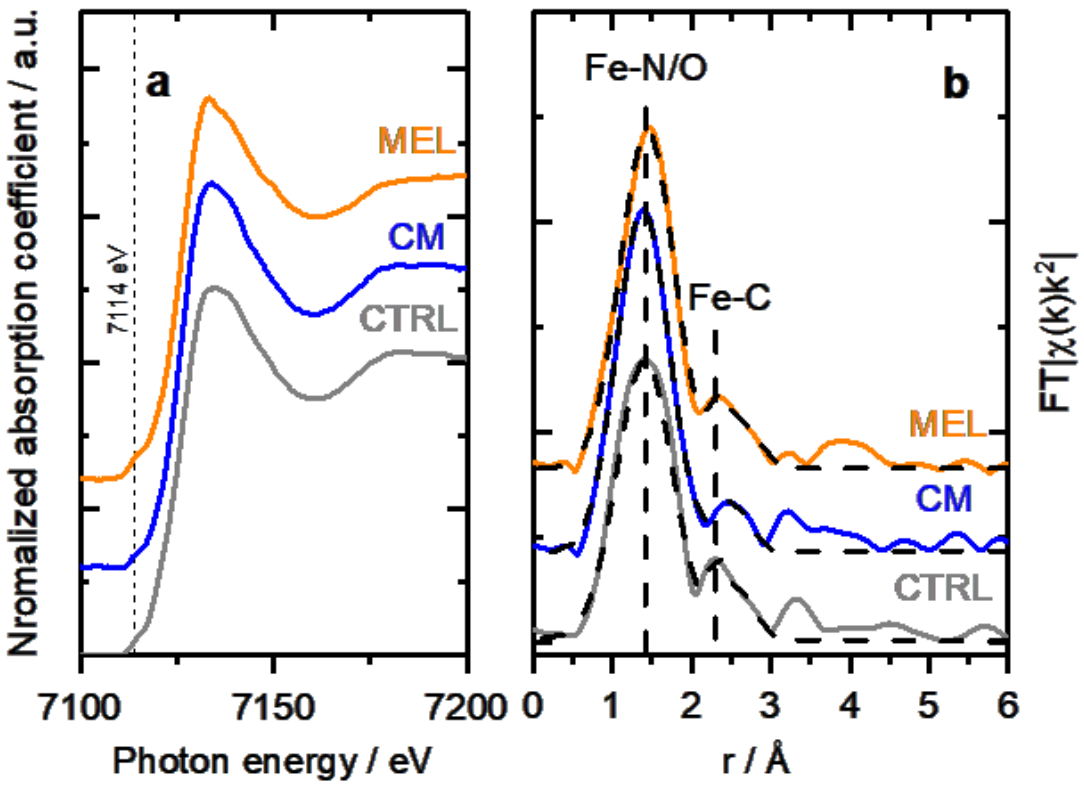

Figure 6- 3 a) Fe K-edge XANES and b) EXAFS spectra of selected Fe-PANI samples, dotted lines in b) show fitted models. XANES and EXAFS spectra of referenced FeOx, Fe foil and FePP (Sigma-Aldrich) are shown in Figure S3-11. Fe K-edge k2-weighted EXAFS data of Fe-PANI samples in k-space and analysis as exemplified by CM sample are shown in Figure S3-12, S3-13.

Table 6- 3 Best-fit parameters for the Fe K-edge EXAFS spectra of the Fe-PANI samples shown in Figure 6-3. Included are the coordination numbers (CN) for Fe-N and Fe-C species, and the bond lengths for the same species (r) and Debye-Waller factor (σ^2). The values in parenthesis are the standard errors in the last digit.

CN_{Fe-N}	r_{Fe-N}, Å	$\sigma^2_{Fe-N}\cdot10^{-3}$, Å^2	CN_{Fe-C}	r_{Fe-C}, Å	$\sigma^2_{Fe-C}\cdot10^{-3}$, Å^2
CM					
3.8(3)	1.98(1)	7.5(6)	1.3(2)	3.0(1)	10.3(9)
CTRL					
3.5(3)	1.99(1)	8.5(7)	1.3(2)	2.8(1)	9.2(8)
MEL					
3.8(2)	2.01(1)	7.3(6)	0.8(1)	2.7(2)	9.8(9)
Fe-PP (Sigma-Aldrich)					
4.0	1.93(1)	4.7(6)	8.0	3.2(1)	4.6(9)

6.3 Correlating CO_2RR performance and physical properties

Now that the catalysts have been described structurally and chemically, this information can be used to better understand the catalysts electrochemical performance. Figure 6-4 shows the CO production rate (a) and CO faradaic efficiency (b) of the various catalysts. From the CO production rate a kinetic region can be identified by the strong increase in performance with decreasing potential between -0.45 and -0.6 V vs RHE. At lower potentials this kinetic region gives way to a plateau with maximum production rates of over 5 mA cm^{-2} for the melamine and cyanamide catalysts. The lack of potential dependence indicated by this plateau suggests that the rate limiting step has shifted to some non-electrochemical process. The faradaic efficiency towards CO production, shown in Figure 6-4b, shows peak faradaic efficiencies occurring around -0.6 V vs RHE with the top performing catalysts being Melamine with 85 % maximum CO efficiency.

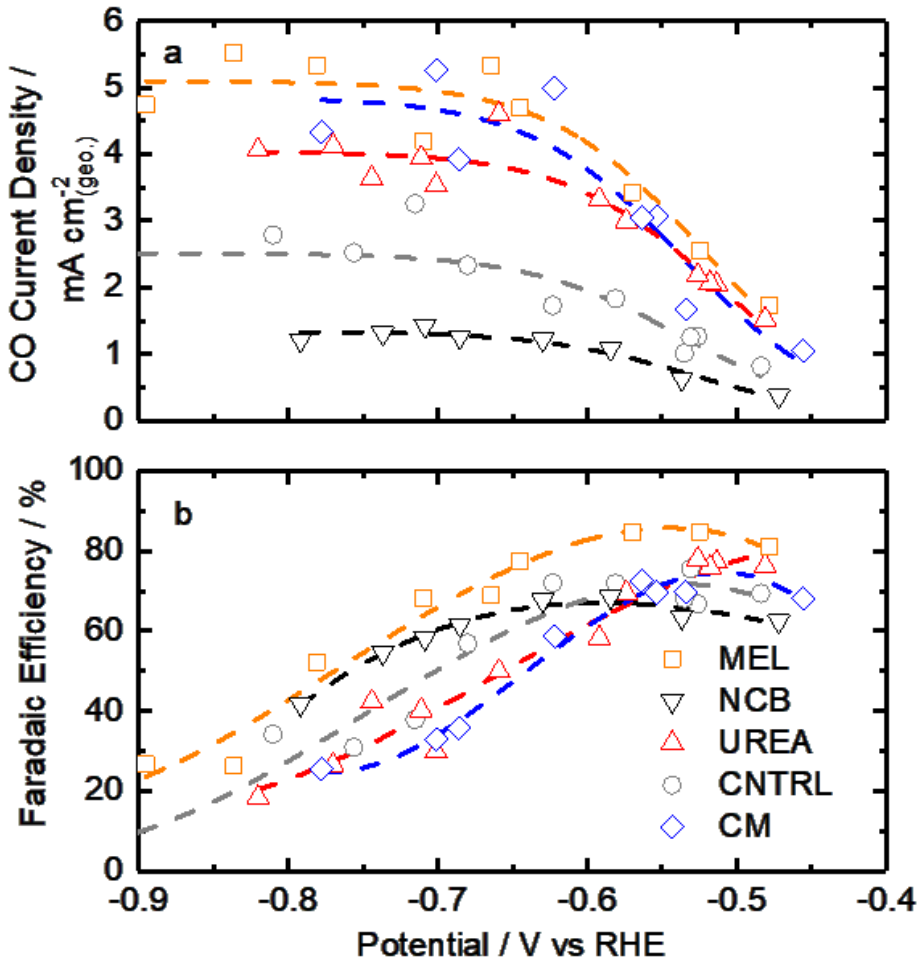

Figure 6- 4 CO_2 reduction data for various Fe-N-C catalysts based on different secondary nitrogen precursors: (a) CO generation rate, (b) faradaic efficiency towards CO production. Experimental conditions: CO_2 saturated 0.1 M $KHCO_3$, catalyst loading: 0.75 mg cm^{-2} on Glassy Carbon.

Comparing Figure 6-4 with the chemical characterizations, it is evident that the addition of the secondary nitrogen precursor has impacted both chemistry and catalyst performance. In order to understand this

performance better, surface area effects must be understood. There is a strong correlation between BET surface area and performance as shown in Figure 6-5. This relationship is not surprising considering the fundamental role of real surface area in heterogeneous catalysis. To reach a deeper understanding of catalysts behavior, the current can be normalized to the real surface area. This will allow a comparison of specific current densities with surface chemistries obtained from XPS results.

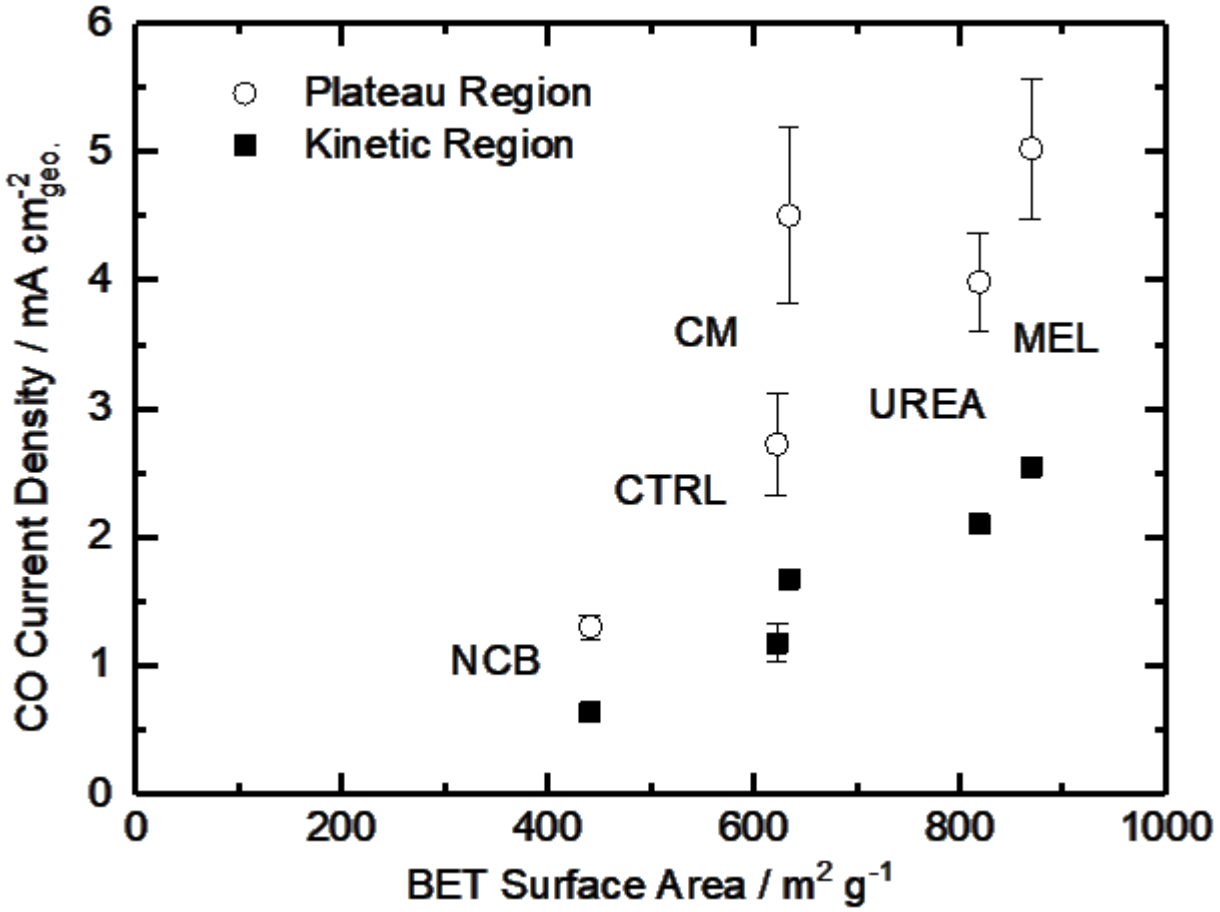

Figure 6- 5 Trends of CO current density on the plateau and in the kinetic region (-0.53 V vs RHE) varying with BET specific surface area.

For a better understanding of the intrinsic catalytic activity of these Fe-N-C catalysts for CO_2-to-CO conversion, specific current densities were calculated by normalizing the current in the kinetic region by the BET surface area, subsequently correlated to the chemical make-up of the surface as measured by XPS. The data show particularly good correlations with N-Fe species (black squares) and pyridinic nitrogen species (open circles) as shown in Figure 6-6a. The N-Fe correlation suggests potentially active Fe-N_x sites, and the pyridinic nitrogen trend is in accordance with its catalytic properties hypothesized by Wu et al. (both mentioned in the introduction).[43,46] Comparing the N-Fe and N-pyridinic correlations, it can be observed that some catalysts have relatively more N-Fe (MEL and CTRL) and some relatively more N-Pyridinic (UREA and CM). This observation leads to the hypothesis that both constituents contribute to the catalytic activity. For this reason, the authors also include a correlation of the specific current density with the sum of N-pyridinic and

N-Fe content (black triangles). The linear fit of the summed data set shows a higher R^2 than either of the other fits. This fit improvement suggests that both sites are likely active.

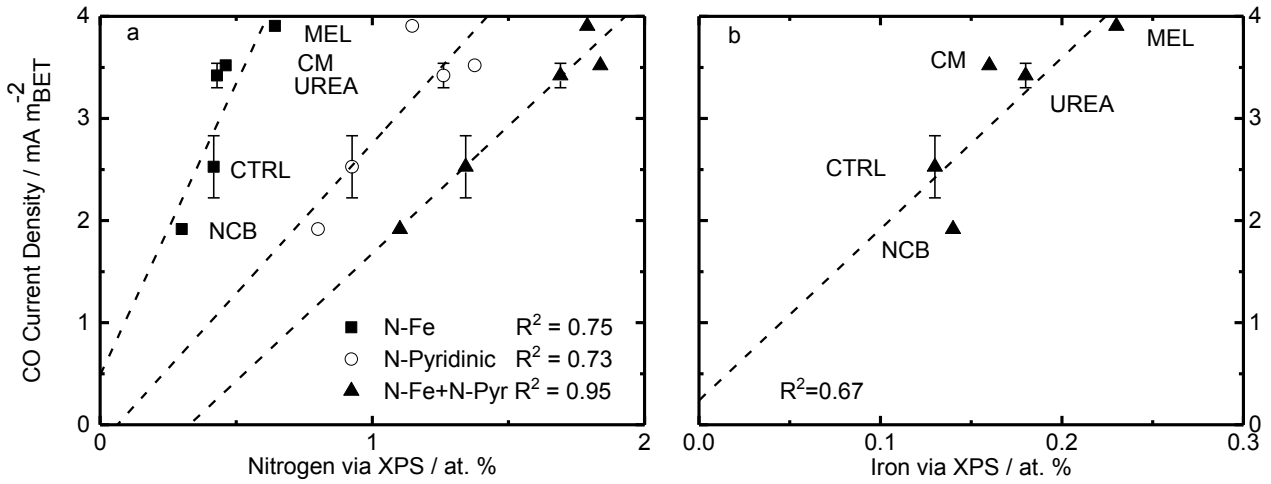

Figure 6- 6 Trends of CO current densities in the kinetic region (-0.53 V vs RHE) varying with (a) various pyridinic nitrogen and N-Fe and (b) surface Fe content. Current density is normalized to the specific surface area as calculated by the BET method. BET-normalized CO current densities in the kinetic region as a function of other functionalities are shown in Figure S3-14 and Figure S3-15. Free Energy Diagrams from CO_2 to CO over FeN_x and Pyridinic-N sites are shown in Figure S3-16, data are adapted from Refs.[45,51]

In addition to the hypothetical nitrogen active sites, literature results have also suggested that trapped iron content near the surface may be an active site for this type of catalysts.[44,102,103] For comparison, Figure 6-6b shows the correlation of specific activity with total iron from XPS. The iron has a poorer correlation than either of the nitrogen constituents, suggesting that this data does not support the hypothesis that encapsulated Fe is an active site for CO_2RR. This uncertainty is compounded by the fact that the Fe peak is small and hard to quantify from XPS and that the samples contained not only Fe-N species, but also FeOx species at/near the surface. The alternative theory that the metallic Fe content is a H_2-generation site is also hard to prove.[44,103] In this case, the melamine based catalyst would be expected to show the highest H_2 faradaic efficiencies (lower CO efficiencies), but this is certainly not the case. In fact, MEL has the highest CO efficiency even though it also has the highest surface metal content.

6.4 Operando X-ray absorption spectra under CO_2RR condition

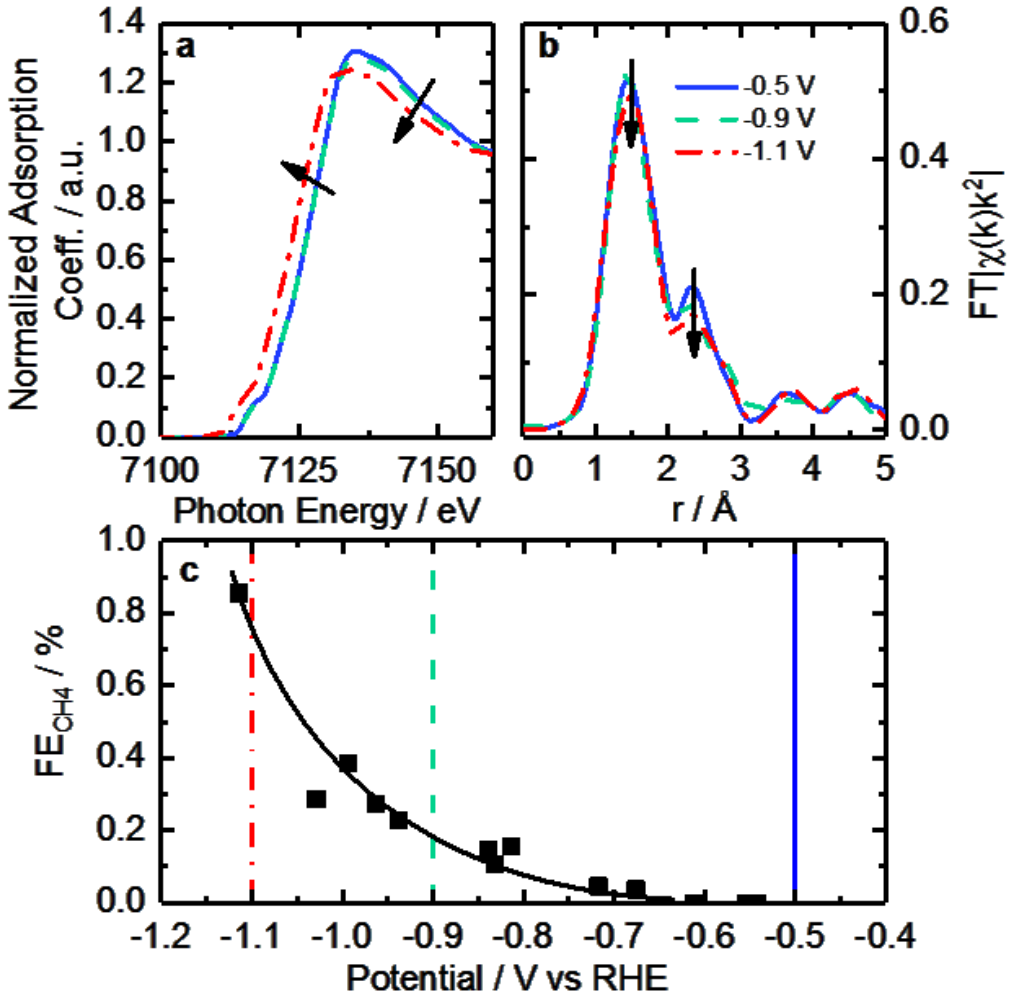

Figure 6- 7 Fe K-edge XANES (a) and EXAFS (b) spectra taken under operando conditions in CO_2-saturated 0.1 M $KHCO_3$ at -0.5 V (solid blue curves), -0.9 V (dashed green curves) and -1.1 V (red dot-dashed curves) vs. RHE a – XANES. (c) CH_4 faradaic efficiency from CO_2RR varying with applied working potential. Lines are added to indicate points representative of spectra in (a) and (b).

Table 6- 4 The best-fit parameters for Fe K-edge EXAFS spectra of the Fe-PANI measured under operando conditions are shown in Figure 6-7. Included are the coordination numbers (CN) for Fe-N and Fe-C species, and the bond lengths for the same species (r) and Debye-Waller factor (σ^2). The values in parenthesis are the standard errors in the last digit.

Potential	CN_{Fe-N}	r_{Fe-N} / Å	$\sigma^2_{Fe-N}\cdot10^{-3}$, Å^2	CN_{Fe-C}	r_{Fe-C} / Å	$\sigma^2_{Fe-C}\cdot10^{-3}$, Å^2
-0.5V_{RHE}	4.3(8)	2.00(2)	6.8(3)	2.6(8)	3.0(2)	8.5(7)
-0.9V_{RHE}	4.2(8)	2.00(2)	7.0(4)	2.4(5)	3.0(2)	8.7(7)
-1.1V_{RHE}	3.9(9)	2.00(3)	7.2(4)	1.8(4)	3.1(2)	9.2(8)

Operando XAFS data were collected to elucidate possible changes in the oxidation state and local coordination of Fe. Scheme of operando-XAS cell is presented in Figure 3-1. Fe K-edge XANES spectra taken under reaction conditions in CO_2 saturated $KHCO_3$ shown in Figure 6-7a display a shift in edge position at -0.9 V vs. RHE (red trace). This shift is similar to that found on related catalysts at around 0.7 V vs. RHE under acidic conditions.[104] That shift was connected to 2+/3+ active site redox behavior which had important implications concerning adsorbate bond strength.[104] Similarly, it is likely that the shift observed in the operando XANES data is correlated to a 1+/2+ redox transition. This redox behavior has been observed for various iron-based macrocycles at similar potentials.[35,105-108] These changes in active site oxidation state and coordination are also supported by changes observed in EXAFS as seen in Figure 6-7b. With decreasing potential, the corresponding spectrum shows a slight decrease of both backscattering features at 1.44 Å (uncorrected), assigned to N/O, and shoulder at 2.35 Å (uncorrected), previously shown to correspond to Fe-C. Thus, the Fe-N/O coordination number decreases from 4.3 to 3.9, while the Fe-C coordination number decreases from 2.6 to 1.8 (see Tables 6-3 and 6-4 for details). The changes observed can be assigned to the reduction of surface iron oxides, detected by XPS, and increasing disorder in the material under reaction conditions.

The redox transition could have a significant impact on binding energies and reaction mechanisms. One of the interesting mechanistic questions concerning these catalysts is the role and prevalence of CO poisoning. It has been suspected that strong CO binding is one of the inhibitors of higher CO_2RR performance as well as the cause of CH_4 production. For that reason, the CO_2 consumption as a function of potential was considered in the hope of seeing significant changes in catalyst behavior. This was accomplished by calculating the ratio of CH_4 production to total CO_2 consumed as shown in Figure 6-7c. Observable in this figure is a strong increase in CH_4 production between -0.9 and -1.1 V vs. RHE. The correspondence of this increase with the changes in coordination and redox behavior indicated by EXAFS suggests that the binding behavior of reactants may indeed be modified during this potential change. This observation is consistent with a proposed mechanism for photochemical methane formation on a potentially similar iron-based macrocycle catalyst.[107] In the proposed mechanism the Fe 1+/2+ transition plays an integral role in the conversion of CO into CH_4 via a formyl intermediate.[107] This theory is consistent with our observations of increased CH_4 production, changed oxidation state, and decreased coordination. All together, we hypothesize that these FeNx sites would provide enough room and proper binding energy for proton binding, facilitating the intermediate CHO*, which might be the rate-limiting step for CH_4 formation. Despite the lack of systematic theoretical simulations, this mechanistic change has significant implications for future catalysts development. Specifically, for actives sites that are nitrogen-coordinated iron complexes, it is possible to adjust the iron center redox potential by adjusting ligand number/strength. This adjustment of iron center redox behavior or coordination number could be used to synthesize catalysts with higher CH_4 yields. Conversely, it may be possible to inhibit CO-poisoning by tuning iron complexes to have lower Fe 1+/2+ redox potentials. Unfortunately, such a study is difficult on the present set of catalysts and would require a following work that looked at CO_2RR on a set of Fe-macrocycles with varying metal center electron density of states. Such a study is outside the scope of this work.

6.5 Discussion

In the present work five different FeNC CO_2RR catalysts have been explored with two goals: 1. synthesizing high performance, inexpensive CO_2 reduction catalysts for aqueous media, 2. increasing our fundamental understanding of the active state and structure of FeNC catalysts during the CO_2RR process. Towards the first goal, the melamine based Fe-PANI catalyst achieved a CO efficiency of 85% and a two-fold improvement in CO production rate resulting in current densities of over 5 mA cm^{-2}.

Towards our second goal of increasing understanding of M-N-C catalysts we have three additional conclusions. Firstly, high specific surface areas are important to catalytic activity. This suggests that reaction rates are limited by adsorption and/or kinetics (i.e. surface events). Secondly, the comparison of specific current density with XPS data on the surface indicates that both N-Fe and pyridinic species are likely actives sites. Finally, operando EXAFS results indicate a reduction in metallic content between -0.9 and -1.1 V vs. RHE which corresponds with the redox potential of Fe $1^+/2^+$. This event coincides with an increase in CH_4 production, which suggests a change in active site behavior. The authors hypothesize that this change in behavior is a change in reaction mechanism that results in the onset of CH_4 production.

Chapter 7. Unraveling the mechanistic insight of Electrochemical CO_2 Reduction to Methane on the Fe-N-C Catalyst

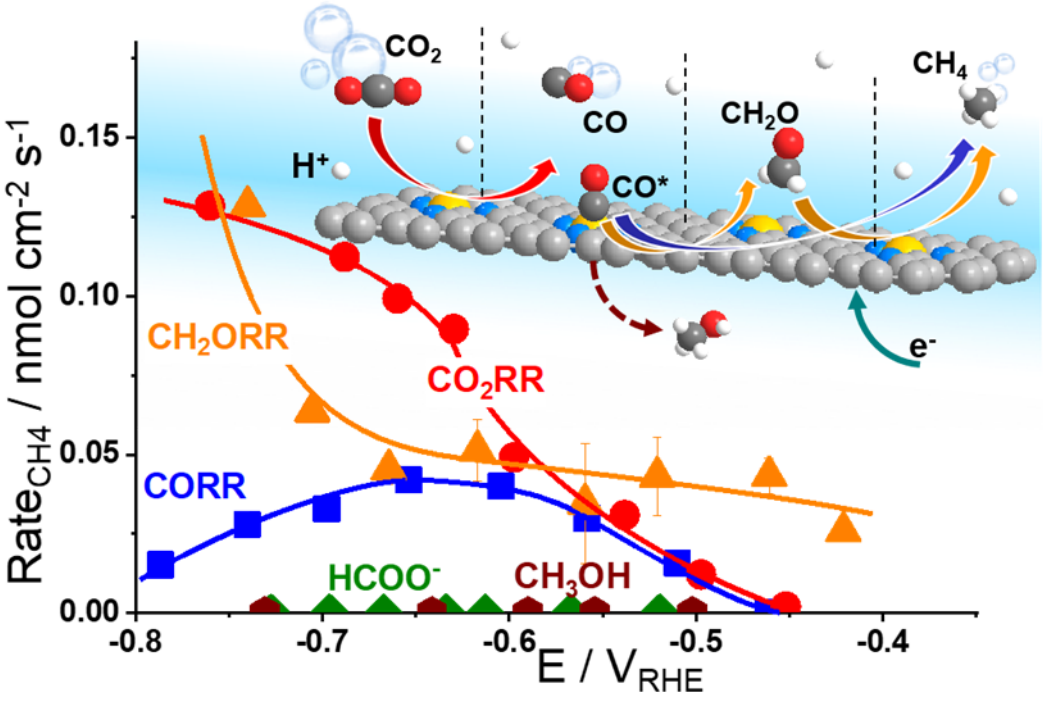

Most parts of this chapter are reproduced from the journal article:

Unraveling Mechanistic Reaction Pathways of the Electrochemical CO_2 Reduction on Fe-N-C Single Site Catalysts

Link: https://doi.org/10.1021/acsenergylett.9b01049

with permission from ACS Energy Letters, 2019, , 5064-5073, as Reference [109] in this dissertation. Copyright 2019 American Chemical Society.

Author list: Wen Ju, Alexander Bagger, Xingli Wang, Yulin Tsai, Fang Luo, Tim Möller, Huan Wang, Ana Sofia Varela, Jan Rossmeisl, and Peter Strasser

Contributions: W.J. and A.B. designed and combined the experiments and simulations. W.J. and A.B. co-wrote the article. Other co-authors contributed characterization data and analysis.

In this work, we report an experimental-computational study of mechanistic reaction pathways during the electrochemical reduction of CO_2 to CH_4, catalyzed by solid-state, single-site Fe-N-C catalysts. Fe-N-C catalysts feature molecularly dispersed catalytically active Fe-N motifs and represent a type of non-Cu-based catalysts that yield "beyond CO" hydrocarbon products. The various multi-step mechanistic pathways toward hydrocarbons with these catalysts has never been studied before and is the focus of this study. A number of different reactant molecules with varying formal carbon redox states, more specifically CO_2, CO, CH_2O, CH_3OH and formate were electrochemically converted at the Fe-N sites, yet only CO_2, CO and CH_2O could be protonated into methane. Also, we observed a distinctly different pH dependence of the catalytic CH_4 evolution from CO and CH_2O, suggesting differences in the proton participation of rate determining steps. In comparing the experimental observations with Density Functional Theory (DFT) -derived Free Energy Diagrams of reactive intermediates along the reaction coordinates, we unraveled the distinctly different dominant mechanistic pathways and roles of CO and CH_2O along the catalytic CO_2-to-CH_4 cascade and their rate-determine-steps (RDS). We close with the first comprehensive reaction network of the CO_2 electroreduction on a M-N-C catalyst. Our findings offer valuable insights in the catalysis of the CO_2RR on single site Fe-N-C catalysts that may prove useful in developing efficient, non-Cu-based catalysts for direct electrochemical hydrocarbons production. [109]

7.1 Catalysts preparation and regular characterization

The poly-aniline-derived single-site Fe-N-C catalysts with atomically dispersed Fe-N_x moieties employed here are identical to those described and characterized in our previous work.[41,47] To ensure the role of the atomically dispersed Fe-N_x motifs, an iron-free, yet otherwise identical N-C catalyst was prepared as used as a control. Conventional ex-situ characterization of physico-chemical properties of the Fe-N-C material is shown in Appendix 4 (Table S4-1, Figure S4-1, S4-2, and S4-3). X-ray Diffraction patterns (XRD, Figure S4-1) and Transmission Electron Microscopy (TEM, Figure S4-2) indicated that the Fe-N-C catalyst had similar amorphous carbon structure as the metal-free N-C one. N_2 specific adsorption and double layer capacity measurements were carried out, that suggested comparable surface areas (Figure S4-3) of Fe-N-C and N-C. Elemental analysis revealed the same or similar nitrogen content in the two catalysts, and absence of Fe in the control (ICP). CO sorption confirmed absence of CO adsorbing centers in the control (Table S4-1). Moreover, the dispersed single site Fe-N_x motifs were identified and confirmed using N1s X-ray photo electron emission spectroscopy,[43,47] Mossbauer spectroscopy,[41] and also X-rays absorption spectroscopy[47] in our previous approaches (Chapter 5 and Appendix 2). All these confirm the dominant character of the coordinative Fe-N_x motifs in our Fe-N-C model catalyst, whereas the inorganic iron species remain in trace portion, catalytically not responsible for methane evolution.[4]

7.2 Products spectrum of prolonged CO_2RR and CORR on Fe-N-C catalyst

Upon electrochemical reduction of CO_2 using CO_2-saturated electrolytes in an H-cell, CO, H_2 and CH_4 were identified as the main CO_2RR products over the Fe-N-C catalyst.[47,48] The overall faradaic efficiency reached 95% during bulk electrolysis tests at constant electrode potentials. Liquid products such as alcohols, aldehydes and formate were below the detection limit for the typical present electrolysis time of 75 min. However, we also performed a few longer-term, 1000 min CO_2RR experiments (see Table S4-2). Similarly, prolonged CO reduction reaction (CORR) was carried out in buffered potassium phosphate solution for 480 min at the same pH. Now, very small, yet clearly detectable amounts of both methanol and formaldehyde were found during these longer term electrolysis tests (see Figure S4-4 and S4-5), demonstrating that these two compounds are apparently involved in the mechanistic network of the CO_2RR as well as of the CORR over the Fe-N-C catalyst.

7.3 Electrochemical reduction of a set of different CO_xH_y molecules

To get insight in the electrochemical CO_2-to-CH_4 reaction pathways, CO_2, CO, CH_2O, CH_3OH and formate were used separately as feed reactants in order to investigate their relative reaction rates and resulting product spectra. The choice of these feeds was based on the fact that all of them may constitute reactive intermediates of the CO_2RR process. In particular, we were interested whether and to what degree these potential reactive intermediates can be electrochemically reduced to CH_4 on the Fe-N-C catalysts, which carries useful insight in the catalytic CO_2-to-CH_4 reaction cascade. Table S4-2 lists the reaction parameters used in the experiments. The formal chemical transformations and their standard potentials read:

$$CO_2 + 8(H^+ + e^-) \rightarrow CH_4 + 2H_2O \qquad E_0 = +0.17\ V_{RHE} \qquad \text{eq. 7-1}$$

$$HCOOH + 6(H^+ + e^-) \rightarrow CH_4 + 2H_2O \qquad E_0 = +0.28\ V_{RHE} \qquad \text{eq. 7-2}$$

$$CO + 6(H^+ + e^-) \rightarrow CH_4 + H_2O \qquad E_0 = +0.26\ V_{RHE} \qquad \text{eq. 7-3}$$

$$CH_2O + 4(H^+ + e^-) \rightarrow CH_4 + H_2O \qquad E_0 = +0.45\ V_{RHE} \qquad \text{eq. 7-4}$$

$$CH_3OH + 2(H^+ + e^-) \rightarrow CH_4 + H_2O \qquad E_0 = +0.63\ V_{RHE} \qquad \text{eq. 7-5}$$

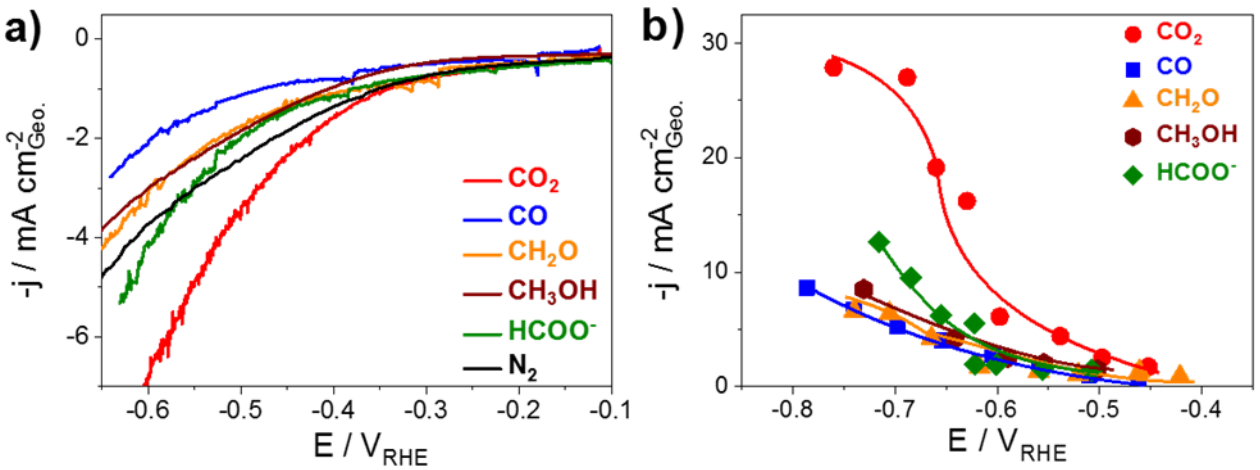

Figure 7-1 Overall electrochemical performance under different conditions and in presence of various reactants in neutral 0.05M K_3PO_4 + 0.05M H_3PO_4 solution. a) Linear sweep voltammetry at -5 mV s^{-1} potential scan rate and b) geometric current density during each bulk electrolysis. Presented dots data are averages calculated from 15 min, 45 min and 75 min of the stationary electrochemical reaction. Line to guide the eye. Catalyst loading: 0.75 mg cm^{-2} on glassy carbon.

The overall electrocatalytic polarization behavior comprising all cathodic processes were studied for each individual feed molecule using transient linear sweep voltammetry (LSV) (Figure 7-1a) and stationary bulk electrolysis (Figure 7-1b). Reactivity trends of transient and stationary measurements matched well. CO_2 outperformed the HER control activity (N_2 as feed in Figure 7-1a), largely thanks to significant CO evolution

(Figure S4-6) below -0.4 V_{RHE}. CO_2 was followed by formic acid, while the other reactants exhibited faradaic currents comparable to the HER background. CO feeds, likely due to its site blocking nature, displayed lower currents than the background (Figure 7-1a). Liquid products remained below the detection limit. Methane formation, however, was observed for CO_2, CO and CH_2O feeds (Figure 7-2) and became the primary focus of subsequent kinetic studies.

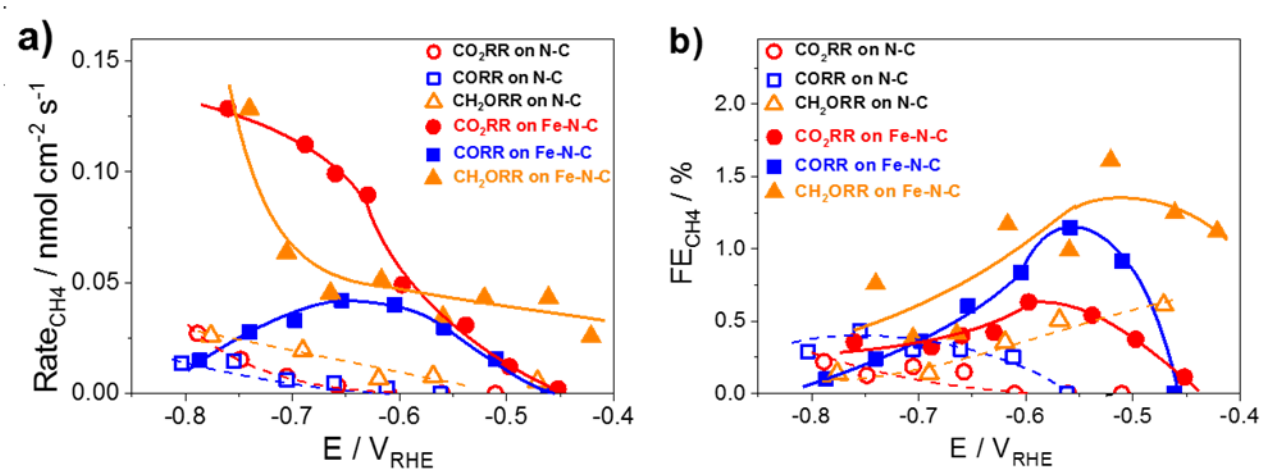

Figure 7- 2 Methane a) production rate and b) faradaic efficiency as a function of applied IR-free potential during the electrochemical CO_2 (saturated, 30 mM), CO (saturated, 1 mM) and CH_2O (1 mM) reduction reactions on Fe-N-C (solid dots) and metal free N-C (empty) catalysts in neutral 0.05 M K_2HPO_4 + 0.05 M KH_2PO_4 buffer solution. Data points are averages obtained from 15 min, 45 min and 75 min of each bulk electrolysis. Line to guide the eye. Catalyst loading: 0.75 mg cm^{-2} on glassy carbon plate.

First, we analyzed how the CH_4 formation rate changed with applied potential. Figure 7-2 shows the potential-dependent electrocatalytic methane production rate and the faradaic methane efficiency for each feed on Fe-N-C catalysts (solid symbols) and Fe-free "N-C" control (open symbols) catalysts. The Fe-free catalysts displayed little to none CH_4 yield, evidencing the catalytic role of the Fe-N_x single sites in the CO protonation process. Closer inspection of Figure 7-2 reveals more anodic CH_4 onset potentials under CH_2O feeds compared to CO or CO_2 feeds. This suggests that CH_2O activation and subsequent protonation to methane is fast, while activation barriers in the catalytic cascade from CO_2 or CO to CH_2O appeared to delay their reduction kinetics. Indeed, the fact that the CH_4 yields under CO_2 and CO feeds track each other so closely is an indication that they are kinetically limited by a shared elementary process, more specifically the protonation of adsorbed CO, *CO. Note that we will abbreviate surface adsorbed species with an asterisk on the left to symbolize a surface site that binds to the element adjacent to it. All three feeds showed steadily increasing catalytic CH_4 formation rates with increasing applied overpotential up to -0.65 V_{RHE}. Beyond -0.65 V_{RHE}, catalytic CH_4 rate hikes with potential slowed down for CO_2, yet increased sharply for CH_2O. For CO feeds, the CH_4 formation rates actually peaked and subsequently dropped slightly at more cathodic potentials. We attribute this distinct kinetic behavior to the poisoning effect of adsorbed *CO on the FeN_4 sites due to their strong binding, which will be supported later by computational analysis.[13,15,17] For CO_2, even though its saturated bulk concentration is about

30 times that of CO, local depletion in CO_x concentration at the double layer will limit sustained CH_4 formation rates at sufficiently cathodic potentials. Cathodically of -0.65 V_{RHE}, the CH_4 formation rate from CH_2O displayed a sudden growth suggesting a shift in the rate-determining reaction step. We want to point out that previous kinetic studies invariably showed that the electroreduction of aldehydes on metallic electrocatalysts exclusively generated the respective primary alcohols.[15,110,111] Here, however, the solid non-metallic, single site Fe-N-C catalysts with graphene-embedded molecular sites generated selectively the respective hydrocarbon (CH_4). This is consistent with results on molecular catalysts and suggests mechanistic analogies between molecular and solid state catalysts.[33]

Next, we investigated the CH_4 formation rate and its faradaic efficiency as a function of the initial CH_2O concentration in the electrolyte, see Figure S4-7. The CH_4 yield and its FE scaled nearly linearly with the CH_2O concentration at a given applied potential, with the slope varying with the applied potential. This suggests the CH_4 rate law is approximately first order with respect to CH_2O, which was confirmed in kinetic log-log analysis (see Figure S4-8).

7.4 Proton- coupled and decoupled reaction steps

The generation of CH_4 during the electrochemical reduction of CO_2 on Fe-N-C (and similarly on molecular Cobalt-Protoporphyrin) is known to show a Nernstian dependence on pH,[33,47] suggesting that the rate-determining protonation of adsorbed *CO does involve a concerted proton-coupled electron transfer (PCET). To verify this, we studied the pH dependence of the CORR on the single site catalysts. Results in Figure 7-3a and 7-3c confirmed the Nernstian behavior of the CH_4 onset potentials and CH_4 formation rates, evidenced by the 59 mV shift per pH unit on the NHE scale. Thus, on the present Fe-N-C single site catalysts, experiments suggest the protonation of *CO at the carbon atom to *CHO to be the slowest and thus rate-determining step in the CORR pathway to methane. This will be compared to computational predictions further below.

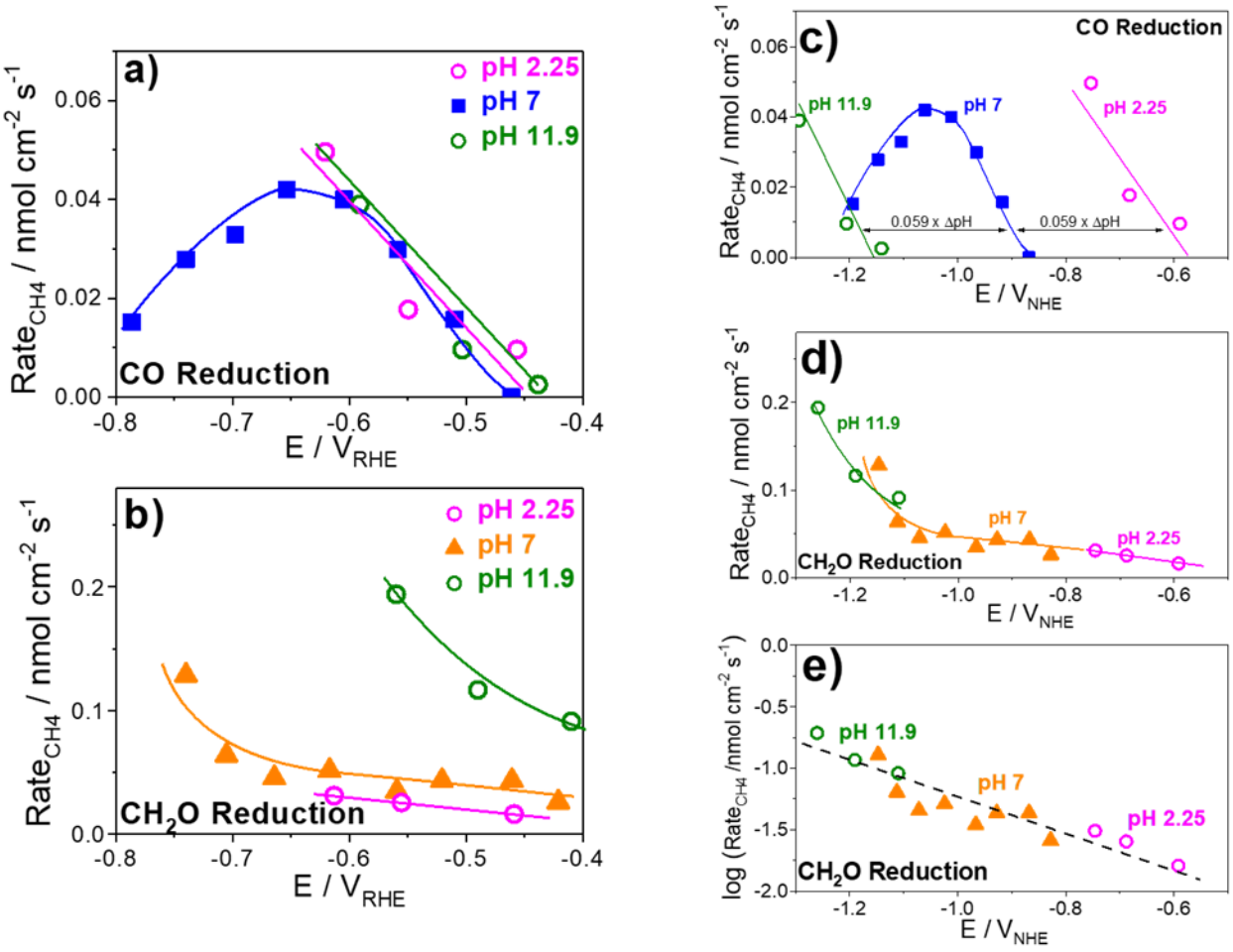

Figure 7- 3 Production rate of CH_4 at various pH as a function of iR-corrected applied electrode potentials. a) CO reduction and b) CH_2O reduction plotted on the RHE scale. c) CO reduction and d) CH_2O reduction plotted on the NHE scale. e) logarithm of the CH_4 formation rate from CH_2O at different pH versus applied potential. Electrolytes are 0.05 M K_2HPO_4 + 0.05 M K_3PO_4 (pH = 11.9), 0.05 M K_3PO_4 + 0.05 M H_3PO_4 (pH = 6.9), and 0.05 M KH_2PO_4 + 0.05 M H_3PO_4 (pH = 2.25) for pH variation. Data are averages over 75 min electrolysis. Line to guide the eye. Catalyst loading: 0.75 mg cm^{-2} on glassy carbon.

Similar pH tests were then conducted using CH_2O as reactant feed (see Figure 7-3b, 7-3d, and 7-3e). Now, the CH_4 onset potentials exhibited close to none pH dependence on the NHE scale (Figure 7-3d), yet did so on the RHE scale (Figure 7-3b). We conclude that the catalytic pathway from CH_2O to CH_4 is limited by a proton-decoupled electron transfer (PDET) step resulting in an experimental rate law following

$$Rate_{CH_4} \backsim k\ e^{-\alpha\eta}[CH_2O]^1[H^+]^{\sim 0} \qquad \text{eq. 7-6}$$

where k is a heterogeneous rate constant, the exponential term describes the rate dependence on the applied cathodic overpotential $\eta\ [V]$ and $\alpha[V^{-1}]$ denotes a parameter related to the inverse Tafel slope.

To summarize our experimental findings on Fe-N-C catalysts, the CO_2RR as well as the CORR generally exhibit a wider range of products, primarily CO, methane, as well as some formaldehyde and methanol. The CH_2ORR exclusively yields CH_4. Both the CO_2 to CO reaction and the CH_2O to CH_4 reactions appear to be rate-limited by a slow proton-decoupled electron transfers (PDET), while the CO to CH_4 reaction features a concerted proton-coupled electron transfer (PCET) as its slowest step. Mechanistic DFT calculations are now needed to rationalize the experimental findings and to establish a full mechanistic network.

7.5 Density Functional Theory Calculation

DFT predictions of possible mechanistic pathways from CO_2 to CH_4 were carried out by calculating the Free Energy of possible intermediates on single-site Fe-N_4-C motifs at 0 V_{RHE}. This particular metal coordination was chosen, because iron sites generally prefer four coordinative nitrogen (DFT calculation details see Experiment Section).[47]

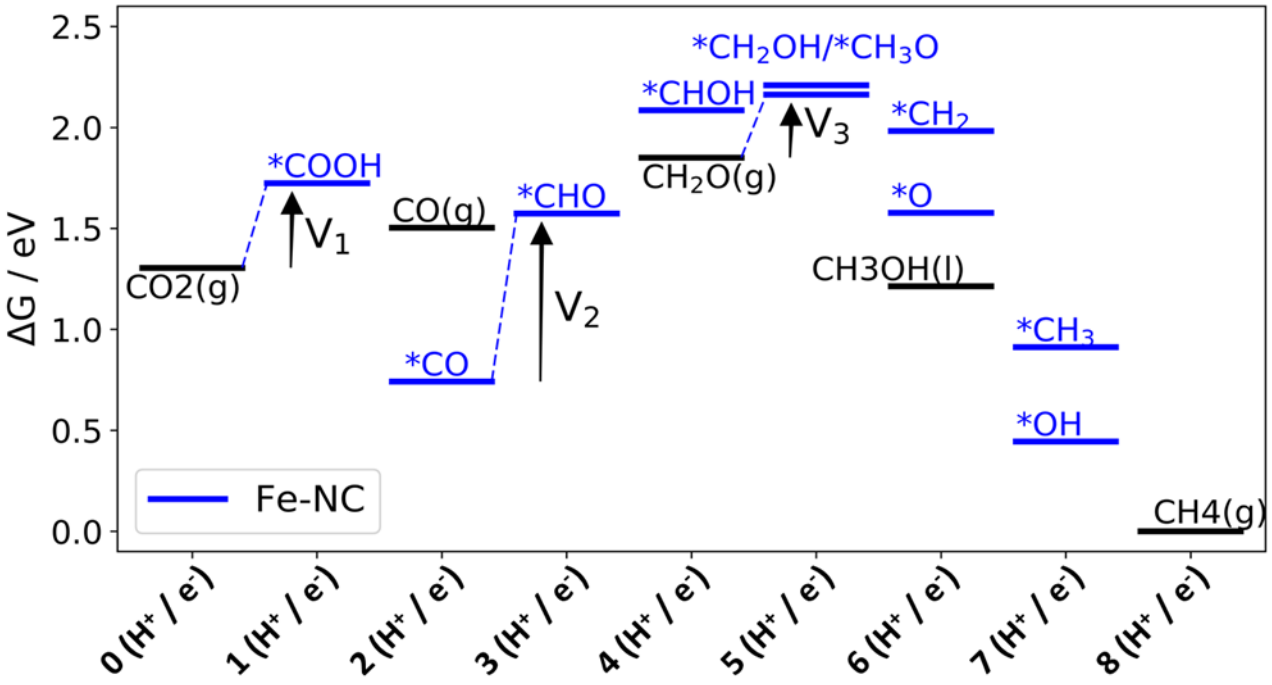

Figure 7- 4 Free energy diagram towards CH_4 from CO_2, CO and CH_2O on Fe-N-C at 0 V_{RHE}. The three limiting potential steps are shown by V_1, V_2 and V_3, with the reduction of CH_2O having the smallest limiting potential step in line with the experiments.

Figure 7-4 presents the free energy network diagram of the individual reaction pathways from the different reactants to methane. The calculations are assuming concerted proton electron transfer, are evaluated at 0 V_{RHE} and with reference made to CH_4 (g), as this reference is common for the reactions investigated. It shows that Fe-N_4-C binds *CO relatively strongly and the most difficult step from CO_2/CO to CH_4 is the protonating *CO to *CHO (V_2: ΔG_{*CO} to ΔG_{*CHO}). Indeed, the *COH has also been proposed as the first reduced intermediate following *CO on metallic Cu facets.[112,113] However, considering that the M-N-C type catalysts contribute isolated active sites, the free energy of *COH intermediate is about 1.5 eV higher than that of *CHO, possibly accommodating an unfavourable triple bond between Fe-N_x and the *COH intermediate.

In comparison, the reduction of CO_2 to CO (V_1: ΔG_{CO2} to ΔG_{*COOH}) and CH_2ORR to CH_4 (V_3: ΔG_{CH2O} to $\Delta G_{*CH2OH/*OCH3}$) exhibit lower energetic pathways, leading to less potential requirement to drive these two conversions, which is in line with the experiment observations (see Figure 7-2 and Figure S4-6).

We firstly focus on a discussion of the selectivity of the reduction of CH_2O, CH_2ORR. Notably, no methanol was observed over Fe-N-C catalysts, which is distinctly different from metals (Cu, Ag and Au), which majorly

produces methanol. Previously, for metal catalyst we tried to classify the two types of products from aldehyde reductions to be a matter of choice: oxygen bonding ($*OCH_3$) gives alcohols while the carbon bonding ($*CH_2OH$) leads to fully reduced hydrocarbons.[15] Nevertheless, we do observe that the calculated $*CH_2OH$ and $*OCH_3$ for the Fe-N-C on free energy scale are similar (see Figure 7-4). Given the fact that CH_2O reduction on Fe-N-C only produces CH_4, we thus propose that uniquely this catalyst offers a special reaction path or has a very different water stabilization as compared to the normal metal catalyst. Water indeed highly influence the stabilization of CO_2RR intermediates for Cu facets[114] and for ORR/OER intermediates water solvation has been shown to be different on M-N-C systems as compare metals.[115] Investigating water dynamics on the M-N-C for this analysis was found to be challenging due to the spin-polarized nature of the calculations. This issue could be addressed with ab initio molecular dynamics (AIMD) of water on the M-N-C system, which is out of scope of the present study.

Secondly, we turn to the pH dependency of these reactions, where, the CO_2RR into CO (performed in our early work[116], data is presented in Figure S4-9) and CH_2ORR into CH_4 showed a non-Nernstian behavior, while the CO-to-CH_4 process followed a Nernstian one. We hypothesize that a proton-decoupled electron transfer (PDET) is the key to rationalize this pH dependence. A proton-decoupled electron transfer was reported to be more likely if the interaction of the intermediates with the catalyst is weak.[117] Based on this, for weakly bound species, the adsorption becomes a slow rate determining step (RDS) and the reaction is limited by a proton decoupled electron transfer (ET) as shown in the equations below:

$$CO_2 + * + e^- \rightarrow *CO_2^- \qquad \text{eq. 7-7}$$

$$CH_2O + * + e^- \rightarrow *CH_2O^- \qquad \text{eq. 7-8}$$

accounting for the experimentally observed pH independent catalytic rates on the NHE scale. However, our DFT calculations using the Computational Hydrogen Electrode (CHE) assumes a concerted proton-electron transfer (equivalent to PCET), thus could not capture the feature of the PDET. Previous investigations have indeed shown the simulation of stable M-N-C-CO_2^- transition states,[33,118] however, without clearly pointing the reference potential for such proton decoupled electron transfer. This implies that both models have their limitations to clearly describe the electrocatalytic process. The experiments, however, provide important information about the reaction mechanism.

We now turn to the discussion of the relatively low (yet finite compared to methanol) methane selectivity on the Fe-N-C catalyst. The Fe-N_4 motifs show similar "binding" properties as copper (the well-known excellent hydrocarbons producer), holding the ability to bind *CO without having *H under potential deposited. Upon this, to better understand the performance difference in CH_4 selectivity of these two types candidates, we compared the proton transfer details of the *CO-to-*CHO steps on the single-site Fe-N_x motif and the extended metal Cu (111) facet.[119] Illustrated in Figure 7-5, comparable PCET barriers (marked as V_2 in both Figure 7-5a and 7-5b, ΔG_{*CO} to $\Delta G_{*CHO,}$ ~1eV) could be observed on these two candidates. For the Cu (111) facet, a pre *H / *CO co-adsorption (schematic is displayed in Figure 7-5a) is energetically favored, leaving V_2 (~1eV) as the major limiting step. This is in agreement with a recent work focusing on CH_4 evolution via CORR on Cu

based catalyst,[120] suggesting that the protonation of adsorbed *CO into *CHO (RDS of CH_4 formation) is preferentially via the "Langmuir-Hinshelwood" reaction channel (*CO + *H → *CHO). On the contrary, on Fe-N-C motif, the co-adsorption of *CO / *H step (V marked in Figure 7-5b) sets the main dynamic barrier, emerging as the limiting step and resulting in low hydrocarbon activity and forcing to a "Eley-Rideal" type protonation step ($*CO + H^+_{sol} + e^- \rightarrow *CHO$).

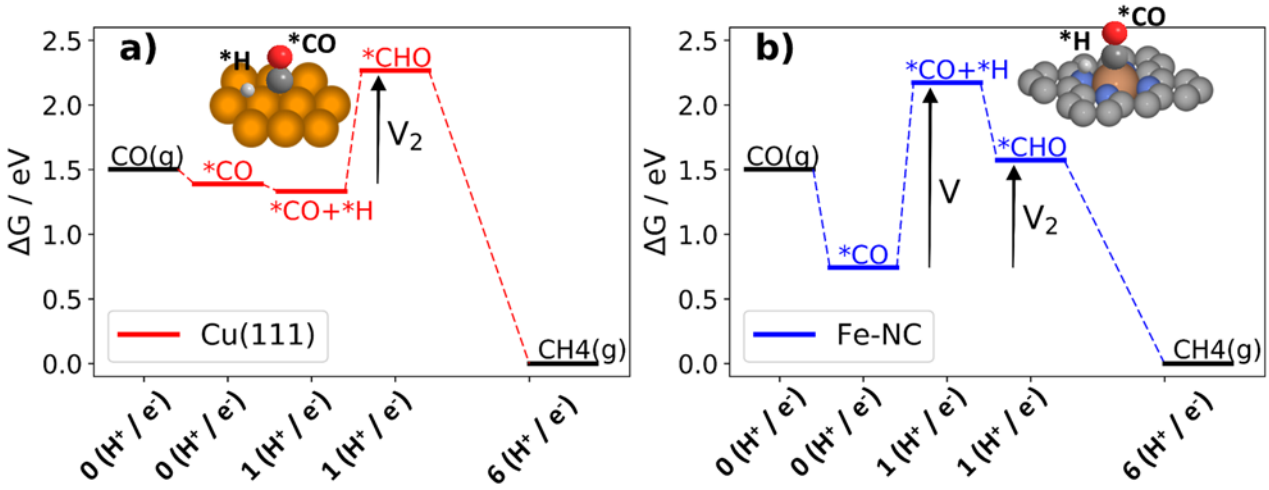

Figure 7- 5 The detailed protonation steps of *CO towards *CHO via the co-adsorption of *CO + *H on a) Cu (111) facet and on b) Fe-N-C, respectively.

In principle, the single site Fe-N-C catalyst constitutes an excellent catalytic CO producer, and thus could contribute sufficient reactive *CO intermediates for higher hydrocarbon yields. Unfortunately, indicated by our simulations, the isolated active site structure on the other hand causes a difficulty in *CO and *H co-adsorption, precluding a dominant formation of hydrocarbons. This finding suggests that the high-active CH_4(g) product formation may require an extended surface or a nearby proton source to lower the barrier of protonation. Strategies to circumvent this would be to increase the number of active sites and thus reducing their mutual distance, or else the introduction of suitable hydrogen adsorption / CO_x reactive twin sites may be a way toward enhanced hydrocarbon yields.

7.6 Discussion

The present combined experimental and theoretical mechanistic study has addressed the kinetics of the electroreduction of various small molecules that may constitute reactive intermediates on the way to methane, in particular CO_2, CO and CH_2O. The study aimed at i) identifying the role of these reducible reactants during the overall CO_2-towards-CH_4 pathway; ii) understanding the rate limiting factor of these key reactions; iii) reasoning the obstructed hydrocarbons selectivity of the Fe-N-C catalyst. As this knowledge will be crucial in the design of novel catalysts to reduce CO_2 into hydrocarbons.

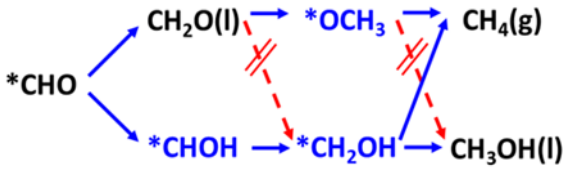

Figure 7- 6 Hypothesized paths of methanol and methane formation on single-site Fe-N-C catalyst.

To achieve the first two goals, unfortunately, neither our experiments nor computation deliver direct evidence to address the CH_2O reduction details. By tracking the methanol trace (see Figure 7-6), which is produced in terms of CO_2/CORR electrolysis (Figure S4-5) while denied in CH_2O reduction (Figure S4-7 and S4-8), we could speculate, methanol is more likely originated via a non-CH_2O channel, and the *CH_2OH is the key intermediate (*CO →*CHO →*CHOH →*CH_2OH →CH_3OH). Upon this hypothesis, the *CH_2OH – relevant for methanol formation – could be filtered out from the pure CH_2ORR, making methane as the only end-product (CH_2O →*OCH_3 →*O + CH_4, shown in Figure 7-6). This shows that the Fe-N-C catalyst provides different CH_2ORR paths than the metals,[15] and better understanding requires more systematical investigation upon a broader catalysts benchmark.

Based on the afore discussions, we could track the overall reaction paths of electrochemical CO_2 reduction into CH_4 with clearly addressing the contribution of CO_2, CO and CH_2O. Here, CO plays as the key intermediate towards methane, formaldehyde and methanol. Moreover, the produced CH_2O in this reaction network, could be further reduced and open up an extra reaction channel towards methane. On the contrary, methanol is more likely yielded from the non-CH_2O reaction channel, poses as a by-product aside the methane. More interestingly, our experimental studies have shown that some of the reduction steps involve proton-coupled electron transfers (PCET, namely, CO-to-CH_4) steps, whereas others, in particular such that involved rather weakly bounded species, featured proton-decoupled electron transfer (PDET, namely, CO_2-to-CO and CH_2O-to-CH_4) steps. This provided a broader and deeper understanding of the reaction mechanism and reaction network of the CO_2 reduction into a wide range of single-carbon chemical on the Fe-N-C single site catalysts. In this regard, an overall schematic display in Chapter 8, Scheme 8-2.

As to the third goal, our simulations revealed that the low hydrocarbons selectivity is primarily due to the isolated nature of the active site of the Fe-N_x motifs, which limits the rate with which further reduction and protonation of adsorbed *CO can occur. To overcome this drawback, synthesis approach to achieve catalysts

with novel site densities and site structure are needed. We speculate, that introducing dual twin metal sites, where two metal centers are located in atomic proximity, would mechanistically allow a more rapid protonation of CO, boosting the hydrocarbons formation on Fe-N-C catalysts.

Chapter 8. Summary and outlook

The M-N-C group catalysts have attracted increasing attention in recent years due to their remarkable CO_2RR performance, abundance and low-cost, making them promising candidates with great potential for future commercial applications. However, as early-stage research, concerns such as reaction / process mechanism, detailed understanding of nature-activity relationships need to be addressed in order to establish novel perspectives for evolving the effective CO_2RR catalysts and finding the efficient reaction conditions. This work presented novel and valuable approaches to overcome some of these challenges for M-N-C catalysts, which are summarized below (the corresponding structure is displayed in Scheme 8-1).

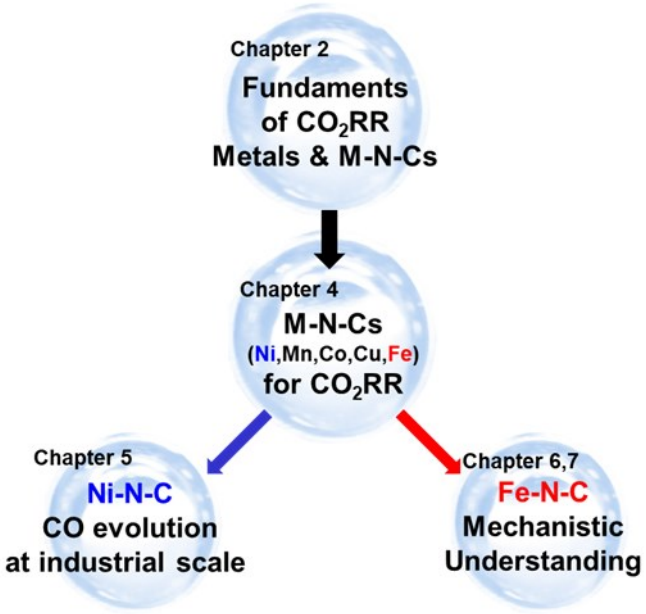

Scheme 8- 1 Summarized structure of this dissertation.

The mechanistic understanding of CO evolution over the M-N-C catalysts is addressed in chapter 4. Our synthesis provided 5 different M-N-C (M: Mn, Fe, Co, Ni, Cu) for the broader testing, and linked the experimental observation with DFT prediction. So we could suggest the nature of these porphyrin-like active motifs. In this contribution, the Ni-based one showed remarkable performance for CO evolution and the great potential for future industrial application. Explained by our theoretical simulation, the nature of the $Ni\text{-}N_x$ allowed to deny the unwanted HER and avoid the desorption issue due to weak interaction to H* and CO*, with the drawback of a large overpotential requirement due to weak binding to COOH*, the first key intermediate for CO_2RR into CO.

To reach the industrial level CO_2 electrolysis, performance exhibited in common liquid cell is far from sufficient. Little solubility of CO_2 is a common problem for CO_2RR in regular CO_2-saturated liquid electrolytes, causing mass transfer limitation of the CO_2 reactant. Thus, an engineering progress was done in a following-up work. In chapter 5, the gas diffusion electrode was deployed to overcome the CO_2 solubility issue. The GDE could create a special $CO_2(g)$ / $CO_2(Sol.)$ / Catalyst interface, boosting the CO_2 transfer for the

electrochemical reaction. Moreover, indicated by our DFT prediction, the Ni-N-C active site could intrinsically deny CO desorption problem in this operation, thus delivering the CO evolution partial current density over 200 mA cm^{-2}. However, the CO selectivity could not be maintained at higher working current densities. To overcome this limitation, strategies in catalysts synthesis and GDL-interface modification could be implemented. Towards catalysts synthesis, removable (soft) template such as the SiO_2 substrate could be introduced during the synthesis approach to physically increase the active site density of the catalyst. Moreover, tuning the active motifs (coordination number, doping of other elements) using specific methodologies could also be considered to achieve higher catalytic reactivities. Towards interface modification, the hydrophobicity, pore-size of the diffusion electrode, receipt of catalyst coating as well as the electrolyte pH value could play a significant role, which requires systematic research in the coming scenarios.

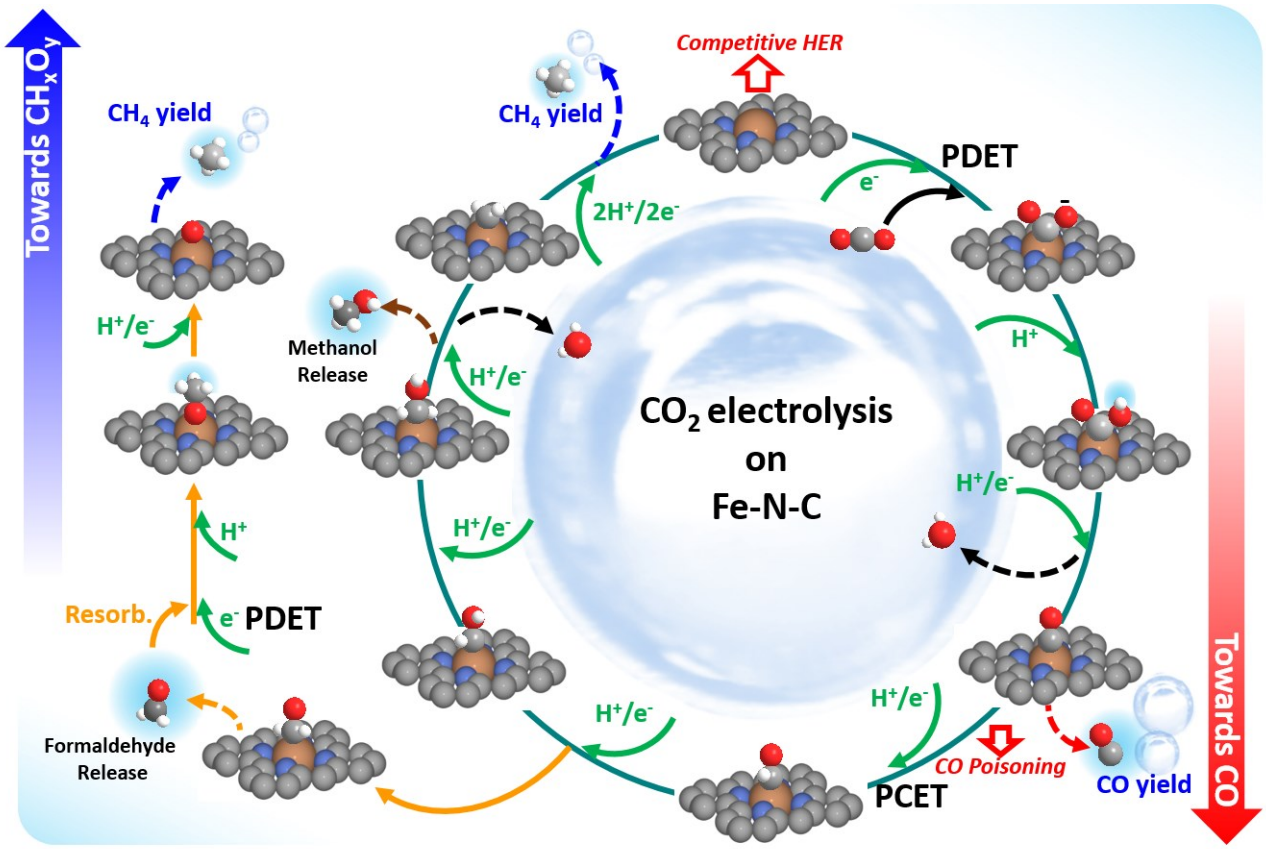

Scheme 8- 2 Overall reaction network form CO_2 reduction towards CH_4 via CO and CH_2O over the Fe-N-C catalyst. PCET: Proton Coupled Electron Transfer; PDET: Proton Decoupled Electron Transfer.

Unlike the Ni-based catalyst, the Fe- doped one suffers CO* poisoning problem at high potential / current range. On the positive site, the strong binding allows to operate the CO_2RR with less potential input, further, could produce hydrocarbons. In chapter 6, we perform the synthesis (PANI-based Fe-N-C) using a secondary nitrogen precursor and find melamine could help to introduce more Fe-N_x functionalities, improving the CO_2RR reactivity. Moreover, operando-XAS was employed to identify the Fe-N_x moieties in our operation potential range. An unusual Fe(I)-N_3 state was observed at high potential range (more negative than -0.9V_{RHE}), which could be responsible for methane formation.

In chapter 7, we provide the knowledge to draw an overall CO_2RR reaction network over the Fe-N-C catalyst, contributing the Scheme 8-2. The CO_2-to-CO and CH_2O-to-CH_4 happens via a proton decoupled electron transfer, whereas the proton is of great importance for CO further protonation. Our simulation points that the CO* and H* co-adsorption is blocked at the singe site single site Fe-N_x motifs, thus methane remains as a minor product. We suspect, novel M-N-C catalysts with specific bridging metal-metal-dimer active centers could boost the hydrocarbons production.

Reference

1 Cox, P. M., Betts, R. A., Jones, C. D., Spall, S. A. & Totterdell, I. J. Acceleration of global warming due to carbon-cycle feedbacks in a coupled climate model. *Nature* **408**, 184, doi:10.1038/35041539 (2000).

2 Hoegh-Guldberg, O. *et al.* Coral Reefs Under Rapid Climate Change and Ocean Acidification. *Science* **318**, 1737-1742, doi:10.1126/science.1152509 (2007).

3 Whipple, D. T. & Kenis, P. J. A. Prospects of CO2 Utilization via Direct Heterogeneous Electrochemical Reduction. *The Journal of Physical Chemistry Letters* **1**, 3451-3458, doi:10.1021/jz1012627 (2010).

4 Hori, Y. in *Modern Aspects of Electrochemistry* (eds Constantinos G. Vayenas, Ralph E. White, & Maria E. Gamboa-Aldeco) 89-189 (Springer New York, 2008).

5 Mistry, H. *et al.* Exceptional Size-Dependent Activity Enhancement in the Electroreduction of CO2 over Au Nanoparticles. *Journal of the American Chemical Society* **136**, 16473-16476, doi:10.1021/ja508879j (2014).

6 Lu, Q. *et al.* A selective and efficient electrocatalyst for carbon dioxide reduction. *Nature Communications* **5**, 3242, doi:10.1038/ncomms4242

https://www.nature.com/articles/ncomms4242#supplementary-information (2014).

7 Kim, C. *et al.* Achieving Selective and Efficient Electrocatalytic Activity for CO2 Reduction Using Immobilized Silver Nanoparticles. *Journal of the American Chemical Society* **137**, 13844-13850, doi:10.1021/jacs.5b06568 (2015).

8 Kim, C. *et al.* Insight into Electrochemical CO2 Reduction on Surface-Molecule-Mediated Ag Nanoparticles. *ACS Catalysis* **7**, 779-785, doi:10.1021/acscatal.6b01862 (2017).

9 Rosen, J. *et al.* Mechanistic Insights into the Electrochemical Reduction of CO2 to CO on Nanostructured Ag Surfaces. *ACS Catalysis* **5**, 4293-4299, doi:10.1021/acscatal.5b00840 (2015).

10 Wenlei Zhu, R. M., Önder Metin, Haifeng Lv, Shaojun Guo, Christopher J. Wright, Xiaolian Sun, Andrew A. Peterson, Shouheng Sun. Monodisperse Au Nanoparticles for Selective Electrocatalytic Reduction of CO2 to CO. *J. Am. Chem. Soc* **135**, 16833−16836 (2013).

11 Wenlei Zhu, Y.-J. Z., Hongyi Zhang, Haifeng Lv, Qing Li, Ronald Michalsky, Andrew A. Peterson, Shouheng Sun. Active and Selective Conversion of CO2 to CO on Ultrathin Au Nanowires. *J. Am. Chem. Soc* **136**, 16132−16135 (2014).

12 Hori, Y., Murata, A. & Takahashi, R. Formation of hydrocarbons in the electrochemical reduction of carbon dioxide at a copper electrode in aqueous solution. *Journal of the Chemical Society, Faraday Transactions 1: Physical Chemistry in Condensed Phases* **85**, 2309-2326, doi:10.1039/F19898502309 (1989).

13 Peterson, A. A., Abild-Pedersen, F., Studt, F., Rossmeisl, J. & Norskov, J. K. How copper catalyzes the electroreduction of carbon dioxide into hydrocarbon fuels. *Energy & Environmental Science* **3**, 1311-1315, doi:10.1039/C0EE00071J (2010).

14 Kuhl, K. P., Cave, E. R., Abram, D. N. & Jaramillo, T. F. New insights into the electrochemical reduction of carbon dioxide on metallic copper surfaces. *Energy & Environmental Science* **5**, 7050-7059, doi:10.1039/C2EE21234J (2012).

15 Bagger, A., Ju, W., Varela Ana, S., Strasser, P. & Rossmeisl, J. Electrochemical CO2 Reduction: A Classification Problem. *ChemPhysChem* **18**, 3266-3273, doi:10.1002/cphc.201700736 (2017).

16 Wang, L. *et al.* Electrochemical Carbon Monoxide Reduction on Polycrystalline Copper: Effects of Potential, Pressure, and pH on Selectivity toward Multicarbon and Oxygenated Products. *ACS Catalysis*, 7445-7454, doi:10.1021/acscatal.8b01200 (2018).

17 Hori, Y., Takahashi, R., Yoshinami, Y. & Murata, A. Electrochemical Reduction of CO at a Copper Electrode. *The Journal of Physical Chemistry B* **101**, 7075-7081, doi:10.1021/jp970284i (1997).
18 Murata, A. & Hori, Y. Product Selectivity Affected by Cationic Species in Electrochemical Reduction of CO2 and CO at a Cu Electrode. *Bulletin of the Chemical Society of Japan* **64**, 123-127, doi:10.1246/bcsj.64.123 (1991).
19 Schouten, K. J. P., Pérez Gallent, E. & Koper, M. T. M. The influence of pH on the reduction of CO and CO2 to hydrocarbons on copper electrodes. *Journal of Electroanalytical Chemistry* **716**, 53-57, doi:https://doi.org/10.1016/j.jelechem.2013.08.033 (2014).
20 Mistry, H. *et al.* Highly selective plasma-activated copper catalysts for carbon dioxide reduction to ethylene. *Nature Communications* **7**, 12123, doi:10.1038/ncomms12123

https://www.nature.com/articles/ncomms12123#supplementary-information (2016).
21 Gao, D., Scholten, F. & Roldan Cuenya, B. Improved CO2 Electroreduction Performance on Plasma-Activated Cu Catalysts via Electrolyte Design: Halide Effect. *ACS Catalysis* **7**, 5112-5120, doi:10.1021/acscatal.7b01416 (2017).
22 Tang, W. *et al.* The importance of surface morphology in controlling the selectivity of polycrystalline copper for CO2 electroreduction. *Physical Chemistry Chemical Physics* **14**, 76-81, doi:10.1039/C1CP22700A (2012).
23 Li, C. W., Ciston, J. & Kanan, M. W. Electroreduction of carbon monoxide to liquid fuel on oxide-derived nanocrystalline copper. *Nature* **508**, 504, doi:10.1038/nature13249 (2014).
24 Dinh, C.-T. *et al.* CO₂ electroreduction to ethylene via hydroxide-mediated copper catalysis at an abrupt interface. *Science* **360**, 783-787, doi:10.1126/science.aas9100 (2018).
25 Wang, X., Varela, A. S., Bergmann, A., Kühl, S. & Strasser, P. Catalyst Particle Density Controls Hydrocarbon Product Selectivity in CO2 Electroreduction on CuOx. *ChemSusChem* **10**, 4642-4649, doi:doi:10.1002/cssc.201701179 (2017).
26 Wannakao, S., Jumpathong, W. & Kongpatpanich, K. Tailoring Metalloporphyrin Frameworks for an Efficient Carbon Dioxide Electroreduction: Selectively Stabilizing Key Intermediates with H-Bonding Pockets. *Inorganic Chemistry* **56**, 7200-7209, doi:10.1021/acs.inorgchem.7b00839 (2017).
27 Tripkovic, V. *et al.* Electrochemical CO2 and CO Reduction on Metal-Functionalized Porphyrin-like Graphene. *The Journal of Physical Chemistry C* **117**, 9187-9195, doi:10.1021/jp306172k (2013).
28 Fisher, B. J. & Eisenberg, R. Electrocatalytic reduction of carbon dioxide by using macrocycles of nickel and cobalt. *Journal of the American Chemical Society* **102**, 7361-7363, doi:10.1021/ja00544a035 (1980).
29 Beley, M., Collin, J.-P., Ruppert, R. & Sauvage, J.-P. Nickel(II)-cyclam: an extremely selective electrocatalyst for reduction of CO2 in water. *Journal of the Chemical Society, Chemical Communications*, 1315-1316, doi:10.1039/C39840001315 (1984).
30 Hawecker, J., Lehn, J.-M. & Ziessel, R. Electrocatalytic reduction of carbon dioxide mediated by Re(bipy)(CO)3Cl (bipy = 2,2′-bipyridine). *Journal of the Chemical Society, Chemical Communications*, 328-330, doi:10.1039/C39840000328 (1984).
31 Reuillard, B. *et al.* Tuning Product Selectivity for Aqueous CO2 Reduction with a Mn(bipyridine)-pyrene Catalyst Immobilized on a Carbon Nanotube Electrode. *Journal of the American Chemical Society* **139**, 14425-14435, doi:10.1021/jacs.7b06269 (2017).
32 Behar, D. *et al.* Cobalt Porphyrin Catalyzed Reduction of CO2. Radiation Chemical, Photochemical, and Electrochemical Studies. *The Journal of Physical Chemistry A* **102**, 2870-2877, doi:10.1021/jp9807017 (1998).

33 Shen, J. *et al.* Electrocatalytic reduction of carbon dioxide to carbon monoxide and methane at an immobilized cobalt protoporphyrin. *Nature Communications* **6**, 8177, doi:10.1038/ncomms9177

http://www.nature.com/articles/ncomms9177#supplementary-information (2015).

34 Birdja, Y. Y., Shen, J. & Koper, M. T. M. Influence of the metal center of metalloprotoporphyrins on the electrocatalytic CO2 reduction to formic acid. *Catalysis Today* **288**, 37-47, doi:https://doi.org/10.1016/j.cattod.2017.02.046 (2017).

35 Costentin, C., Drouet, S., Robert, M. & Savéant, J.-M. A Local Proton Source Enhances CO₂ Electroreduction to CO by a Molecular Fe Catalyst. *Science* **338**, 90-94, doi:10.1126/science.1224581 (2012).

36 Varela, A. S., Ju, W. & Strasser, P. Molecular Nitrogen–Carbon Catalysts, Solid Metal Organic Framework Catalysts, and Solid Metal/Nitrogen-Doped Carbon (MNC) Catalysts for the Electrochemical CO2 Reduction. *Advanced Energy Materials* **8**, 1703614, doi:doi:10.1002/aenm.201703614 (2018).

37 Wu, G., More, K. L., Johnston, C. M. & Zelenay, P. High-Performance Electrocatalysts for Oxygen Reduction Derived from Polyaniline, Iron, and Cobalt. *Science* **332**, 443-447, doi:10.1126/science.1200832 (2011).

38 Kramm, U. I. *et al.* Structure of the catalytic sites in Fe/N/C-catalysts for O2-reduction in PEM fuel cells. *Physical Chemistry Chemical Physics* **14**, 11673-11688, doi:10.1039/C2CP41957B (2012).

39 Ranjbar Sahraie, N., Paraknowitsch, J. P., Göbel, C., Thomas, A. & Strasser, P. Noble-Metal-Free Electrocatalysts with Enhanced ORR Performance by Task-Specific Functionalization of Carbon using Ionic Liquid Precursor Systems. *Journal of the American Chemical Society* **136**, 14486-14497, doi:10.1021/ja506553r (2014).

40 Sahraie, N. R. *et al.* Quantifying the density and utilization of active sites in non-precious metal oxygen electroreduction catalysts. *Nature Communications* **6**, 8618, doi:10.1038/ncomms9618

https://www.nature.com/articles/ncomms9618#supplementary-information (2015).

41 Leonard, N. D. *et al.* Deconvolution of Utilization, Site Density, and Turnover Frequency of Fe–Nitrogen–Carbon Oxygen Reduction Reaction Catalysts Prepared with Secondary N-Precursors. *ACS Catalysis* **8**, 1640-1647, doi:10.1021/acscatal.7b02897 (2018).

42 Zitolo, A. *et al.* Identification of catalytic sites for oxygen reduction in iron- and nitrogen-doped graphene materials. *Nature Materials* **14**, 937-+, doi:10.1038/Nmat4367 (2015).

43 Varela, A. S. *et al.* Metal-Doped Nitrogenated Carbon as an Efficient Catalyst for Direct CO2 Electroreduction to CO and Hydrocarbons. *Angew Chem Int Edit* **54**, 10758-10762, doi:10.1002/anie.201502099 (2015).

44 Li, X. *et al.* Exclusive Ni–N4 Sites Realize Near-Unity CO Selectivity for Electrochemical CO2 Reduction. *Journal of the American Chemical Society* **139**, 14889-14892, doi:10.1021/jacs.7b09074 (2017).

45 Wu, J. *et al.* Achieving Highly Efficient, Selective, and Stable CO2 Reduction on Nitrogen-Doped Carbon Nanotubes. *ACS Nano* **9**, 5364-5371, doi:10.1021/acsnano.5b01079 (2015).

46 Wu, J. *et al.* A metal-free electrocatalyst for carbon dioxide reduction to multi-carbon hydrocarbons and oxygenates. **7**, 13869, doi:10.1038/ncomms13869

https://www.nature.com/articles/ncomms13869#supplementary-information (2016).

47 Leonard, N. *et al.* The chemical identity, state and structure of catalytically active centers during the electrochemical CO2 reduction on porous Fe-nitrogen-carbon (Fe-N-C) materials. *Chemical Science* **9**, 5064-5073, doi:10.1039/C8SC00491A (2018).

48 Zitolo, A. *et al.* Identification of catalytic sites in cobalt-nitrogen-carbon materials for the oxygen reduction reaction. *Nature Communications* **8**, 957, doi:10.1038/s41467-017-01100-7 (2017).

49 Artyushkova, K., Serov, A., Rojas-Carbonell, S. & Atanassov, P. Chemistry of Multitudinous Active Sites for Oxygen Reduction Reaction in Transition Metal–Nitrogen–Carbon Electrocatalysts. *The Journal of Physical Chemistry C* **119**, 25917-25928, doi:10.1021/acs.jpcc.5b07653 (2015).

50 Kabir, S., Artyushkova, K., Kiefer, B. & Atanassov, P. Computational and experimental evidence for a new TM-N3/C moiety family in non-PGM electrocatalysts. *Physical Chemistry Chemical Physics* **17**, 17785-17789, doi:10.1039/C5CP02230D (2015).

51 Ju, W. *et al.* Understanding activity and selectivity of metal-nitrogen-doped carbon catalysts for electrochemical reduction of CO2. *Nature Communications* **8**, 944, doi:10.1038/s41467-017-01035-z (2017).

52 Jiang, K. *et al.* Isolated Ni single atoms in graphene nanosheets for high-performance CO2 reduction. *Energy & Environmental Science* **11**, 893-903, doi:10.1039/C7EE03245E (2018).

53 Yang, F. *et al.* Highly Efficient CO2 Electroreduction on ZnN4-based Single-Atom Catalyst. *Angewandte Chemie* **130**, 12483-12487, doi:doi:10.1002/ange.201805871 (2018).

54 Chen, Z., Mou, K., Yao, S. & Liu, L. Zinc-Coordinated Nitrogen-Codoped Graphene as an Efficient Catalyst for Selective Electrochemical Reduction of CO2 to CO. *ChemSusChem* **11**, 2944-2952, doi:doi:10.1002/cssc.201800925 (2018).

55 Roy, A. *et al.* Nanostructured metal-N-C electrocatalysts for CO2 reduction and hydrogen evolution reactions. *Applied Catalysis B: Environmental* **232**, 512-520, doi:https://doi.org/10.1016/j.apcatb.2018.03.093 (2018).

56 Su, P., Iwase, K., Harada, T., Kamiya, K. & Nakanishi, S. Covalent triazine framework modified with coordinatively-unsaturated Co or Ni atoms for CO2 electrochemical reduction. *Chemical Science* **9**, 3941-3947, doi:10.1039/C8SC00604K (2018).

57 Dembinska, B., Kiciński, W., Januszewska, A., Dobrzeniecka, A. & Kulesza, P. J. Carbon Dioxide Electroreduction at Highly Porous Nitrogen and Sulfur Co-Doped Iron-Containing Heterogeneous Carbon Gel. *Journal of The Electrochemical Society* **164**, H484-H490, doi:10.1149/2.0721707jes (2017).

58 Möller, T. *et al.* Efficient CO2 to CO electrolysis on solid Ni–N–C catalysts at industrial current densities. *Energy & Environmental Science*, doi:10.1039/C8EE02662A (2019).

59 Zhang, Z. *et al.* Reaction Mechanisms of Well-Defined Metal–N4 Sites in Electrocatalytic CO2 Reduction. *Angewandte Chemie International Edition* **57**, 16339-16342, doi:doi:10.1002/anie.201808593 (2018).

60 Jiang, K. *et al.* Transition-Metal Single Atoms in a Graphene Shell as Active Centers for Highly Efficient Artificial Photosynthesis. *Chem*, doi:https://doi.org/10.1016/j.chempr.2017.09.014 (2017).

61 Yan, C. *et al.* Coordinatively unsaturated nickel–nitrogen sites towards selective and high-rate CO2 electroreduction. *Energy & Environmental Science* **11**, 1204-1210, doi:10.1039/C8EE00133B (2018).

62 Ravel, B. & Newville, M. ATHENA, ARTEMIS, HEPHAESTUS: data analysis for X-ray absorption spectroscopy using IFEFFIT. *J Synchrotron Radiat* **12**, 537-541, doi:10.1107/S0909049505012719 (2005).

63 Ankudinov, A. L., Ravel, B., Rehr, J. J. & Conradson, S. D. Real-space multiple-scattering calculation and interpretation of x-ray-absorption near-edge structure. *Phys Rev B* **58**, 7565-7576, doi:DOI 10.1103/PhysRevB.58.7565 (1998).

64 Ask Hjorth, L. *et al.* The atomic simulation environment—a Python library for working with atoms. *Journal of Physics: Condensed Matter* **29**, 273002 (2017).

65 Enkovaara, J. *et al.* Electronic structure calculations with GPAW: a real-space implementation of the projector augmented-wave method. *Journal of Physics: Condensed Matter* **22**, 253202 (2010).

66 Hammer, B., Hansen, L. B. & Nørskov, J. K. Improved adsorption energetics within density-functional theory using revised Perdew-Burke-Ernzerhof functionals. *Phys Rev B* **59**, 7413-7421, doi:10.1103/PhysRevB.59.7413 (1999).

67 Nørskov, J. K. *et al.* Origin of the Overpotential for Oxygen Reduction at a Fuel-Cell Cathode. *The Journal of Physical Chemistry B* **108**, 17886-17892, doi:10.1021/jp047349j (2004).

68 Chan, K., Tsai, C., Hansen Heine, A. & Nørskov Jens, K. Molybdenum Sulfides and Selenides as Possible Electrocatalysts for CO2 Reduction. *ChemCatChem* **6**, 1899-1905, doi:10.1002/cctc.201402128 (2014).

69 Guang-Ping Hao, W.-C. L., Dan Qian, Guang-Hui Wang, Wei-Ping Zhang, Tao Zhang, Ai-Qin Wang, Ferdi Schüth, Hans-Josef Bongard, An-Hui Lu. Structurally Designed Synthesis of Mechanically Stable Poly(benzoxazine-co-resol)-Based Porous Carbon Monoliths and Their Application as High-Performance CO2 Capture Sorbents. *J. Am. Chem. Soc* **133**, 11378–11388 (2011).

70 C.D. Wagner, A. V. N., A. Kraut-Vass, J.W. Allison, C.J. Powell, J.R. Jr. Rumble. NIST Standard Reference Database 20. (2003).

71 M.C. Biesinger, B. P. P., L.W.M. Lau, A.R. Gerson, R.St.C. Smart. Resolving surface chemical states in XPS analysis of first row transition metals, oxides and hydroxides: Cr, Mn, Fe, Co and Ni. *Appplied Surface Science* **257**, 887-898 (2010).

72 S. Muralidharan, R. G. H. Satellite in the x-ray photoelectron spectra of metalloporphyrins. *Journal of Chemical Physics* **71**, 2970-2974 (1979).

73 H.W. Nesbitt, D. B. Interpretation of XPS Mn(2p) spectra of Mn oxyhydroxides and constraints on the mechanism of MnO2 precipitation. *American Mineralogist* **83**, 305-315 (1998).

74 Bai, Y. Photoelectron Spectroscopic Investigations of Porphyrins and Phthalocyanines on Ag(111) and Au(111): Adsorption and Reactivity. (2010).

75 Li, Y., Su, H., Chan, S. H. & Sun, Q. CO2 Electroreduction Performance of Transition Metal Dimers Supported on Graphene: A Theoretical Study. *ACS Catalysis* **5**, 6658-6664, doi:10.1021/acscatal.5b01165 (2015).

76 Back, S., Lim, J., Kim, N.-Y., Kim, Y.-H. & Jung, Y. Single-atom catalysts for CO2 electroreduction with significant activity and selectivity improvements. *Chemical Science* **8**, 1090-1096, doi:10.1039/C6SC03911A (2017).

77 Shen, H., Li, Y. & Sun, Q. CO2 Electroreduction Performance of Phthalocyanine Sheet with Mn Dimer: A Theoretical Study. *The Journal of Physical Chemistry C* **121**, 3963-3969, doi:10.1021/acs.jpcc.7b00317 (2017).

78 Michael Busch, N. B. H., Ulrike I. Kramm, Samira Siahrostami, Petr Krtil, Jan Rossmeisl. Beyond the top of the volcano? – A unified approach to electrocatalytic oxygen reduction and oxygen evolution. *Nano Energy*, 2211-2855 (2016).

79 Atchudan, R., Joo, J. & Pandurangan, A. An efficient synthesis of graphenated carbon nanotubes over the tailored mesoporous molecular sieves by chemical vapor deposition. *Materials Research Bulletin* **48**, 2205-2212, doi:https://doi.org/10.1016/j.materresbull.2013.02.048 (2013).

80 Wang, Z. *et al.* Nanocarbons from rice husk by microwave plasma irradiation: From graphene and carbon nanotubes to graphenated carbon nanotube hybrids. *Carbon* **94**, 479-484, doi:https://doi.org/10.1016/j.carbon.2015.07.037 (2015).

81 Artyushkova, K. *et al.* Density functional theory calculations of XPS binding energy shift for nitrogen-containing graphene-like structures. *Chem Commun* **49**, 2539-2541, doi:10.1039/c3cc40324f (2013).

82 Gupta, N., Gattrell, M. & MacDougall, B. Calculation for the cathode surface concentrations in the electrochemical reduction of CO2 in KHCO3 solutions. *Journal of Applied Electrochemistry* **36**, 161-172, doi:10.1007/s10800-005-9058-y (2006).

83 Haas, T., Krause, R., Weber, R., Demler, M. & Schmid, G. Technical photosynthesis involving CO2 electrolysis and fermentation. *Nature Catalysis* **1**, 32-39, doi:10.1038/s41929-017-0005-1 (2018).

84 Verma, S., Lu, X., Ma, S., Masel, R. I. & Kenis, P. J. The effect of electrolyte composition on the electroreduction of CO2 to CO on Ag based gas diffusion electrodes. *Phys Chem Chem Phys* **18**, 7075-7084, doi:10.1039/c5cp05665a (2016).

85 Dinh, C.-T., García de Arquer, F. P., Sinton, D. & Sargent, E. H. High Rate, Selective, and Stable Electroreduction of CO2 to CO in Basic and Neutral Media. *ACS Energy Letters*, 2835-2840, doi:10.1021/acsenergylett.8b01734 (2018).

86 Nallathambi, V., Leonard, N., Kothandaraman, R. & Barton, S. C. Nitrogen Precursor Effects in Iron-Nitrogen-Carbon Oxygen Reduction Catalysts. *Electrochem Solid St* **14**, B55-B58, doi:10.1149/1.3566065 (2011).

87 Leonard, N., Nallathambi, V. & Barton, S. C. Carbon Supports for Non-Precious Metal Oxygen Reducing Catalysts. *Journal of The Electrochemical Society* **160**, F788-F792, doi:10.1149/2.026308jes (2013).

88 Leonard, N. D. & Barton, S. C. Analysis of Adsorption Effects on a Metal-Nitrogen-Carbon Catalyst Using a Rotating Ring-Disk Study. *Journal of the Electrochemical Society* **161**, H3100-H3105, doi:10.1149/2.0161413jes (2014).

89 Chung, H. T. *et al.* Combining Nitrogen Precursors in Synthesis of Non-Precious Metal ORR Catalysts with Improved Fuel Cell Performance. *Meeting Abstracts* **MA2015-02**, 1278 (2015).

90 Chung, H. T. *et al.* Cyanamide-derived non-precious metal catalyst for oxygen reduction. *Electrochem Commun* **12**, 1792-1795 (2010).

91 Chung, H. T., Won, J. H. & Zelenay, P. Active and stable carbon nanotube/nanoparticle composite electrocatalyst for oxygen reduction. *Nat Commun* **4**, 1922, doi:10.1038/ncomms2944 (2013).

92 Tian, J., Birry, L., Jaouen, F. & Dodelet, J. P. Fe-based catalysts for oxygen reduction in proton exchange membrane fuel cells with cyanamide as nitrogen precursor and/or pore-filler. *Electrochim Acta* **56**, 3276-3285, doi:10.1016/j.electacta.2011.01.029 (2011).

93 Workman, M. J. *et al.* Platinum group metal-free electrocatalysts: Effects of synthesis on structure and performance in proton-exchange membrane fuel cell cathodes. *J Power Sources* **348**, 30-39, doi:10.1016/j.jpowsour.2017.02.067 (2017).

94 Beamson, G. & Briggs, D. High-Resolution Monochromated X-Ray Photoelectron-Spectroscopy of Organic Polymers - a Comparison between Solid-State Data for Organic Polymers and Gas-Phase Data for Small Molecules. *Mol Phys* **76**, 919-936, doi:Doi 10.1080/00268979200101761 (1992).

95 Lindberg, B. J. *et al.* Molecular Spectroscopy by Means of ESCA II. Sulfur compounds. Correlation of electron binding energy with structure. *Physica Scripta* **1**, 286 (1970).

96 Smart, R. S. C., Skinner, W. M. & Gerson, A. R. XPS of sulphide mineral surfaces: metal-deficient, polysulphides, defects and elemental sulphur. *Surface and Interface Analysis* **28**, 101-105, doi:10.1002/(SICI)1096-9918(199908)28:1<101::AID-SIA627>3.0.CO;2-0 (1999).

97 Yamashita, T. & Hayes, P. Analysis of XPS spectra of Fe2+ and Fe3+ ions in oxide materials. *Appl Surf Sci* **254**, 2441-2449, doi:10.1016/j.apsusc.2007.09.063 (2008).

98 Grosvenor, A. P., Kobe, B. A., Biesinger, M. C. & McIntyre, N. S. Investigation of multiplet splitting of Fe 2p XPS spectra and bonding in iron compounds. *Surface and Interface Analysis* **36**, 1564-1574, doi:10.1002/sia.1984 (2004).

99 Tanuma, S., Powell, C. J. & Penn, D. R. Calculations of Electron Inelastic Mean Free Paths for 31 Materials. *Surface and Interface Analysis* **11**, 577-589, doi:DOI 10.1002/sia.740111107 (1988).
100 Li, J. K. *et al.* Structural and mechanistic basis for the high activity of Fe-N-C catalysts toward oxygen reduction. *Energy & Environmental Science* **9**, 2418-2432, doi:10.1039/c6ee01160h (2016).
101 Hu, C. J., Noll, B. C., Schulz, C. E. & Scheidt, W. R. Four-coordinate iron(II) porphyrinates: Electronic configuration change by intermolecular interaction. *Inorganic Chemistry* **46**, 619-621, doi:10.1021/ic0620182 (2007).
102 Varnell, J. A. *et al.* Identification of carbon-encapsulated iron nanoparticles as active species in non-precious metal oxygen reduction catalysts. *Nature Communications* **7**, 12582, doi:10.1038/ncomms12582

http://www.nature.com/articles/ncomms12582#supplementary-information (2016).
103 Bagger, A., Ju, W., Varela, A. S., Strasser, P. & Rossmeisl, J. Single site porphyrine-like structures advantages over metals for selective electrochemical CO2 reduction. *Catalysis Today*, doi:http://doi.org/10.1016/j.cattod.2017.02.028 (2017).
104 Jia, Q. *et al.* Experimental Observation of Redox-Induced Fe-N Switching Behavior as a Determinant Role for Oxygen Reduction Activity. *Acs Nano* **9**, 12496-12505, doi:10.1021/acsnano.5b05984 (2015).
105 Costentin, C., Robert, M., Saveant, J. M. & Tatin, A. Efficient and selective molecular catalyst for the CO2-to-CO electrochemical conversion in water. *P Natl Acad Sci USA* **112**, 6882-6886, doi:10.1073/pnas.1507063112 (2015).
106 Azcarate, I., Costentin, C., Robert, M. & Saveant, J. M. Through-Space Charge Interaction Substituent Effects in Molecular Catalysis Leading to the Design of the Most Efficient Catalyst of CO2-to-CO Electrochemical Conversion. *Journal of the American Chemical Society* **138**, 16639-16644, doi:10.1021/jacs.6b07014 (2016).
107 Rao, H., Schmidt, L. C., Bonin, J. & Robert, M. Visible-light-driven methane formation from CO2 with a molecular iron catalyst. *Nature* **548**, 74-77, doi:10.1038/nature23016 (2017).
108 Bhugun, I., Lexa, D. & Saveant, J. M. Homogeneous catalysis of electrochemical hydrogen evolution by iron(0) porphyrins. *Journal of the American Chemical Society* **118**, 3982-3983, doi:DOI 10.1021/ja954326x (1996).
109 Ju, W. *et al.* Unraveling Mechanistic Reaction Pathways of the Electrochemical CO2 Reduction on Fe-N-C Single Site Catalysts. *ACS Energy Letters*, doi:10.1021/acsenergylett.9b01049 (2019).
110 Bertheussen, E. *et al.* Acetaldehyde as an Intermediate in the Electroreduction of Carbon Monoxide to Ethanol on Oxide-Derived Copper. *Angewandte Chemie International Edition* **55**, 1450-1454, doi:10.1002/anie.201508851 (2015).
111 Ledezma-Yanez, I., Gallent, E. P., Koper, M. T. M. & Calle-Vallejo, F. Structure-sensitive electroreduction of acetaldehyde to ethanol on copper and its mechanistic implications for CO and CO2 reduction. *Catalysis Today* **262**, 90-94, doi:https://doi.org/10.1016/j.cattod.2015.09.029 (2016).
112 Nie, X., Esopi, M. R., Janik, M. J. & Asthagiri, A. Selectivity of CO2 Reduction on Copper Electrodes: The Role of the Kinetics of Elementary Steps. *Angewandte Chemie International Edition* **52**, 2459-2462, doi:10.1002/anie.201208320 (2013).
113 Hussain, J., Jónsson, H. & Skúlason, E. Calculations of Product Selectivity in Electrochemical CO2 Reduction. *ACS Catalysis* **8**, 5240-5249, doi:10.1021/acscatal.7b03308 (2018).
114 Bagger, A., Arnarson, L., Hansen, M. H., Spohr, E. & Rossmeisl, J. Electrochemical CO Reduction: A Property of the Electrochemical Interface. *Journal of the American Chemical Society* **141**, 1506-1514, doi:10.1021/jacs.8b08839 (2019).

115 Calle-Vallejo, F., Krabbe, A. & García-Lastra, J. M. How covalence breaks adsorption-energy scaling relations and solvation restores them. *Chemical Science* **8**, 124-130, doi:10.1039/C6SC02123A (2017).

116 Varela, A. S. *et al.* pH Effects on the Selectivity of the Electrocatalytic CO2 Reduction on Graphene-Embedded Fe–N–C Motifs: Bridging Concepts between Molecular Homogeneous and Solid-State Heterogeneous Catalysis. *ACS Energy Letters* **3**, 812-817, doi:10.1021/acsenergylett.8b00273 (2018).

117 Koper, M. T. M. Theory of the transition from sequential to concerted electrochemical proton–electron transfer. *Physical Chemistry Chemical Physics* **15**, 1399-1407, doi:10.1039/C2CP42369C (2013).

118 Göttle, A. J. & Koper, M. T. M. Proton-coupled electron transfer in the electrocatalysis of CO2 reduction: prediction of sequential vs. concerted pathways using DFT. *Chemical Science* **8**, 458-465, doi:10.1039/C6SC02984A (2017).

119 Hori, Y., Takahashi, I., Koga, O. & Hoshi, N. Electrochemical reduction of carbon dioxide at various series of copper single crystal electrodes. *Journal of Molecular Catalysis A: Chemical* **199**, 39-47, doi:https://doi.org/10.1016/S1381-1169(03)00016-5 (2003).

120 Schreier, M., Yoon, Y., Jackson, M. N. & Surendranath, Y. Competition between H and CO for Active Sites Governs Copper-Mediated Electrosynthesis of Hydrocarbon Fuels. *Angewandte Chemie International Edition* **57**, 10221-10225, doi:doi:10.1002/anie.201806051 (2018).

121 Skála, R., Císařová, I. & Drábek, M. in *American Mineralogist* Vol. 91 917 (2006).

Appendix

A1. Supplementary Information to Chapter 4

Table S1- 1 Physical parameters of nitrogen-metal doped carbon (M-N-C) CO_2RR electrocatalysts

ID	S_{BET} [a] m^2g^{-1}	DL-Cap [b] mF cm^{-2}	Overall metal by ICP wt. %	
			Metal [c]	Cu [d]
Mn-N-C	938	87.82	Mn: 0.44	0.16
Fe-N-C	724	66.94	Ni: 2.88	0.12
Co-N-C	758	80.39	Co: 1.11	0.17
Ni-N-C	615	38.82	Fe: 1.73	0.14
Cu-N-C	807	74.38	-	1.11

a) S_{BET}: N_2 ad/desorption-based surface area; b) Double layer capacity values (Geometric area of each electrode is 1 cm^2 with 0.76 mg cm^{-2} catalyst loading); c,d) overall metal content determined from ICP-OES measurement. Notably, the detection limit of ICP-OES is as low as 0.1, 0.25, 0.4, 0.5 and 0.1 µg/L for Fe, Co, Cu, Ni and Mn, respectively, where the measured solution of the dissolved M-N-C sample is 5000, 1400, 900, 1700 and 1300 times higher than the limit, indicating a low uncertainty. Each sample is measured twice. The value in the table is the average.

Scanning Electron Microscopy

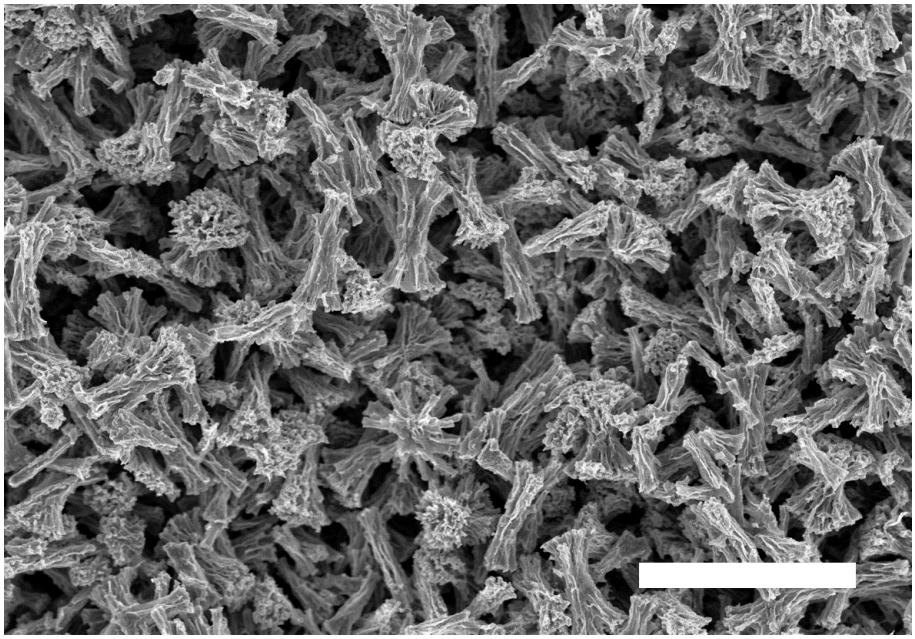

Figure S1- 1 Typical SEM image of the M-N-C electrocatalysts. Scale bar: 10 μm.

N_2 physisorption

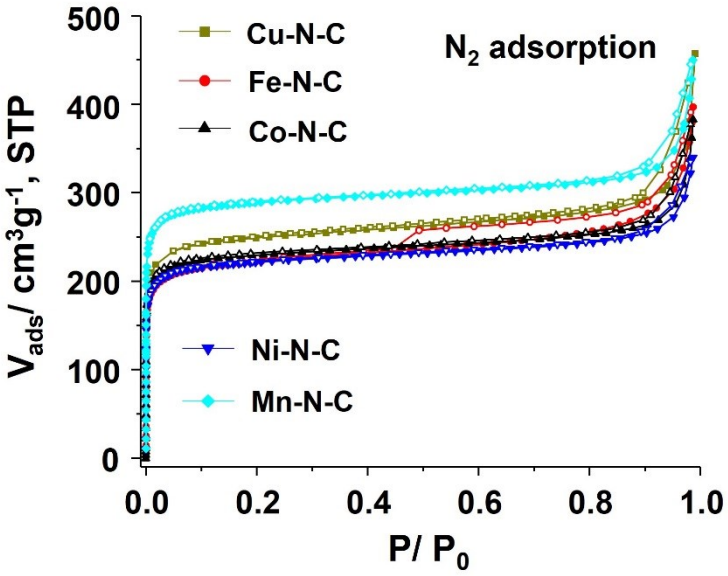

Figure S1- 2 N_2 physisorption isotherms for this family of M-N-C electrocatalysts. As shown, the isotherms are type I indicating the microporous structures; the abrupt increase in the higher pressure regime indicating the existence of macropores. In short, this information confirms the rich of microporosity, and indicates the hierarchical structure.

Double Layer Capacity Measurements – Relation to BET surface area

Cycle voltammetry was performed between 0.0 and 0.52 V vs. RHE to avoid the interference of the faradaic process. Double layer current density was utilized to determine double layer capacity, which is proportional to the double-layer interfacial area.

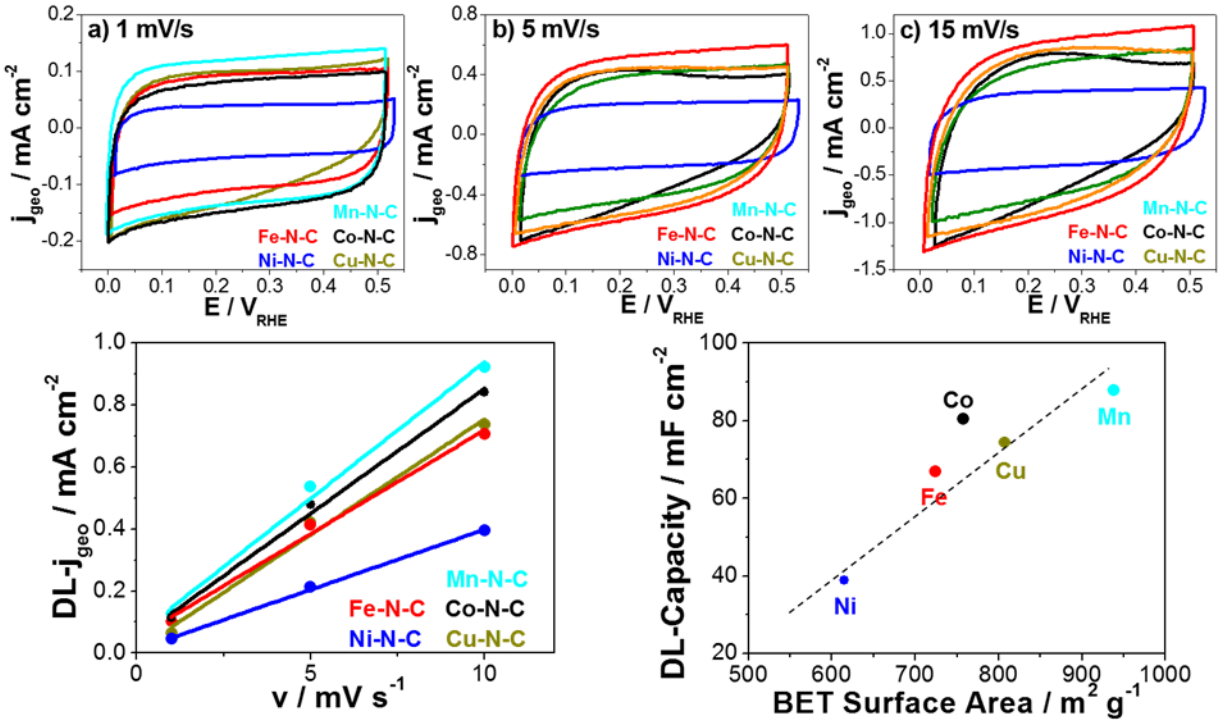

Figure S1- 3 a) to c) Cyclic voltammetry of the five M-N-C catalysts conducted in CO_2 -saturated 0.1 M $KHCO_3$ at various scan rates for estimation of double layer (DL) capacity. d) current densities from a-c plotted vs. electrode potential scan rate to extract the double layer capacity; e) Correlation of double layer capacity and the N_2 adsorption –derived BET surface area.

H_2O adsorption measurements

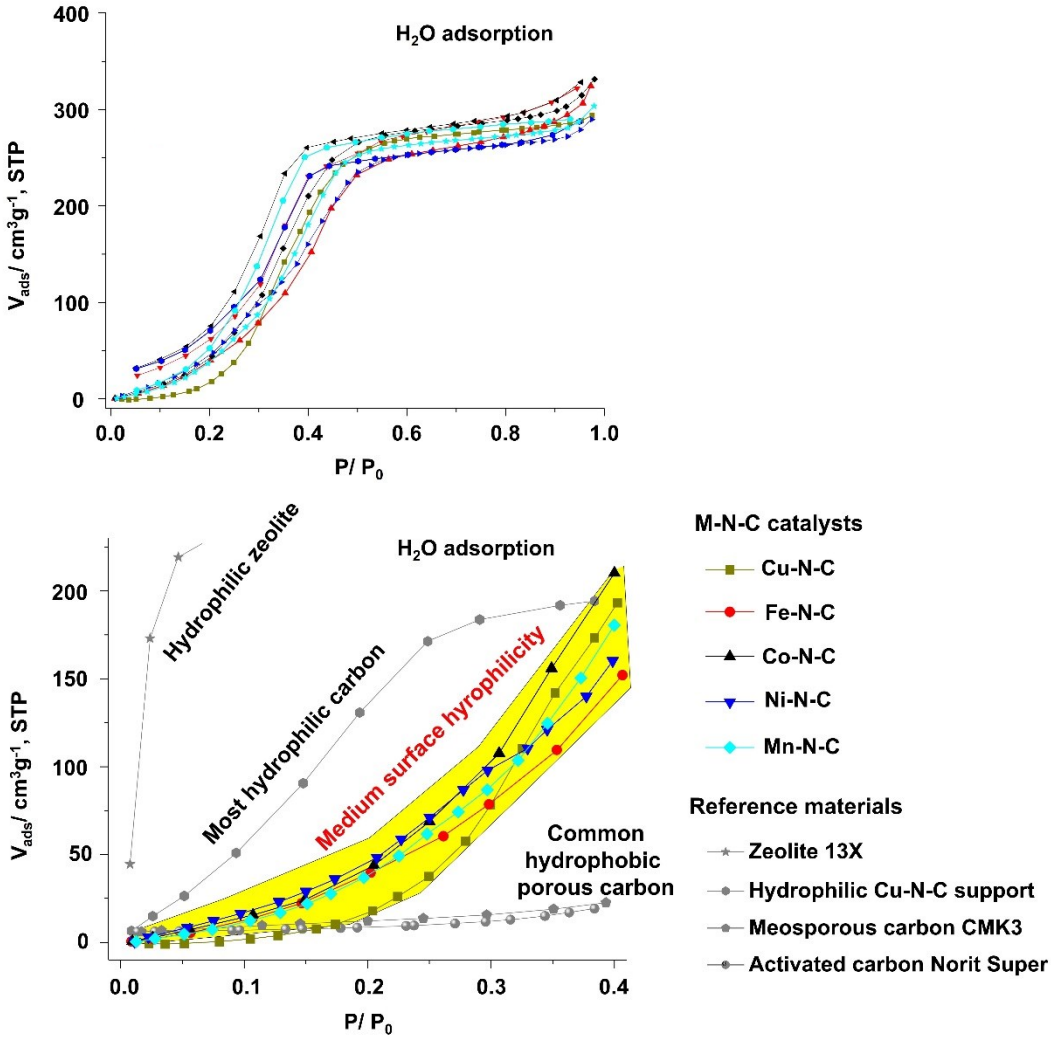

Figure S1- 4 Water vapor adsorption isotherms for this family of M-N-C electrocatalysts (top) with highlighted low pressure regime (bellow) together with typical benchmark samples, including hydrophilic zeolite 13X, most hydrophilic carbon as well as porous carbons (mesoporous CMK-3, commercial activated carbon Norit Super) that commonly show hydrophobic nature. As shown, the surface of this family of M-N-C is medium hydrophilic or hydrophobic as compared with the typical benchmark materials.

X-ray Diffraction Measurements

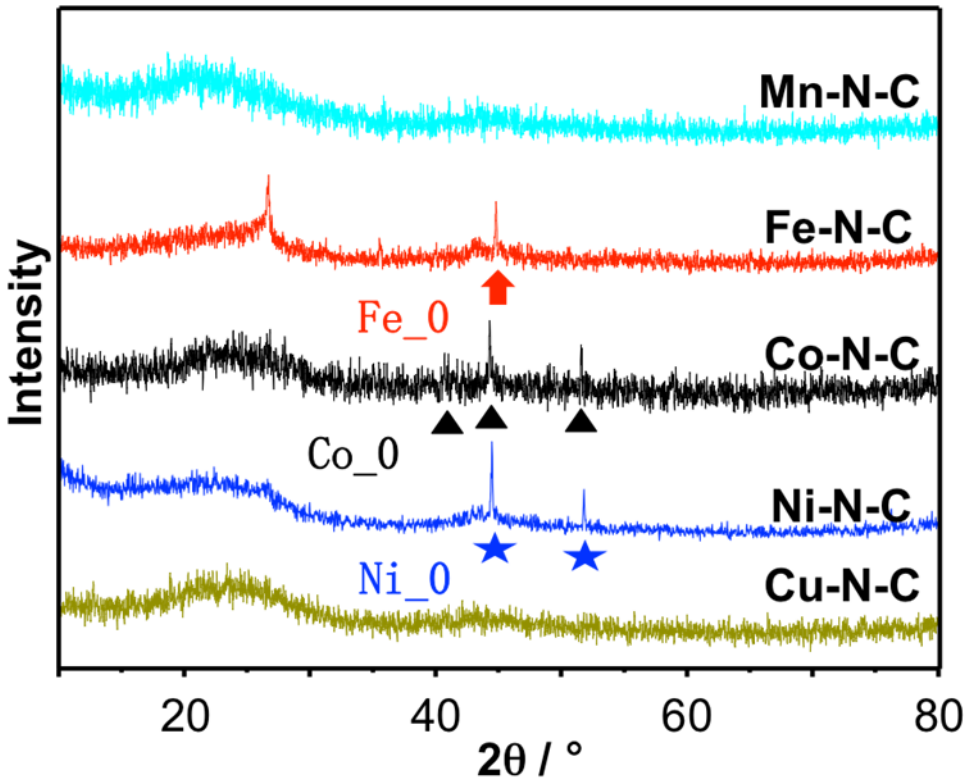

Figure S1- 5 XRD patterns of this family of M-N-C catalysts.

STEM/EDX Dark field microscopy, z Contrast, and elemental mapping

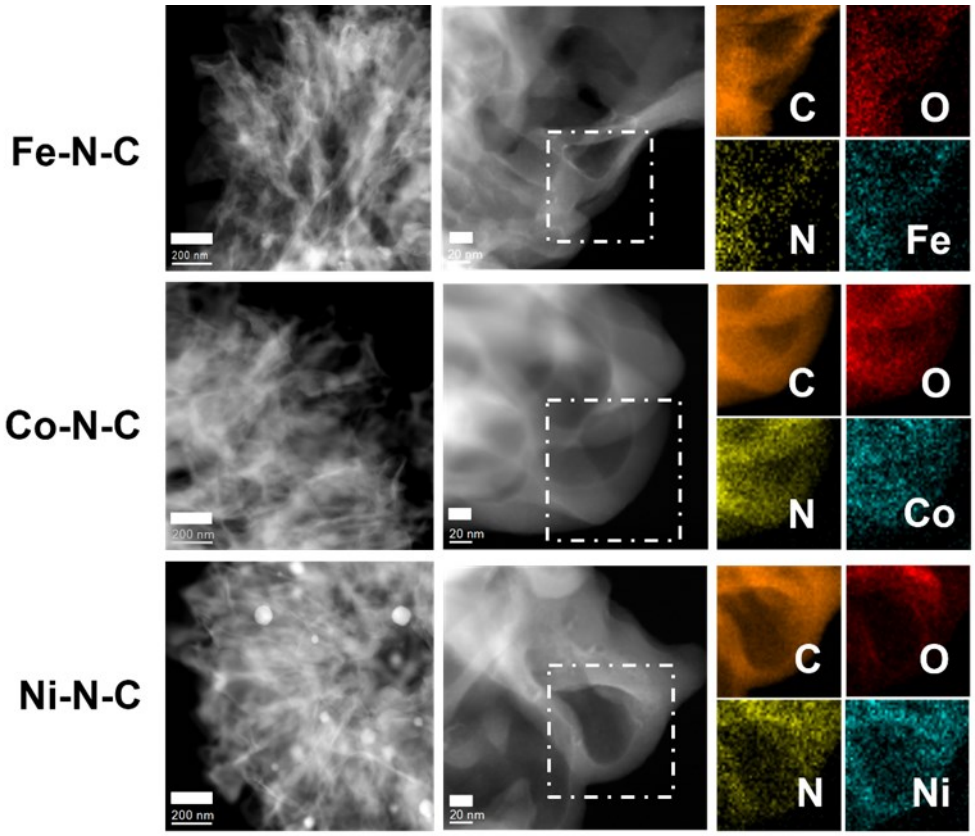

Figure S1- 6 STEM images and elemental maps for Fe-N-C, Co-N-C and Ni-N-C; Scale bar in left column: 200 nm, middle column: 20 nm.

High Resolution X-ray photoemission spectroscopy

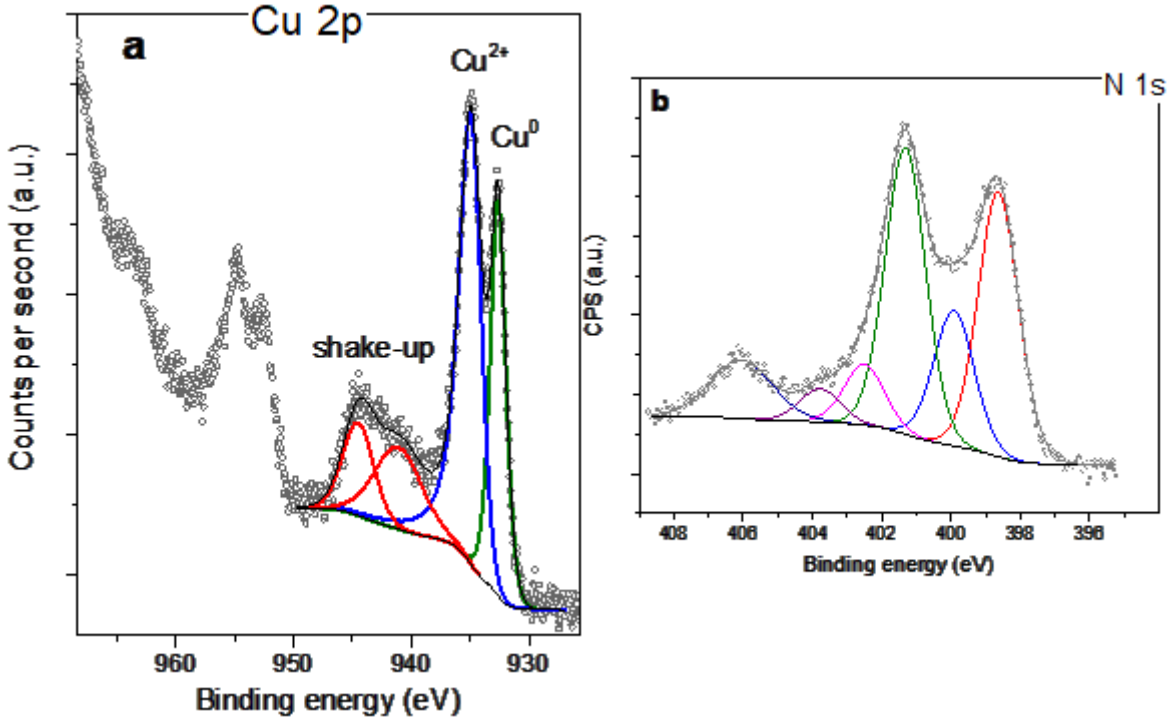

Figure S1- 7 High-resolution Cu 2p (a) and N 1s (b) XP spectra of the Cu-N-C sample. See main text for N 1s peak assignment.

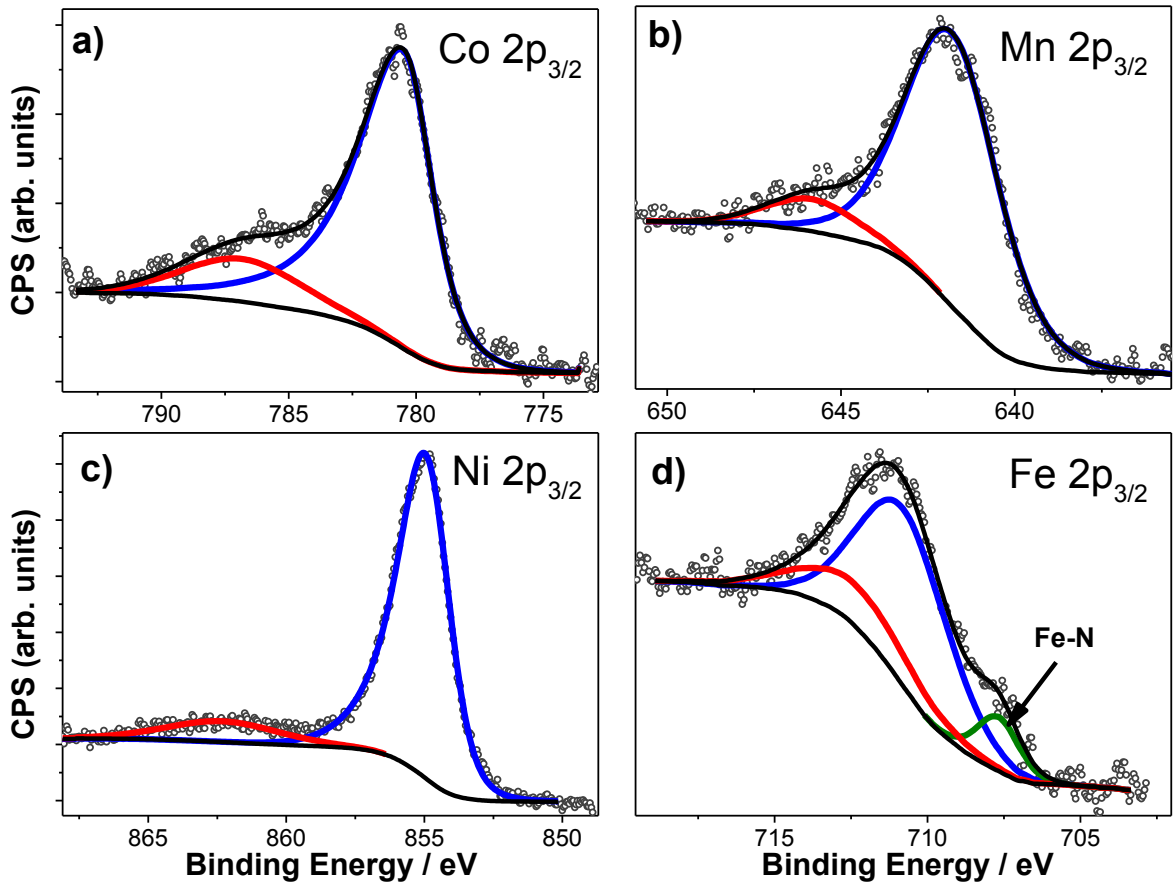

Figure S1- 8 High-resolution metal 2p3/2 of Co-N-C (a), Mn-N-C (b), Ni-N-C (c) and Fe-N-C (d). Blue lines represent 2p3/2 main peaks, red – the corresponding shake-up satellites.

Table S1- 2 Metal atom, nitrogen content and assignment of the different N species in the M-N-C CO2RR electrocatalysts extracted from XPS data. Total metal and nitrogen content are calculated from measured XP spectra areas using instrument-specific relative sensitivity factors provided by manufacturer (SPECS).

Sample	Metal[a] atom %	Nitrogen[a] atom%	Fitting of Nitrogen moieties / atom%					
			Metal-N	Pyridinic	Pyrrolic	Graphitic	N-O_x	CH-Ox
Mn-N-C	Mn: 0.2	8.2	12.2	25.8	43.9	10.3	5.0	2.8
Fe-N-C	Fe: 0.3	8.2	10.4	24.2	44.6	11.7	6.0	3.1
Co-N-C	Co: 0.4	10.5	13.4	28.1	41.6	9.8	4.4	2.7
Ni-N-C	Ni: 0.7	9.5	20.2	17.1	43.6	10.7	5.3	3.2
Cu-N-C	Cu: 0.8	14.6	15.5	30.4	32.9	7.0	3.9	10.3

Catalytic Activity Testing - Total Faradic current densities

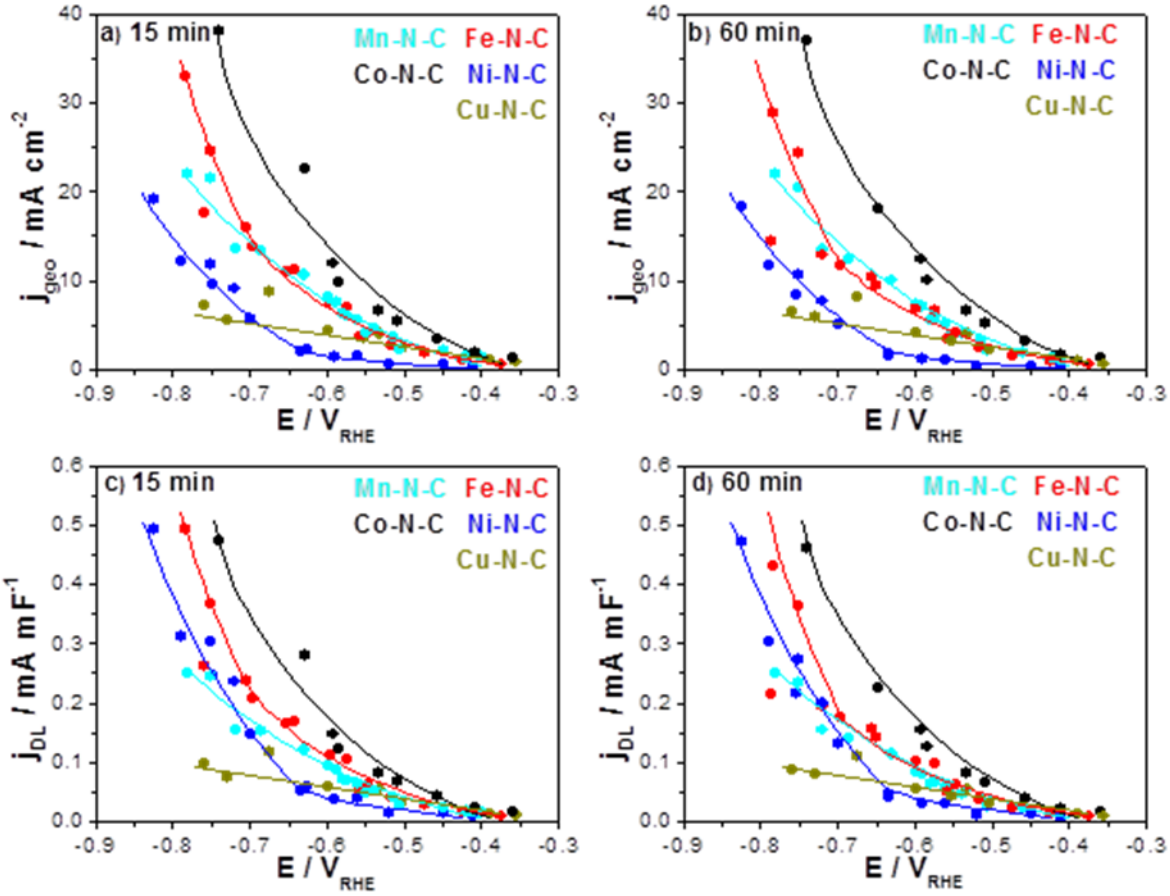

Figure S1- 9 Stationary potentiostatic catalytic activity of Cu-N-C (grey), Fe-N-C (red), Ni-N-C (blue), Mn-N-C (cyan) and Co-N-C (black) catalysts during bulk CO_2 electrolysis. Geometric current densities at a) 15 min b) 60min. Double layer capacity -normalized stationary current densities: c) 15 min d) 60 min. Lines to guide the eye. Conditions: CO_2-saturated 0.1 M $KHCO_3$, 0.76 mg cm^{-2} catalyst loading

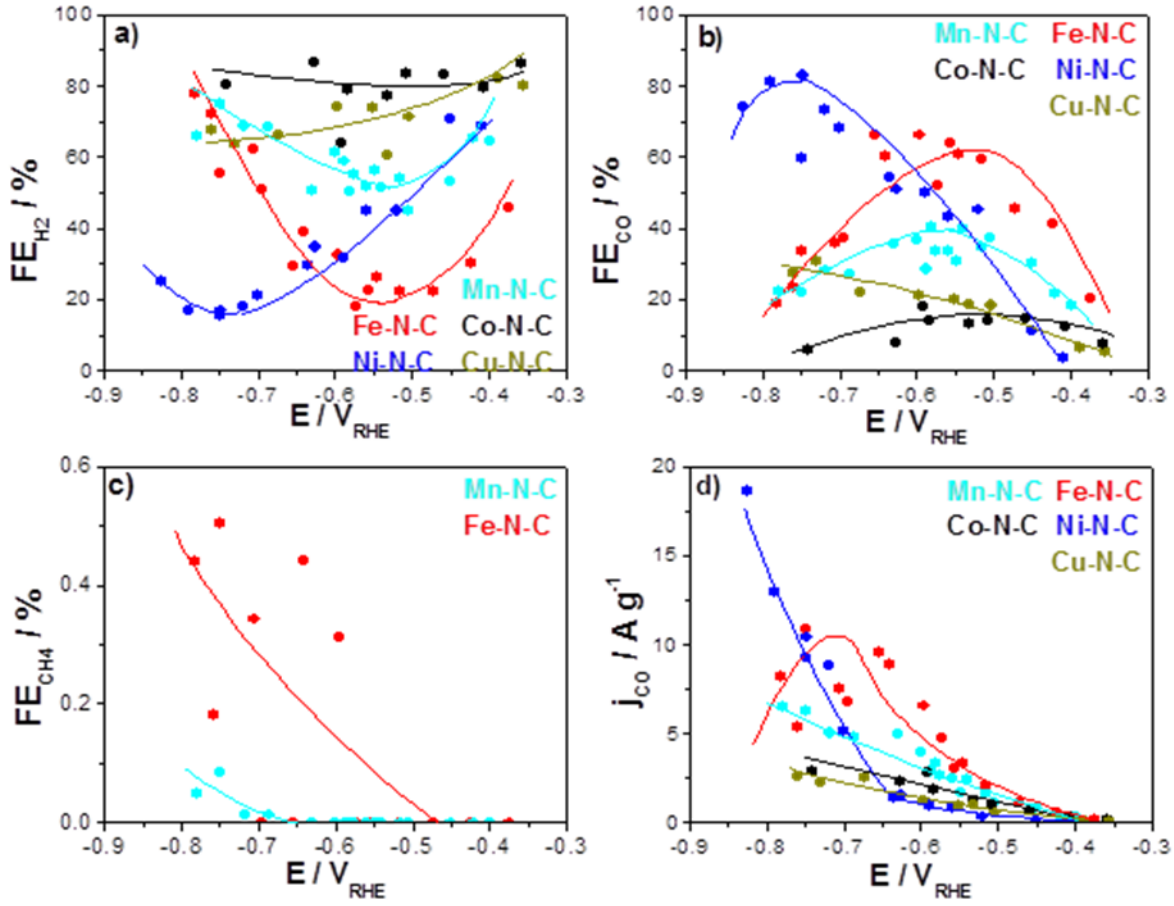

Figure S1- 10 Product efficiencies and yields. CO a) Faradaic efficiency and Absolute value of geometric reduction current density during bulk CO_2 electrolysis on Cu-N-C (gold), Fe-N-C (red), Ni-N-C (blue), Mn-N-C (cyan) and Co-N-C (black). Lines to guide the eye. Conditions: 15 min at constant electrode potential in CO_2-saturated 0.1 M $KHCO_3$ at 0.76 mg cm^{-2} catalyst loading

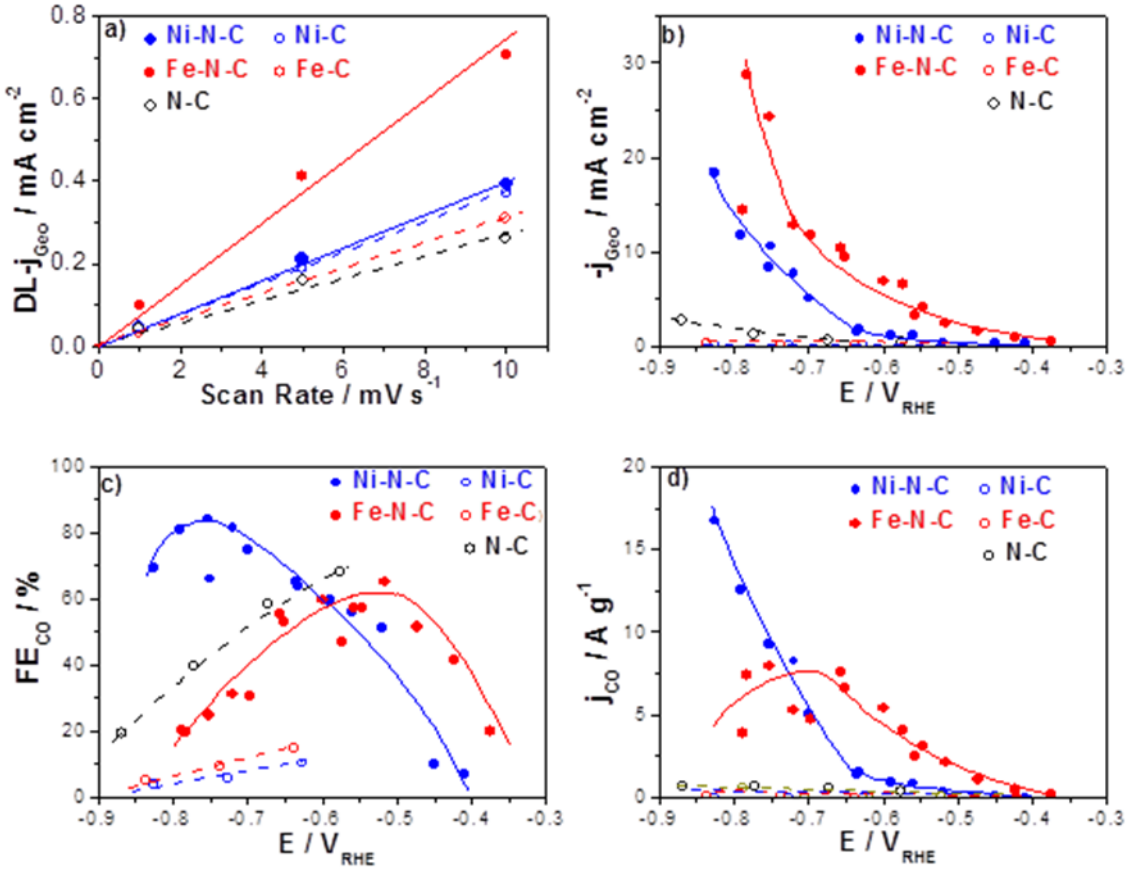

Figure S1- 11 Catalytic performance of Ni-N-C, Ni-C, Fe-N-C, Fe-C and N-C for CO_2RR in 0.1 M CO_2 saturated $KHCO_3$ electrolyte, a) Double layer capacity, b) Absolute total geometric current density, c) Faradaic Efficiency towards CO and d) Mass normalized CO partial current density at 60 min of CO_2 bulk electrolysis. Guide for the eye lines are shown. Catalyst loading: 0.76 mg cm^{-2}.

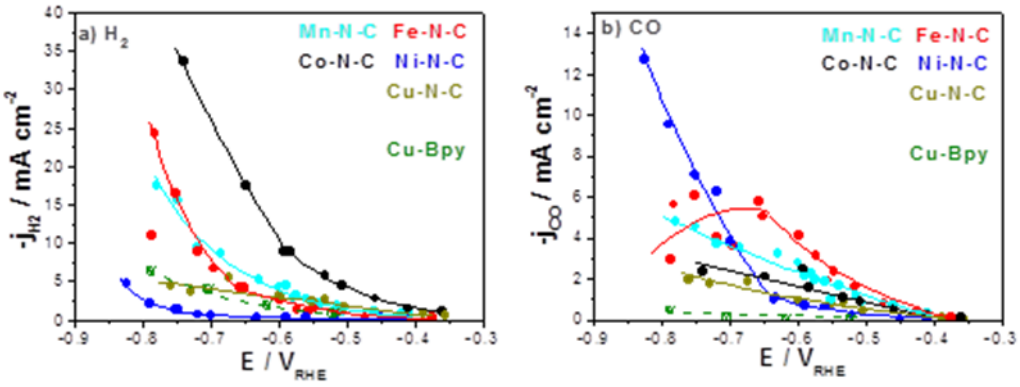

Figure S1- 12 Catalytic performance of Mn-N-C, Fe-N-C, Co-N-C, Ni-N-C, Cu-N-C and Cu-Bpy for CO_2RR in 0.1 M CO_2 saturated $KHCO_3$ electrolyte. Geometric partial current density for a) H_2 and b) CO at 60 min of CO_2 bulk electrolysis. Lines to guide the eye. Catalyst loading: 0.76 mg cm^{-2}.

DFT Calculations at 0V_{RHE} and -0.6 V_{RHE}

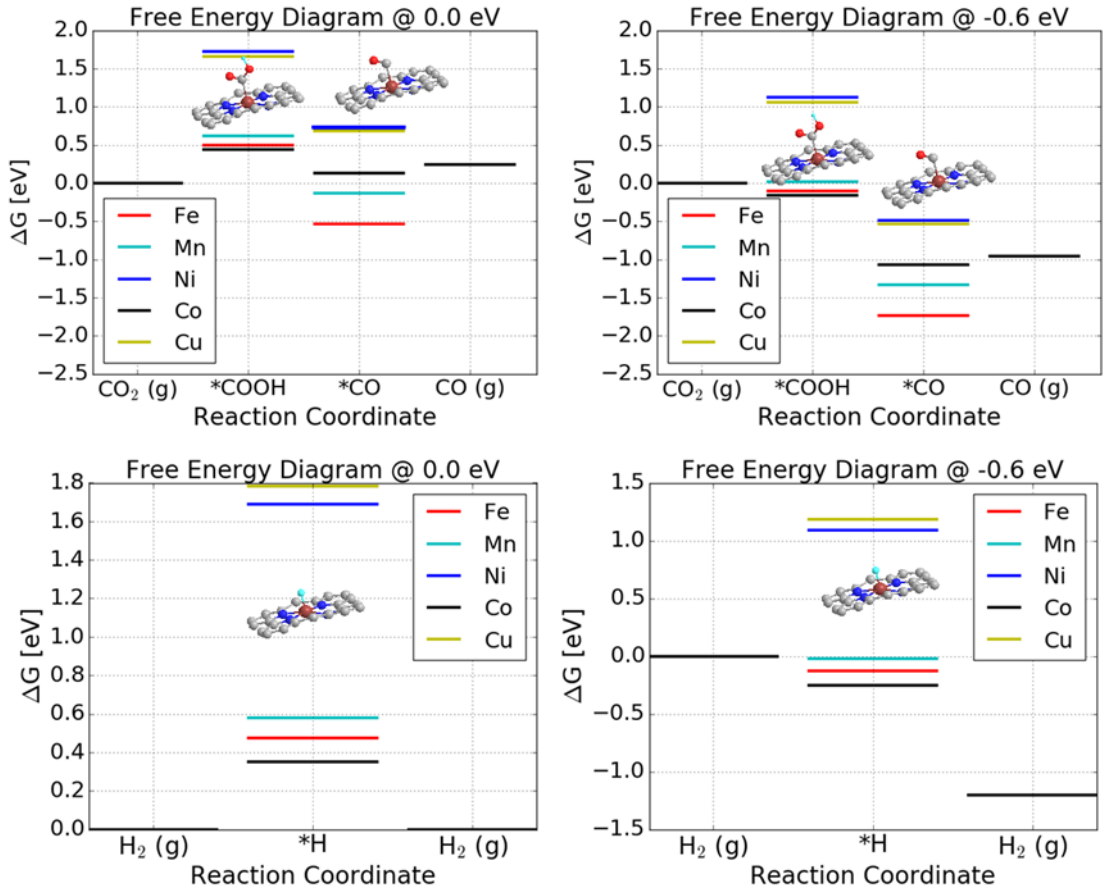

Figure S1- 13 DFT-calculated free energy diagram for the CO_2 reduction reaction (CO_2RR) and hydrogen evolution reaction (HER) at 0 V_{RHE} (a,c) and -0.6 V_{RHE}.

CO production TOF trends – Correlation of experiments with theory

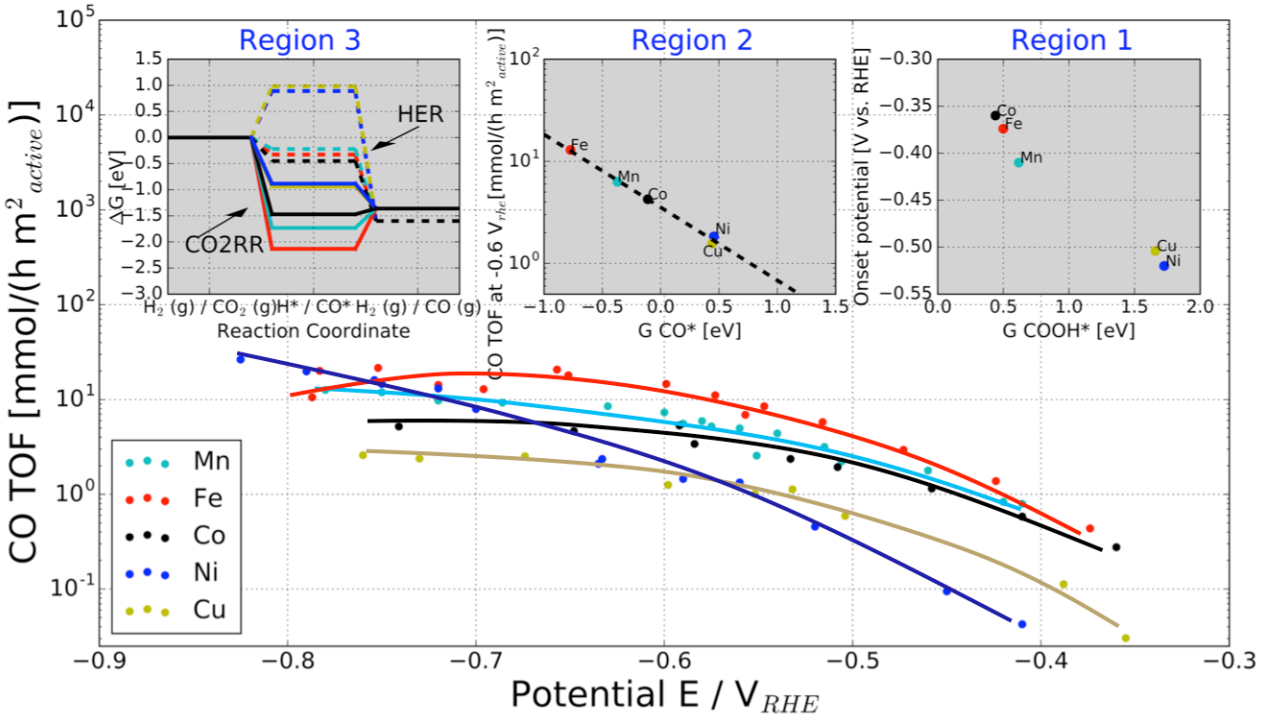

Figure S1- 14 Experimental CO production turnover frequency (TOF) of the M-N-C catalysts versus applied iR-corrected electrode potential (see Equation SI 3). The catalytic reactivity trends split into 3 potential regions with distinctly different rate-determining mechanistic features. Insets: Region 1: Low overpotentials, the experimental onset potential of CO production correlates with the binding energy of the reaction intermediate COOH*. Region 2: Intermediate over-potentials, CO production TOF at -0.6 V_{RHE} vs. free energy of adsorbed CO, CO*; Region 3: High overpotentials, free energy diagrams for the HER (dashed paths) and CO2RR (solid paths) at -0.8 V_{RHE} for each M-N-C catalyst. HER barriers are high for Ni and Cu, while CO2RR is downhill making these materials favorable CO producing catalysts.

A2. Supplementary Information to Chapter 5

Table S2- 1 Physiochemical characterization

Sample	a) BET $m^2\ g^{-1}$	b) DL-Capa $\mu F\ cm^{-2}$	c) Metal content wt.% (ICP)	d) Metal ratio $\%_{Mole}$ (XPS)	N ratio $\%_{Mole}$	O ratio $\%_{Mole}$	S ratio $\%_{Mole}$	C ratio $\%_{Mole}$	e) CO uptake $mmol\ g^{-1}$
Fe-N-C	634	72.4	1.05	0.82	5.93	3.55	0.53	88.92	60
Ni-N-C	238	22.5	10.2	0.38	3.67	1.91	1.17	92.88	0
N-C	174	25.3	--	--	6.68	3.39	1.03	88.9	0

a) BET: N_2 ad/desorption-based surface area; b) Double layer capacity values, geometric area of each electrode is 1 cm^2 with 0.75 mg cm^{-2} catalyst loading; c) Overall metal content determined from ICP-OES measurement. d) Interfacial atomic ratio quantified with X-ray photoelectron spectra. e) CO uptake at -80°C based on CO chemisorption measurement.

X-Ray Diffraction profiles:

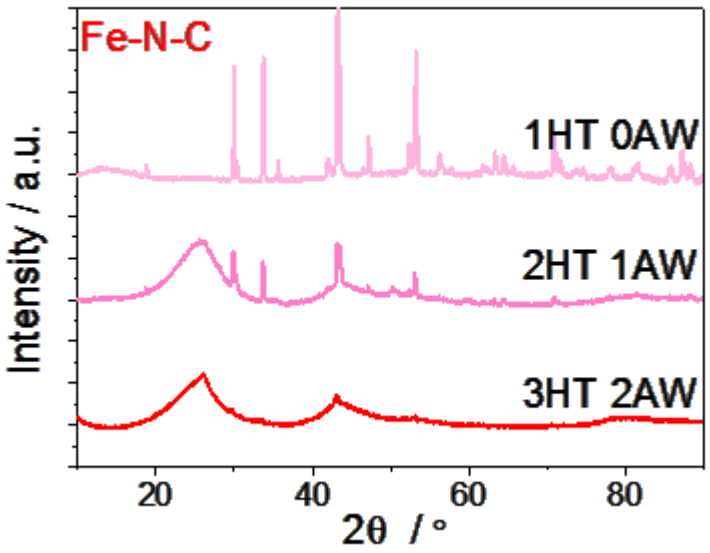

Figure S2- 1 Powder XRD patterns of the Fe-N-C materials without (1HT, 0AW), with one time (2HT, 1AW) and with two times (3HT, 2AW) acid-washing during the synthesis approach.

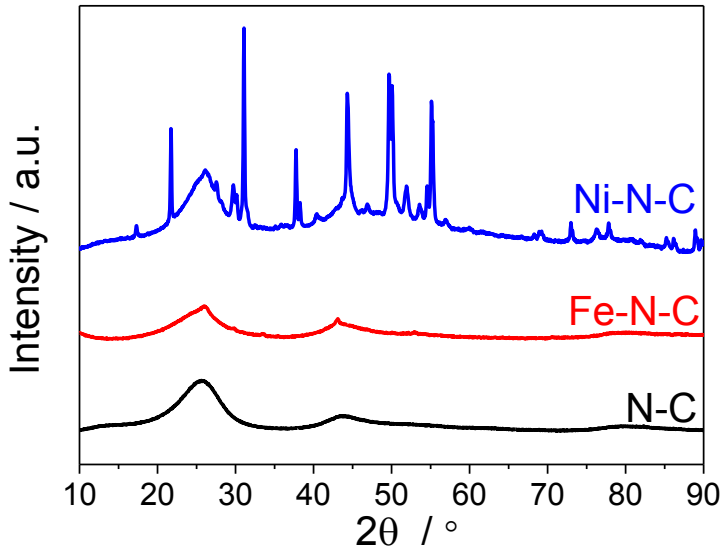

Figure S2- 2 Powder XRD patterns of N-C, Fe-N-C and Ni-N-C catalysts.

TEM image of encapsulated crystalline nanoparticles in Ni-N-C catalyst

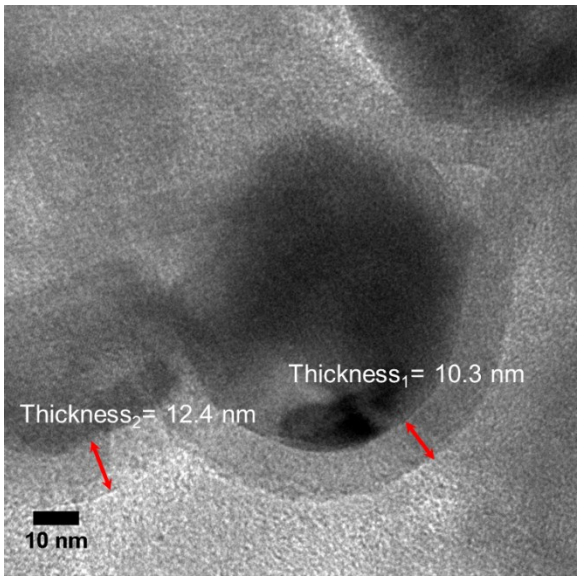

Figure S2- 3 HR-TEM image of carbon-encapsulated crystalline nanoparticles in Ni-N-C catalyst.

BET surface area and Pore size distribution:

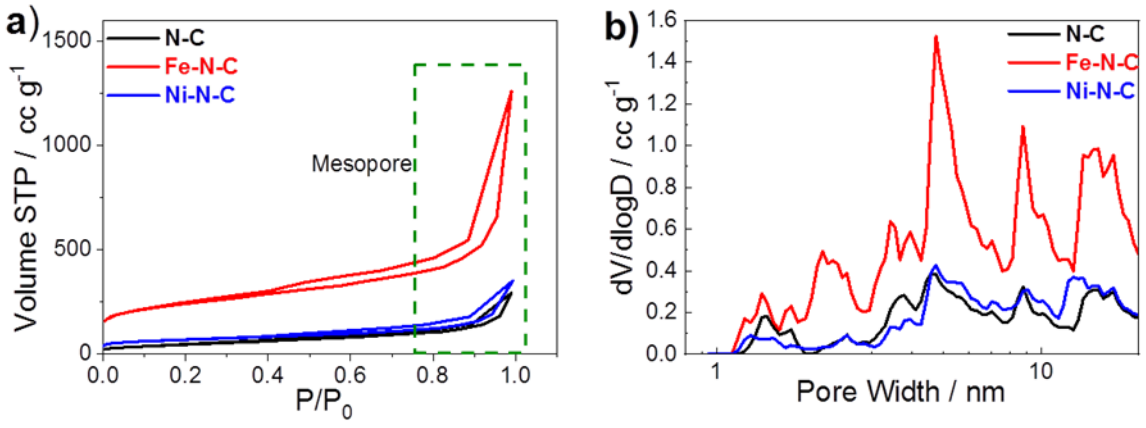

Figure S2- 4 a) N_2 specific ad/desorption isotherm profile; b) pore size distribution of the N-C, Fe-N-C and Ni-N-C catalysts.

Interfacial surface area determination: BETSA vs. ECSA

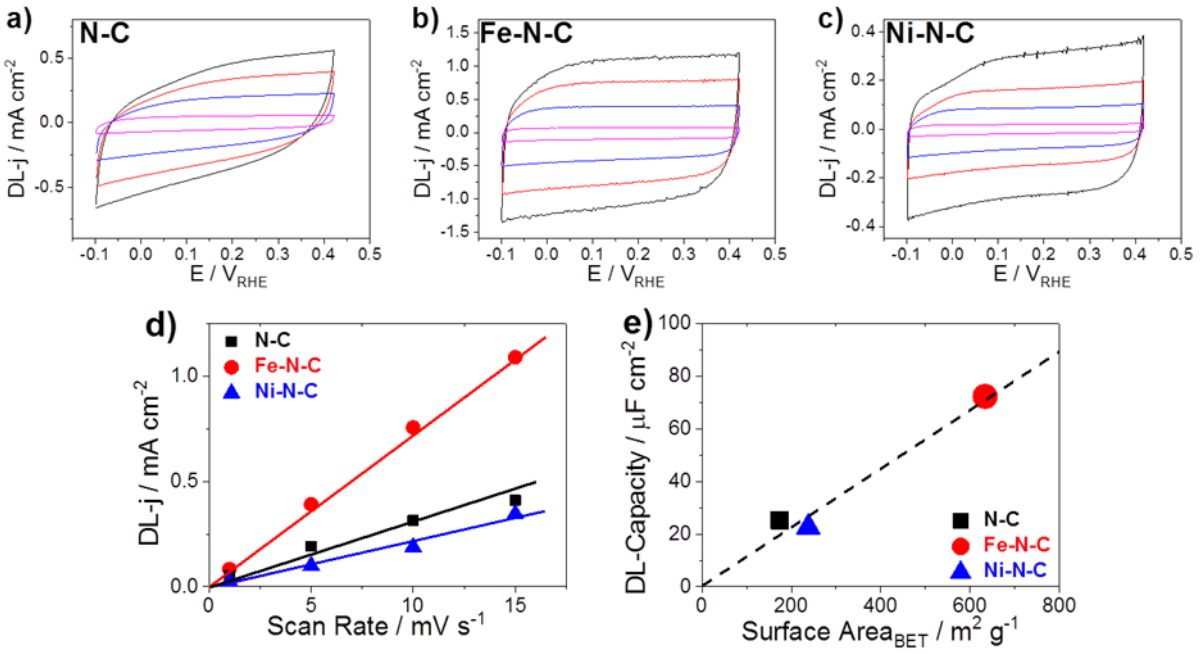

Figure S2- 5 Cyclic voltammetry of a) N-C, b) Fe-N-C and c) Ni-N-C catalysts conducted in N_2-saturated 0.05 M K_2HPO_4 + 0.05 M KH_2PO_4 (pH=6.9) solution at scan rate 15 mV s^{-1}, 10 mV s^{-1}, 5 mV s^{-1}, 1 mV s^{-1} to determine the double layer capacity. Potential was scanned between -0.1 and 0.42 V vs. RHE. d) Double layer current densities (extracted at +0.16 V_{RHE}) on N-C, Fe-N-C and Ni-N-C catalysts at each scan rate. e) Correlation of double layer capacity (ECSA) and the N_2 adsorption derived BET surface area (BETSA). Catalysts loading: 0.75 mg cm^{-2}.

X-ray Photoelectron spectra:

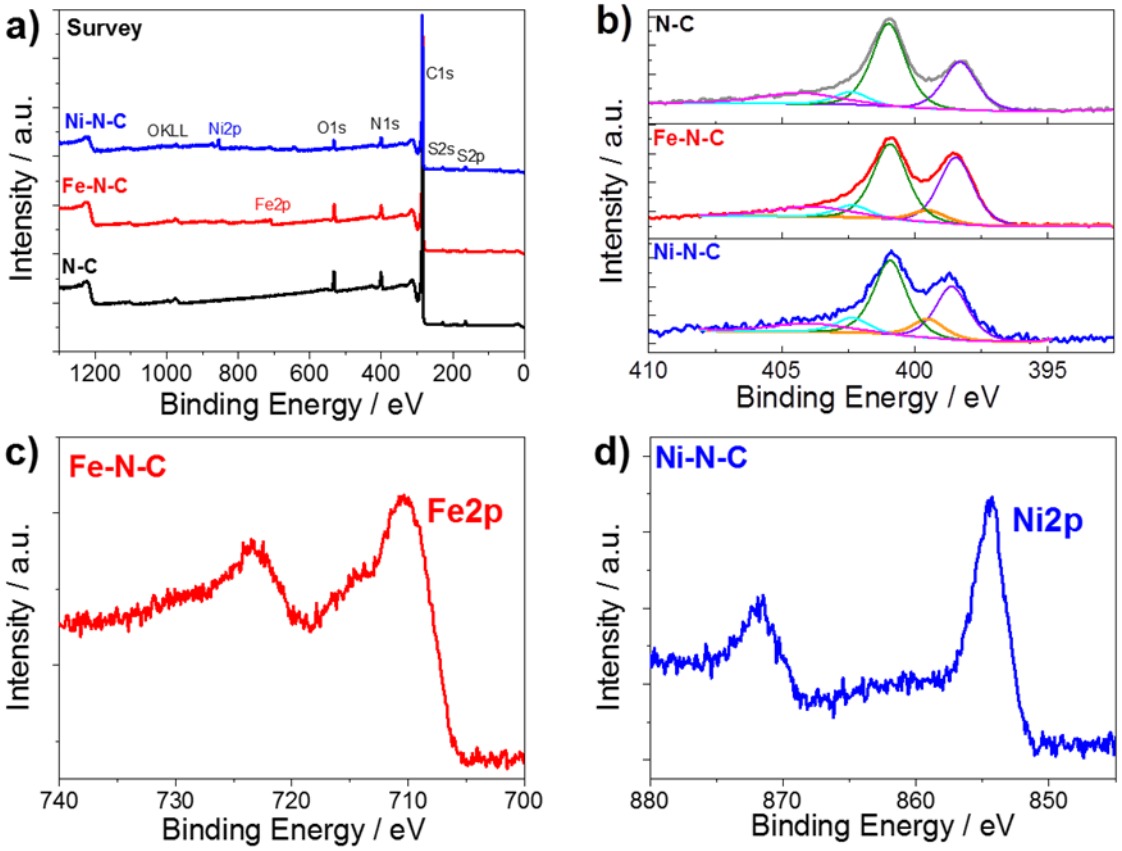

Figure S2- 6 X-ray photoelectron spectra. a) Survey XPS spectra of the PANI derived materials with the main features assigned and high resolution spectra of b) N1s of M-N-C catalysts according to the peak positions: M-N_x moieties (399.7 eV), pyrrolic (401.3 eV), pyridinic (398.6 eV), quaternary (402.5 eV), and graphitic (403.9 eV) according to ref[50,61,81] c) Fe2p assignment of Fe-N-C and d) Ni2p of Ni-N-C. Please note, XPS data on Fe-N-C and N-C catalysts were already reported in ref[43,] but measured with other spectrometers.

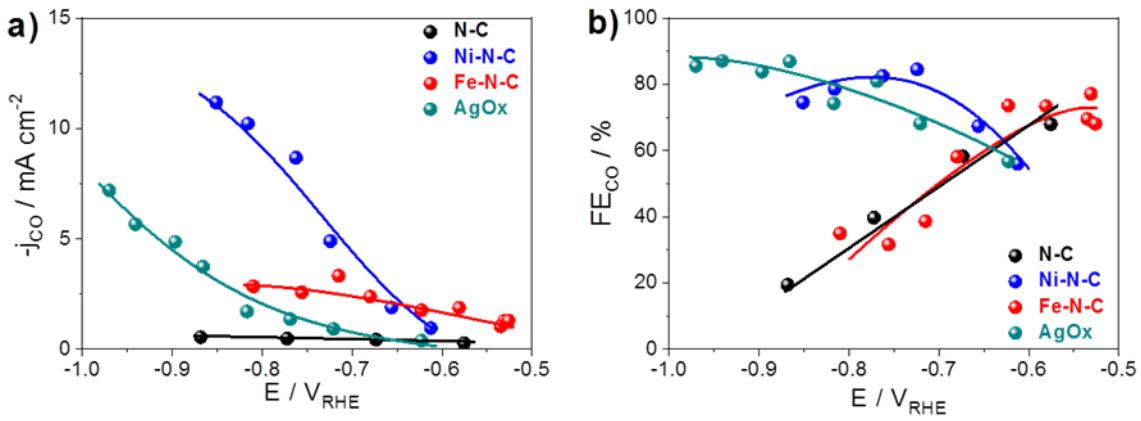

Figure S2- 7 a) Geometric CO production current densities and b) CO faradaic efficiency as a function of applied iR-corrected electrode potential. Lines to guide the eye. Conditions: 60 min at constant electrode potential in CO_2-saturated 0.1 M $KHCO_3$ with 0.75 mg cm^{-2} catalysts loading.

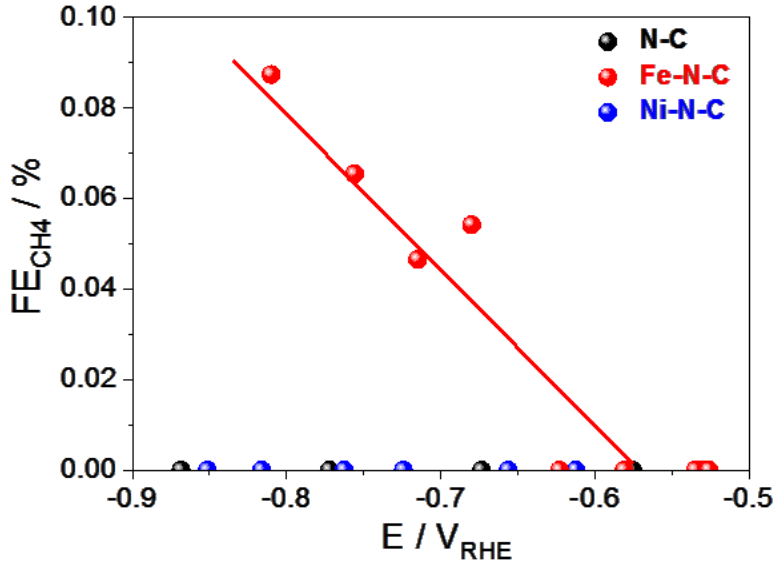

Figure S2- 8 Faradaic efficiency of CH_4 as a function of applied iR-corrected electrode potential. Lines to guide the eye. Conditions: 15 min at constant electrode potential in CO_2-saturated 0.1 M $KHCO_3$ with 0.75 mg cm^{-2} catalysts loading.

DFT calculation of different Ni-Nx-C coordination motifs

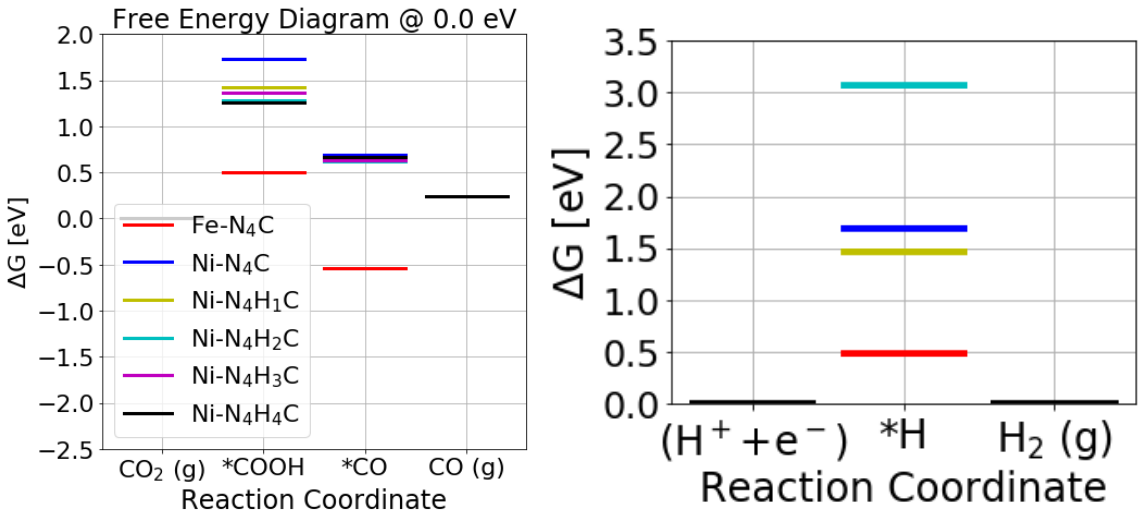

Figure S2- 9 Free energy diagram of CO_2 reduction to CO on the Ni-N-C and Fe-N-C catalysts. Influence of hydrogenating the Ni-N_4-C on the binding strength for the *COOH and *CO intermediate.

Stability test of Electrochemical CO_2RR in the MFC:

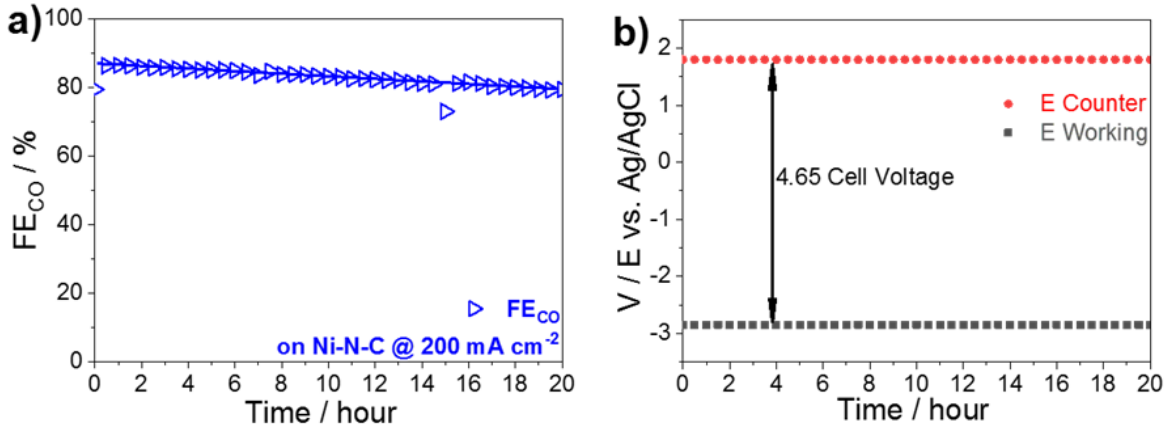

Figure S2- 10 Stability test of Ni-N-C GDL for CO_2RR on in MFC. a) Faradaic efficiency of CO and b) Cell potential (voltage) as a function of stationary electrolysis time. Conditions: 20 hours at constant 200 mA cm^{-2} working current density in CO_2-saturated 1 M $KHCO_3$ with 1 mg cm^{-2} catalysts loading and 3 cm^2 total geometric electrode area. Line to guide the eye.

A3. Supplementary Information to Chapter 6

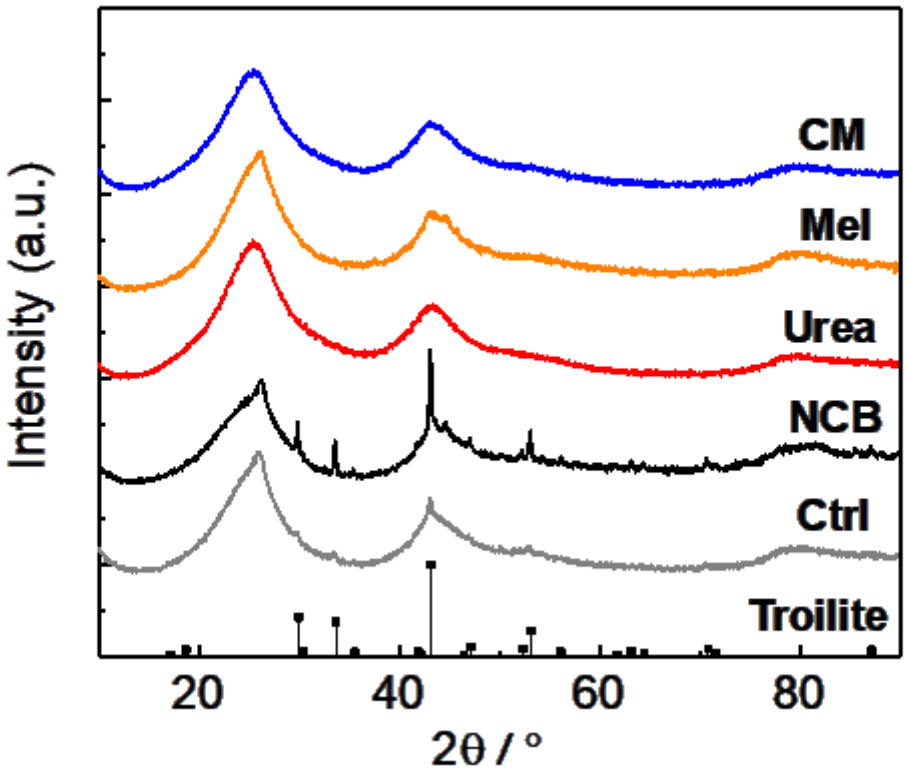

Figure S3- 1 Powder X-ray diffraction of catalysts from this project. At the bottom a diffraction pattern of troilite from Skala et al[121] is displayed.

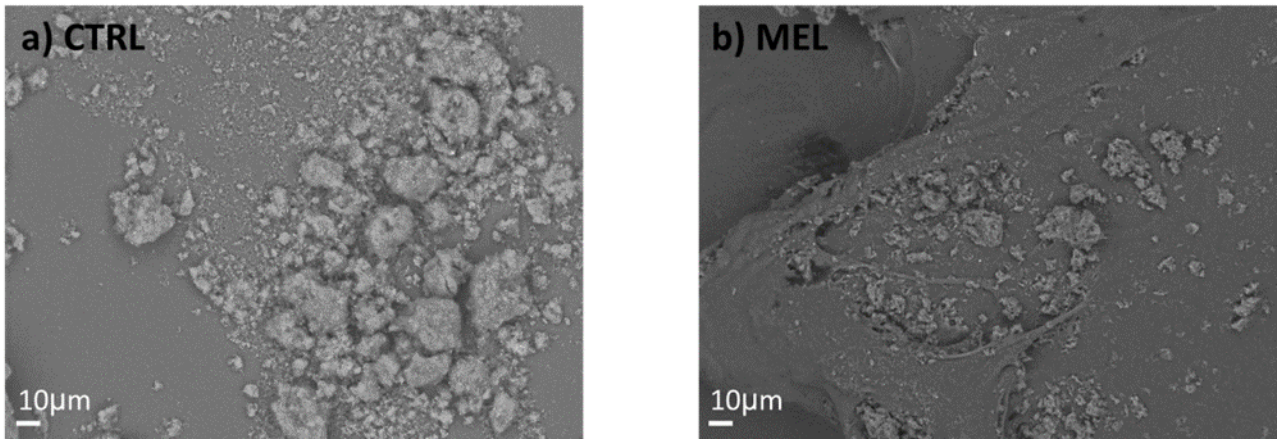

Figure S3- 2 Typical Scanning Electron Microscopy images of a) CTRL and b) MEL PANI-Fe electro-catalysts.

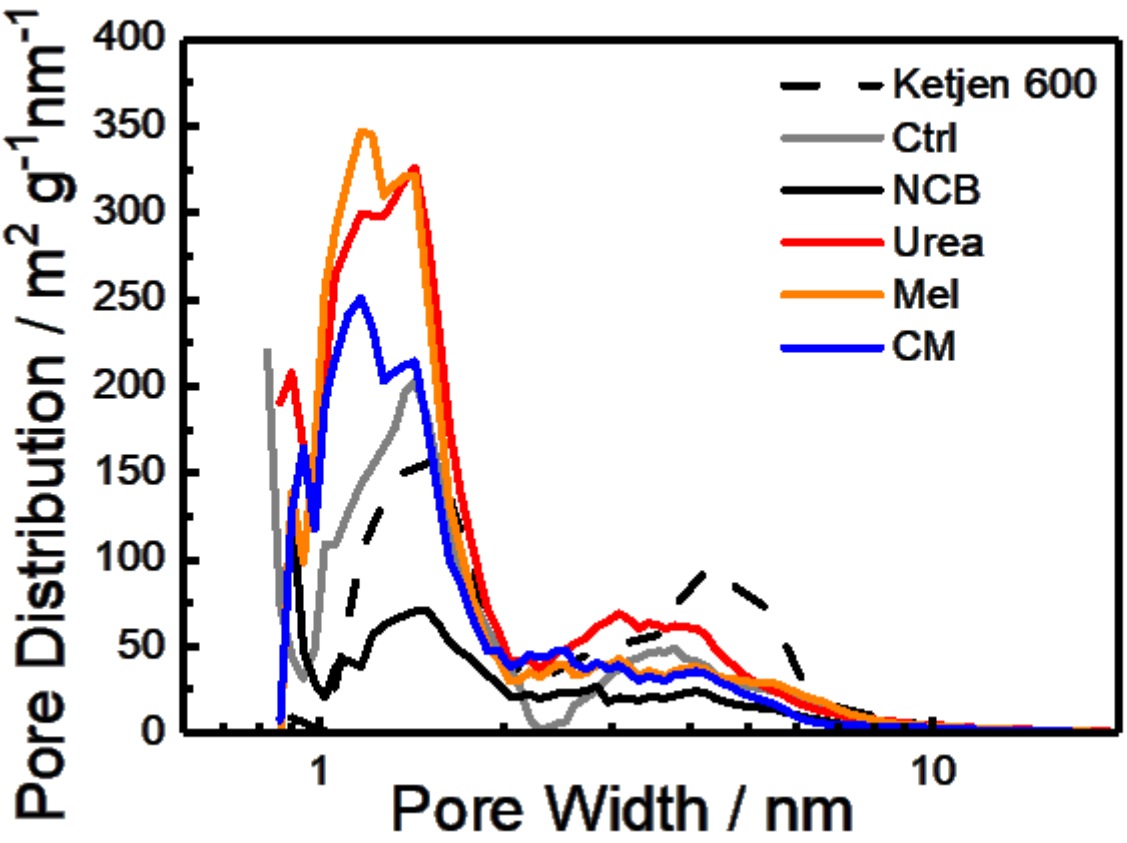

Figure S3- 3 Pore size distribution of support and catalysts.

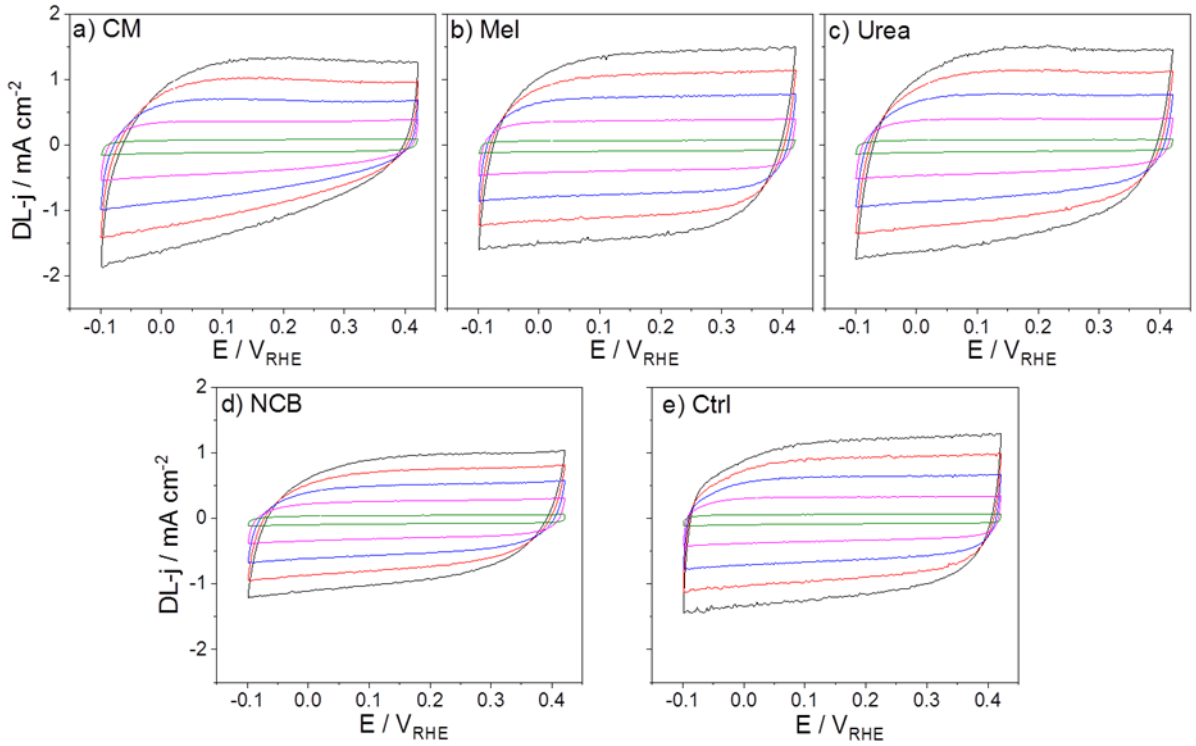

Figure S3- 4 Cyclic voltammetry of the five Fe-N-C catalysts conducted in CO_2-saturated 0.1 M $KHCO_3$ at various scan rates for estimation of the double layer (DL) capacity. a) CM, b) Mel, c) Urea, d) NCB and e) Ctrl. Cycle voltammetry was performed between -0.1 and 0.42 V vs. RHE to avoid the interference of the faradaic process and at the scan rate were 20 mV s^{-1}, 15 mV s^{-1}, 10 mV s^{-1}, 5 mV s^{-1}, 1 mV s^{-1}. Double layer current densities are utilized to determine the double layer capacitance, which is proportional to the double-layer interfacial area. Catalysts loading: 0.75 mg cm^{-2}.

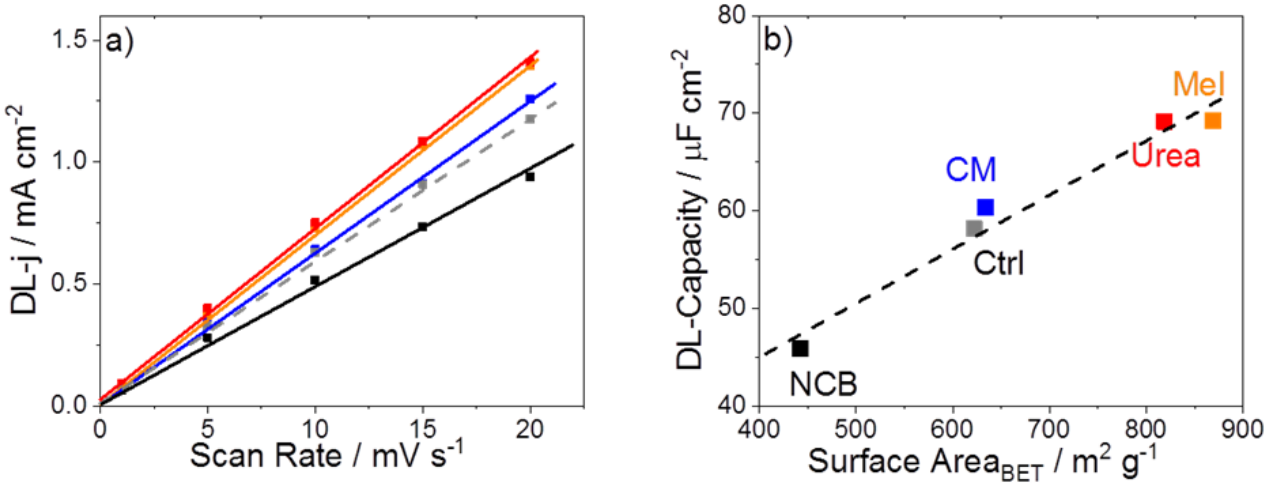

Figure S3- 5 a) Double layer current densities on 5 different Fe-N-C catalysts as a function electrode potential scan rate to extract the double layer capacity; b) Correlation of double layer capacity and the N_2 adsorption derived BET surface area.

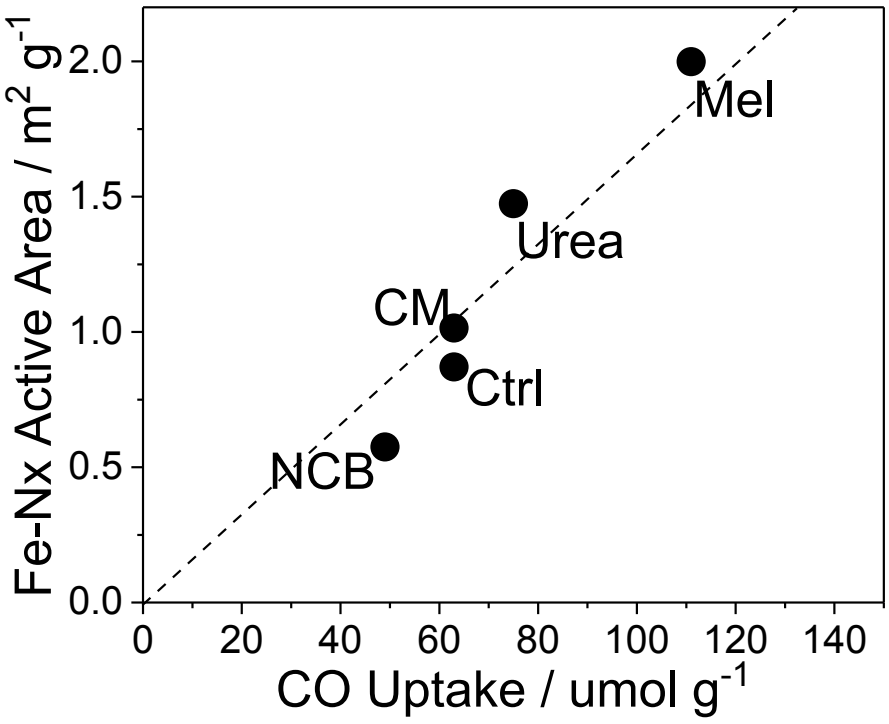

Figure S3- 6 Combination of CO-Chemisorption measurements and interfacial Fe-Nx sites area.

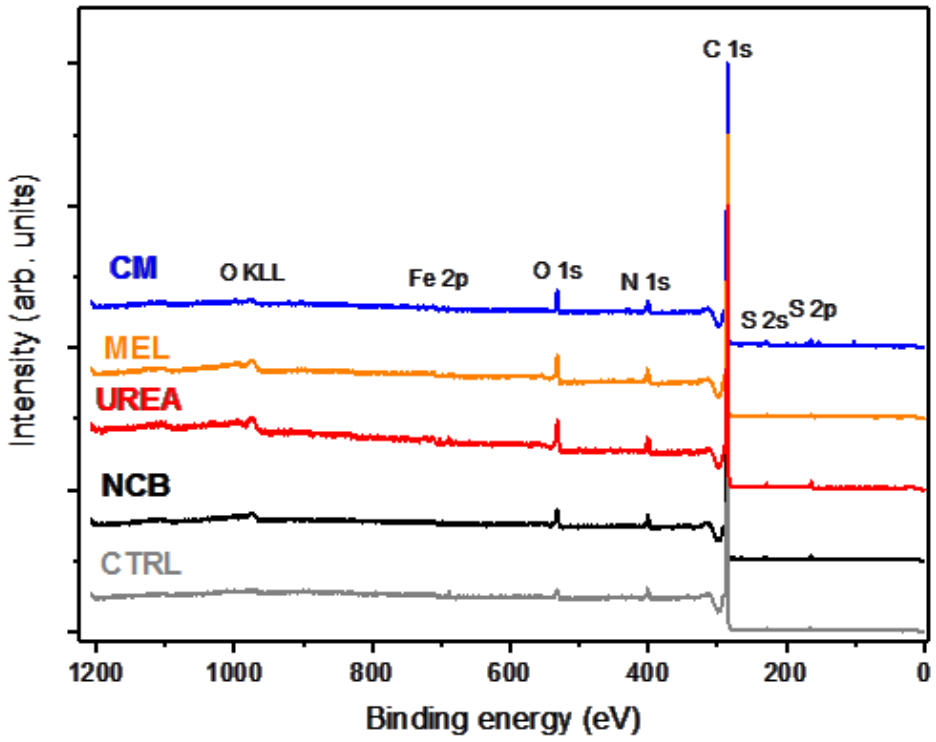

Figure S3- 7 Survey XPS spectra of Fe-PANI materials with the main features assigned.

Table S3- 1 Atomic ratio of various elements determined using X-ray photoelectron spectra.

Sample	C	N	O	S	Fe
NCB	94.8	2.9	1.7	0.5	0.1
CTRL	93.3	3.3	3.1	0.2	0.1
CM	93.1	3.9	1.6	1.3	0.2
MEL	90.9	3.6	4.8	0.5	0.2
UREA	92.8	3.7	2.0	1.3	0.2

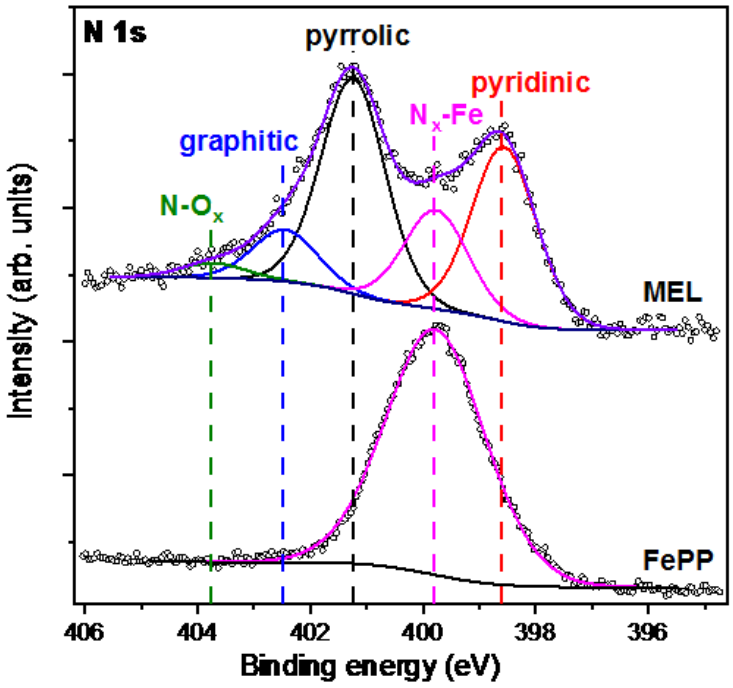

Figure S3- 8 High resolution N 1s XPS spectra of a PANI-Mel sample and Fe-Protoporphyrin (Sigma-Aldrich).

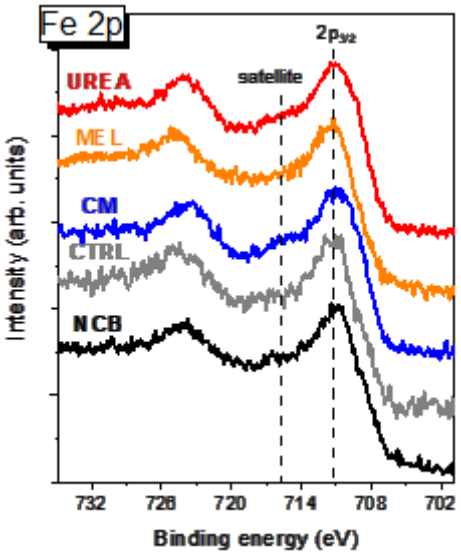

Figure S3- 9 Fe 2p high resolution XPS spectra of Fe-PANI catalysts.

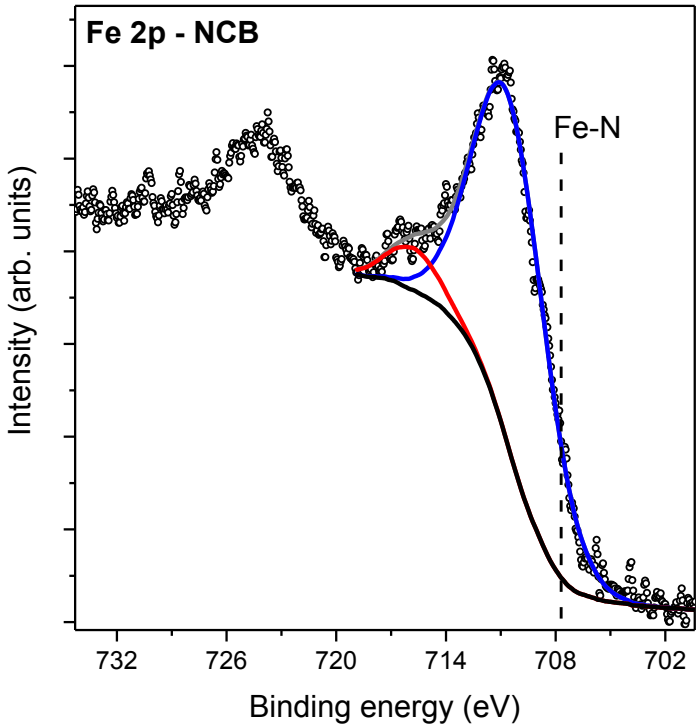

Figure S3- 10 Deconvolution of Fe $2p_{3/2}$ XPS spectrum representative of the NCB sample. Open dots show experimental data, solid blue line – main Fe $2p_{3/2}$ peak, solid red line – shake up satellite. Vertical dashed line shows position of $Fe2p_{3/2}$ reported for Fe-porphyrin.

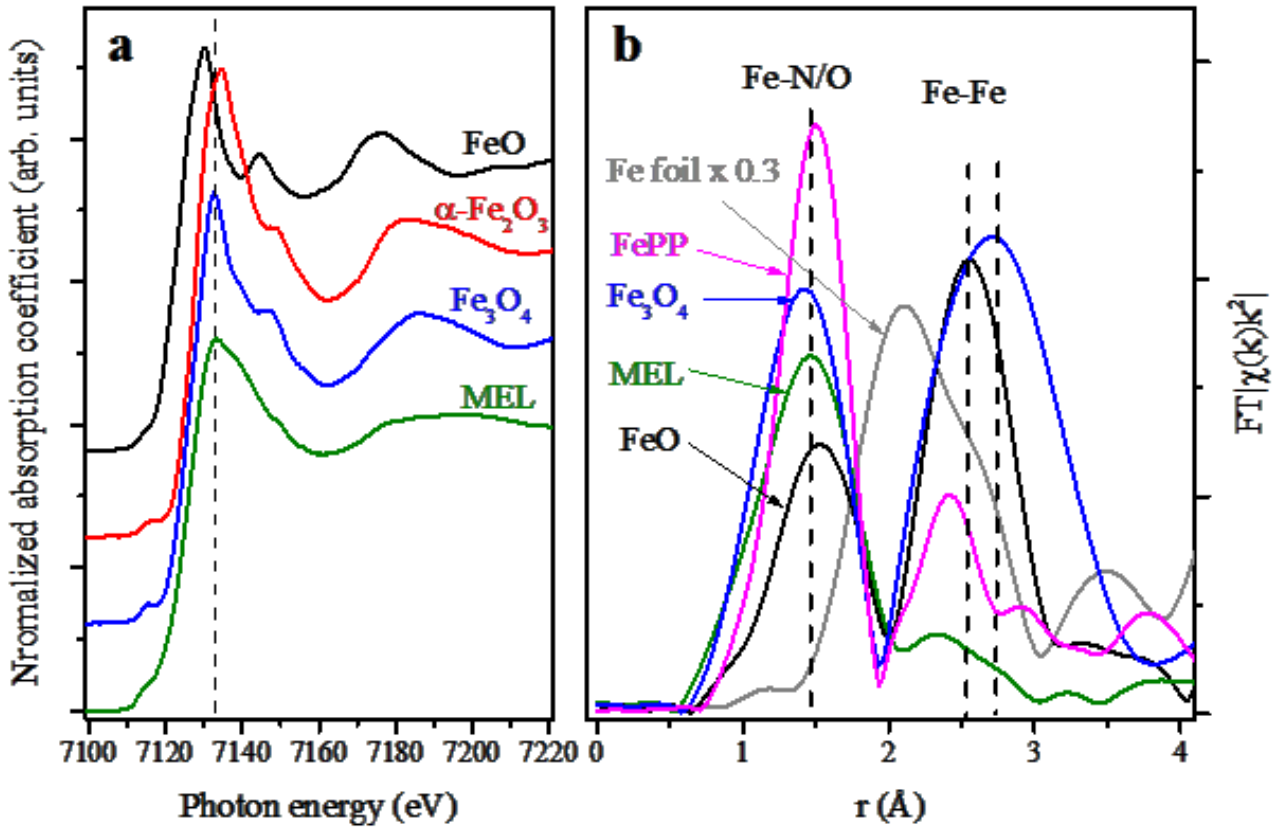

Figure S3- 11 Fe K-edge XANES (a) and EXAFS (b) spectra of Fe-PANI MEL sample, iron foil, commercial iron protoporphyrin (FePP, Sigma Aldrich) and the most common iron oxides. The intensity of iron foil spectrum in (b) is reduced by factor of 3 for better display.

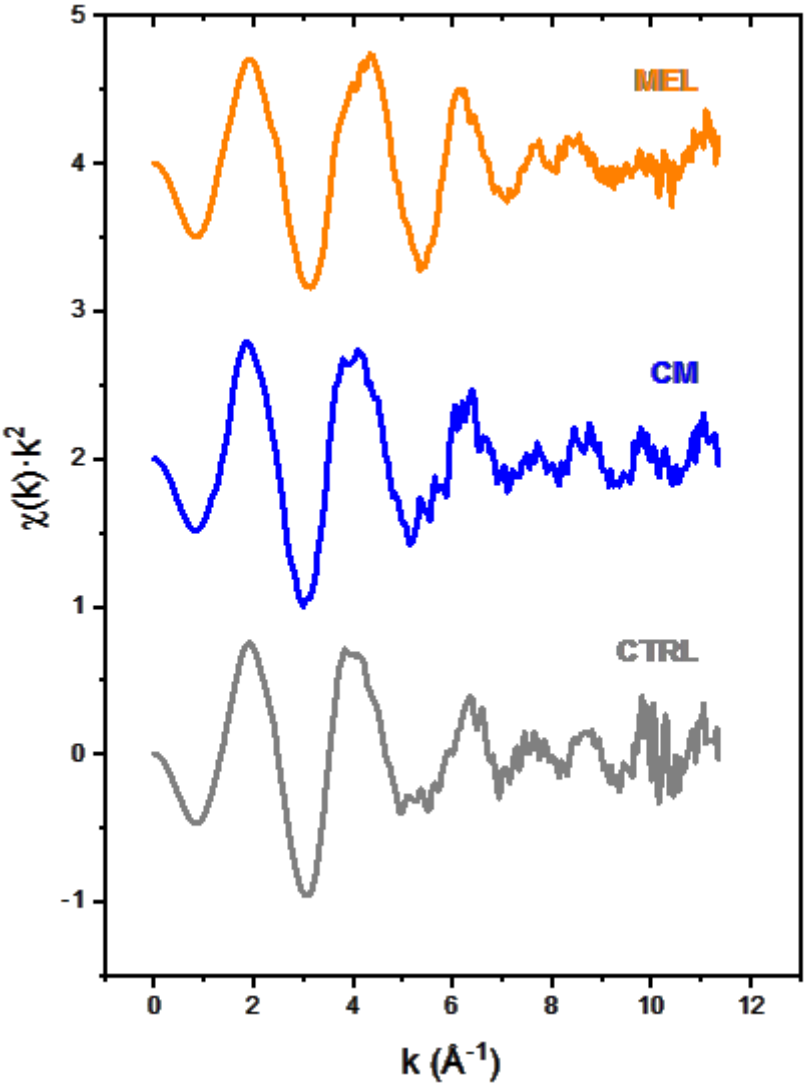

Figure S3- 12 Fe K-edge k2-weighted EXAFS data of Fe-PANI samples in k-space.

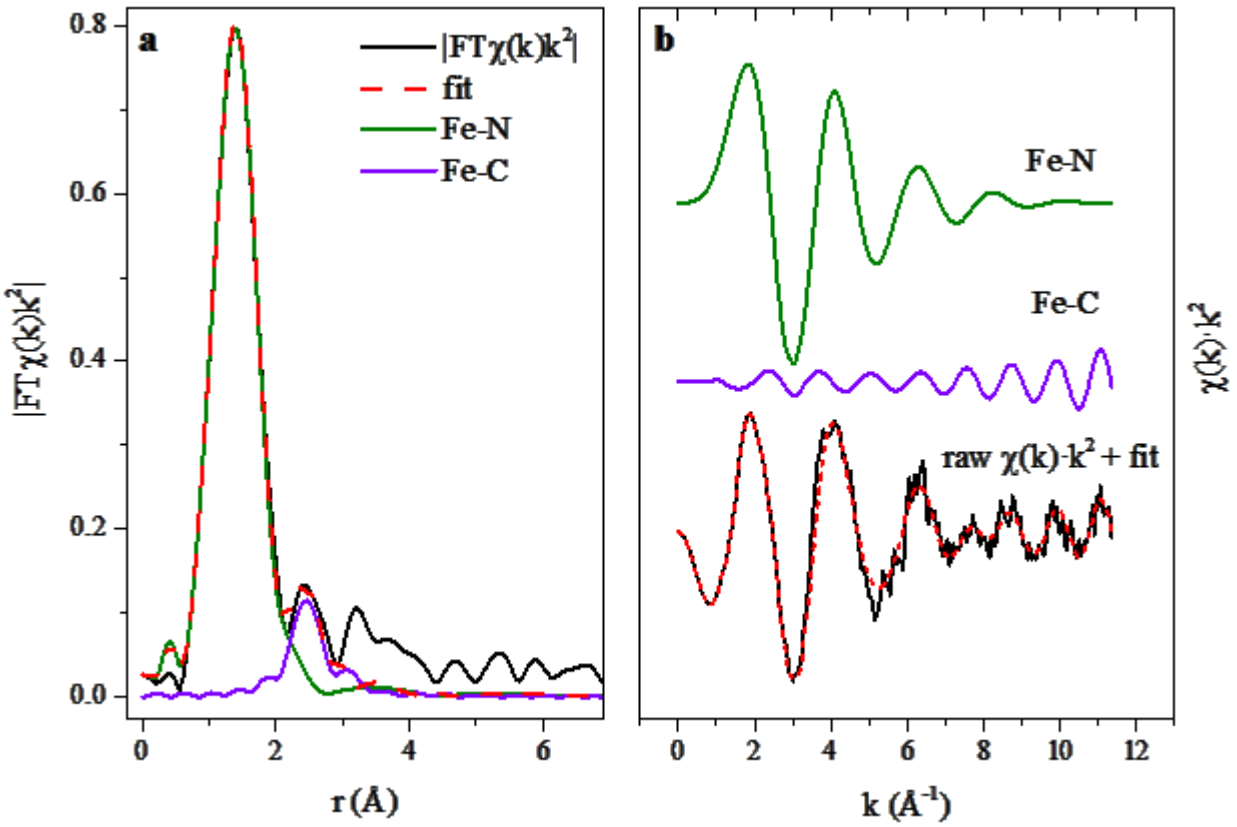

Figure S3- 13 FeK-edge EXAFS analysis as exemplified by CM sample. Panel a: the fit in the Fourier Transformed space, solid black line - raw data, dashed red line - fitting model. Panel b shows the corresponding curves in the k-space along with the Fe-N and Fe-N single scattering components.

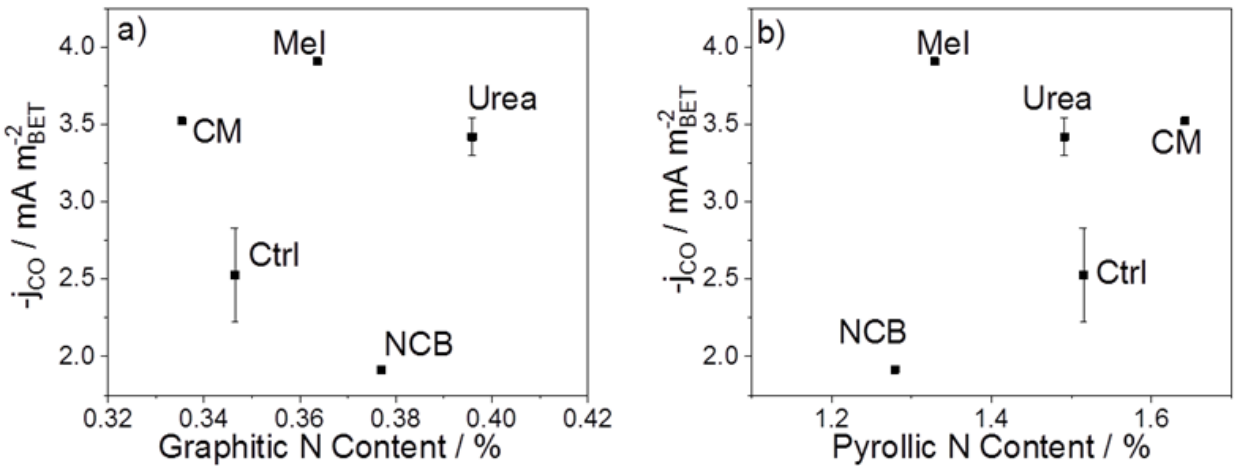

Figure S3- 14 BET normalized CO partial current density as a function of a) Graphitic N content and b) Pyrrolic N content.

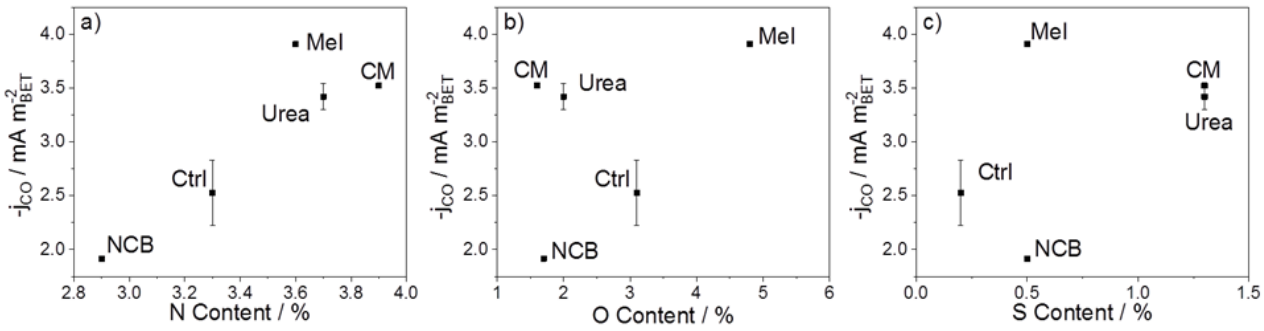

Figure S3- 15 BET-normalized CO partial current density as a function of a) Nitrogen content, b) Oxygen content and c) Sulfate Content.

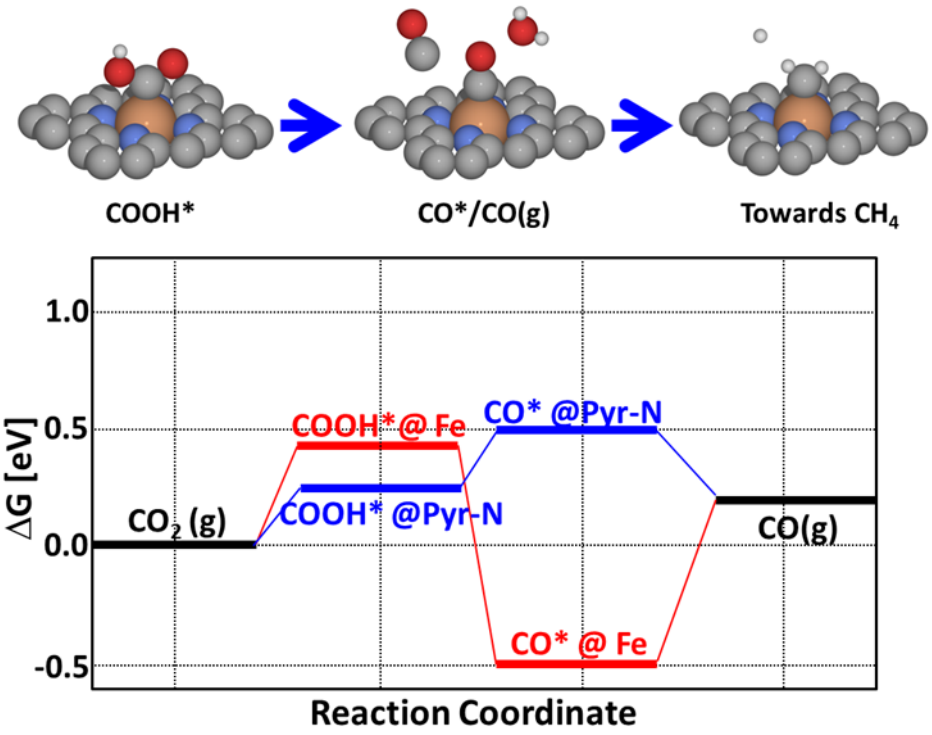

Figure S3- 16 Reaction mechanism and DFT free energy diagram of CO2RR to CO on Fe-Nx site and pyridinic nitrogen. (Free Energy data are adapted from [45] and [51])

A4. Supplementary Information to Chapter 7

Table S4- 1 Physiochemical characterization

Sample	[a)]BET surface area ($m^2\ g^{-1}$)	[b)]Double layer capacity ($\mu F\ cm^{-2}$)	[c)]Fe content (wt. %) ICP	[d)]CO uptake (mmol g^{-1}) CO-Chemisorption	[e)]N content (wt. %) element analysis
Fe-N-C	634	25.3	1.05	62	~6.5
N-C	214	72.4	0	0	~7

a) BET: N_2 ad/desorption-based surface area; b) Double layer capacity values, geometric area of each electrode is 1 cm^2 with 0.75 mg cm^{-2} catalyst loading; c) Overall metal content determined from ICP-OES measurement. d) CO uptake value examined according to CO chemisorption. e) Nitrogen content measured with elemental analysis.

X-Ray Diffraction:

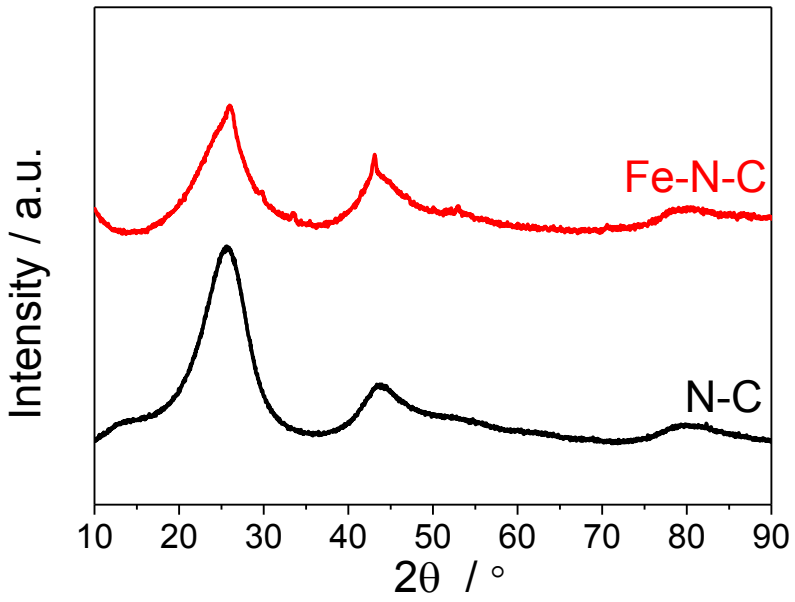

Figure S4- 1 Powder XRD patterns of Fe-N-C and N-C catalysts. Data of Fe-N-C and N-C has been reported in Figure S2-1.

TEM Images:

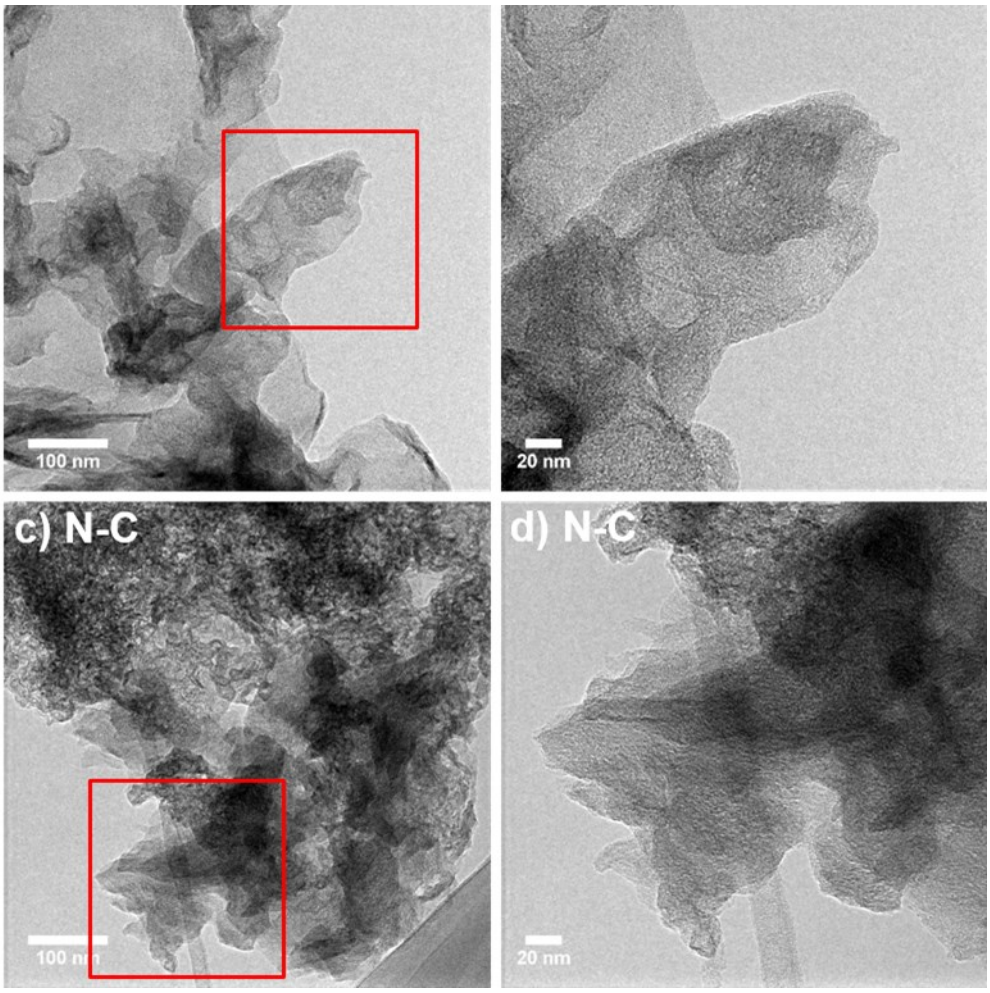

Figure S4- 2 Represented TEM images of as prepare a)-b) Fe-N-C and c)-d) N-C catalysts. Scale bar: left column 100 nm, right column 20 nm. Identical catalysts have been presented in Chapter 5.

Interfacial surface area determination: BETSA vs. ECSA

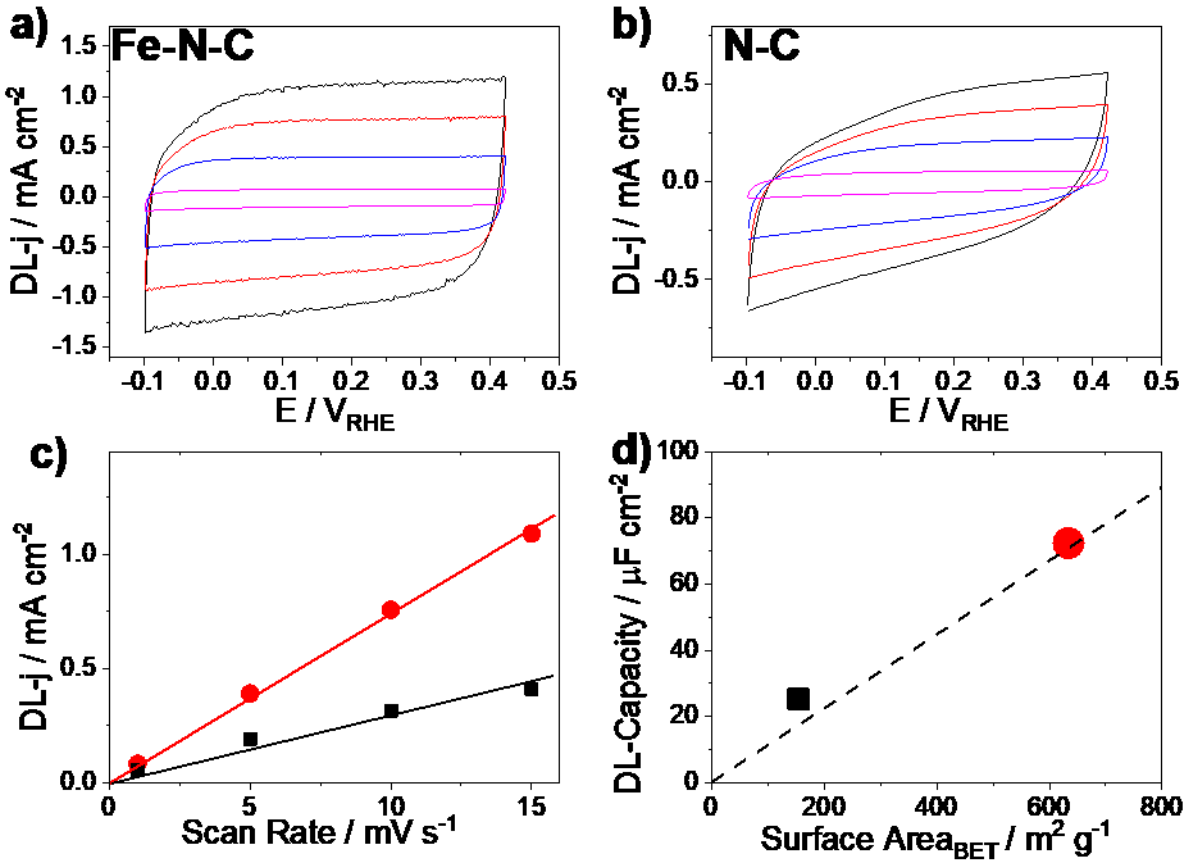

Figure S4- 3 Cyclic voltammetry of a) Fe-N-C and b) N-C catalysts conducted in N_2-saturated 0.05 M K_3PO_4 + 0.05 M H_3PO_4 solution at scan rate 15 mV s^{-1}, 10 mV s^{-1}, 5 mV s^{-1}, 1 mV s^{-1} to determine the double layer capacity. Potential was scanned between -0.1 and 0.42 V vs. RHE. c) Double layer current densities (extracted at +0.16 V_{RHE}) on Fe-N-C and N-C catalysts at each scan rate. d) Correlation of double layer capacity (ECSA) and the N_2 adsorption derived BET surface area (BETSA). Catalysts loading: 0.75 mg cm^{-2} on glassy carbon.

Table S4- 2 Electrolysis parameters in presence of various reactants

Electrolysis	Electrolyte	Reactant	Tot. time	Ionomer	Products
Long-term CO_2RR	0.1 M $KHCO_3$ (pH: 6.8)	20 ccm CO_2 flow	1020 min	Selemion	CO, CH_4, CH_3OH, CH_2O
Long-term CO_2RR	0.05 M KH_2PO_4 + 0.05 M K_2HPO_4 (pH: 6.9)	20 ccm CO flow	480 min	Selemion	CH_4, CH_3OH, CH_2O
CO_2RR	0.05 M KH_2PO_4 + 0.05 M K_2HPO_4 (pH: 6.4)	20 ccm CO_2 flow	75 min	Nafion 117	CO, CH_4
CORR	0.05 M KH_2PO_4 + 0.05 M K_2HPO_4 (pH: 6.9)	20 ccm CO flow	75 min	Nafion 117	CH_4
CH_2ORR	0.05 M KH_2PO_4 + 0.05 M K_2HPO_4 (pH: 6.9)	1 mM CH_2O 6 ccm N_2 flow	75 min	Nafion 117	CH_4
Methanol RR	0.05 M KH_2PO_4 + 0.05 M K_2HPO_4 (pH: 6.9)	1 mM CH_3OH 6 ccm N_2 flow	75 min	Nafion 117	N/A
Formate RR	0.05 M KH_2PO_4 + 0.05 M K_2HPO_4 (pH: 6.7)	1 mM HCOOH 6 ccm N_2 flow	75 min	Nafion 117	N/A

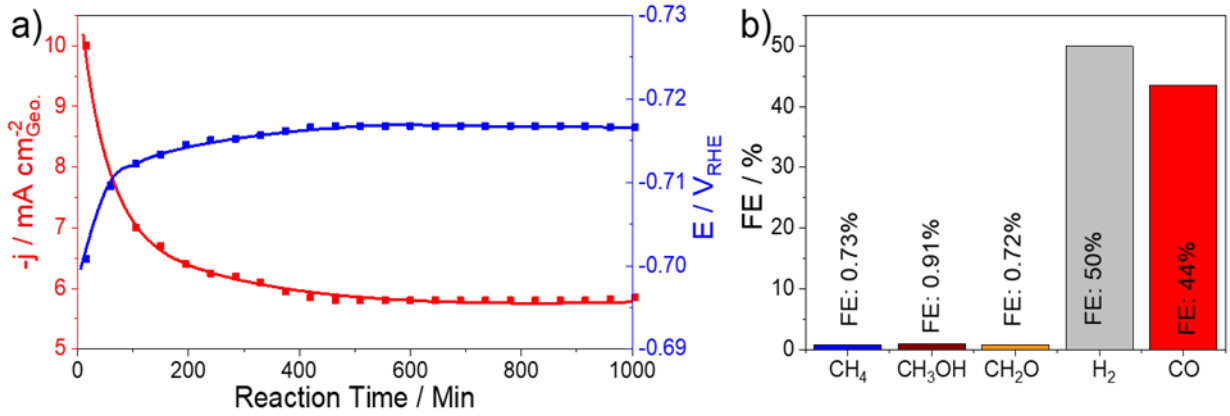

Figure S4- 4 Catalytic performance of long term CO_2RR on Fe-N-C catalyst in CO_2 purged 0.1 M $KHCO_3$. a) Geometric working current density and applied iR-free potential as a function of reaction time. b) Faradaic efficiency of measured products. Catalyst loading: 0.75 mg cm^{-2} on glassy carbon electrode. Measurement parameters see Table S4-2.

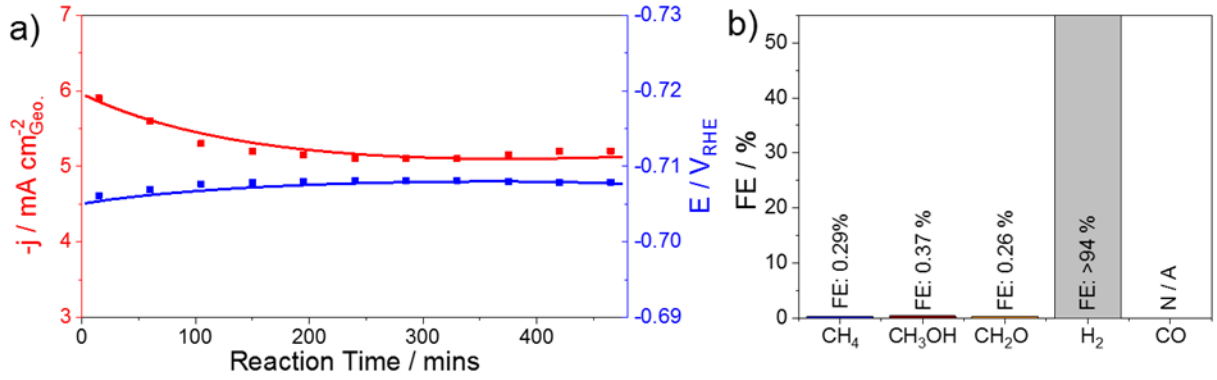

Figure S4- 5 Catalytic performance of long term CORR on Fe-N-C catalyst in CO purged phosphate solution with neutral initial pH value. a) Geometric working current density and applied iR-free potential as a function of reaction time. b) Faradaic efficiency of measured products. Catalyst loading: 0.75 mg cm^{-2} on glassy carbon electrode. Measurement parameters see Table S4-2.

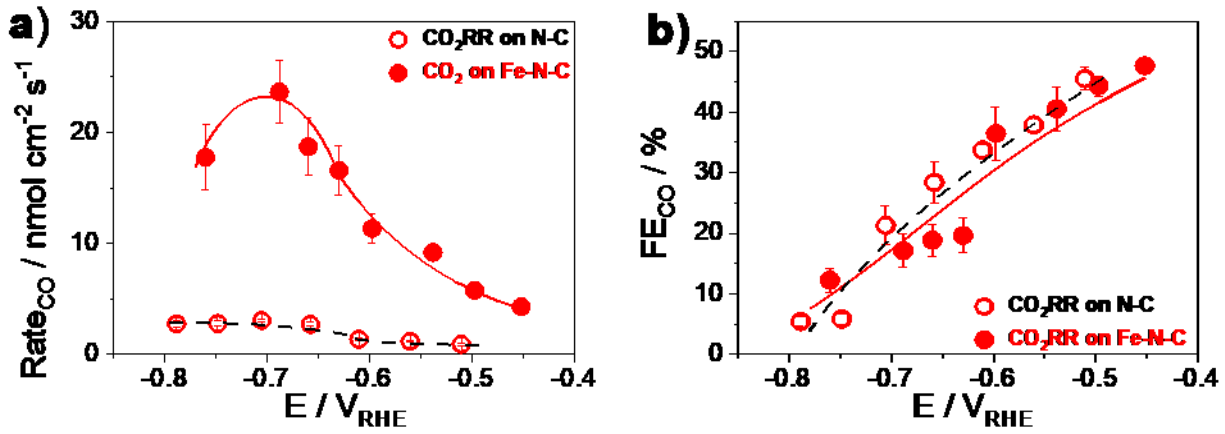

Figure S4- 6 Products distribution as a function of applied iR-free potentials on Fe-N-C and N-C catalysts. a) CO production rate and b) faradaic efficiency during CO_2 reduction. Data points are standard Mean and Error obtained from 15 min, 45 min and 75 min of the bulk electrolysis. Catalyst loading: 0.75 mg cm^{-2} on glassy carbon electrode.

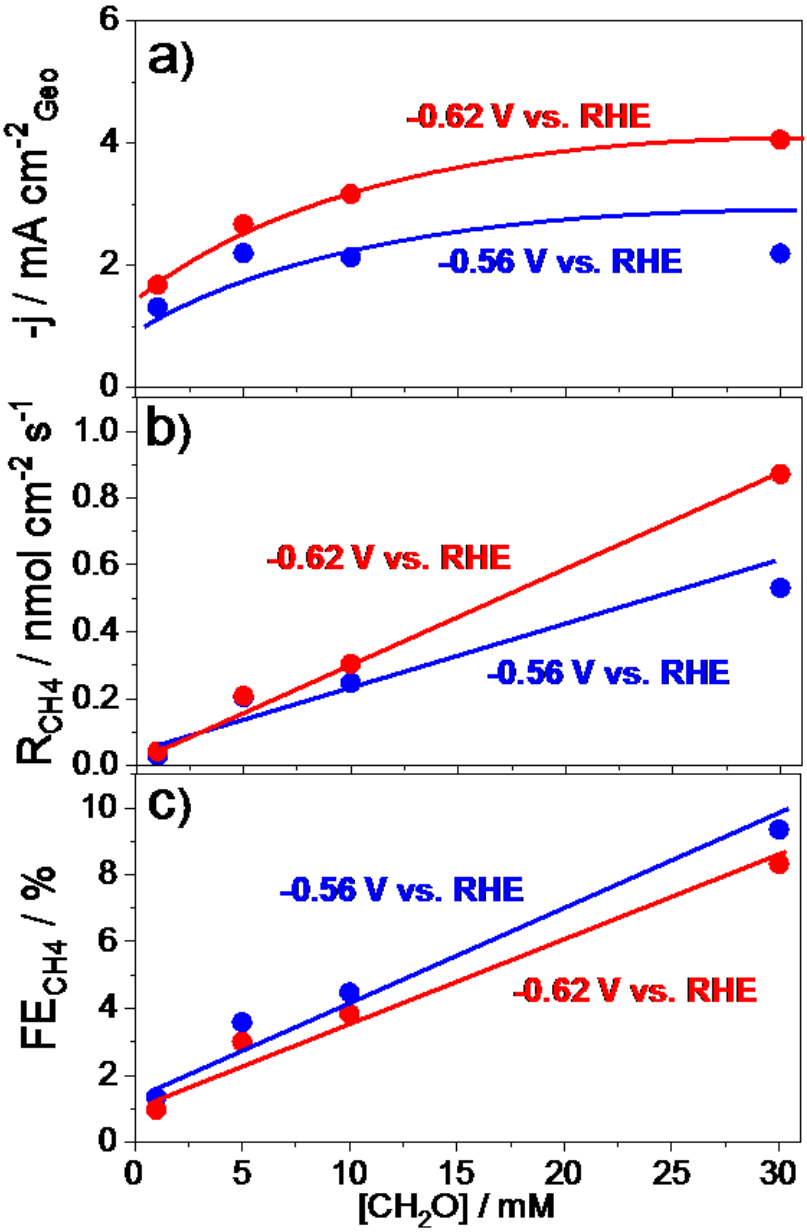

Figure S4- 7 Catalytic performance of CH_2O reduction on Fe-N-C catalyst with different initial CH_2O concentrations. a) Geometric current densities, b) CH_4 production rate and c) faradaic efficiency. Data are averages over 75 min electrolysis. Reaction conditions: 6 ccm N_2 purged 0.05 M K_3PO_4 + 0.05 M H_3PO_4 electrolyte in presence of CH_2O. Catalyst loading: 0.75 mg cm^{-2} on glassy carbon.

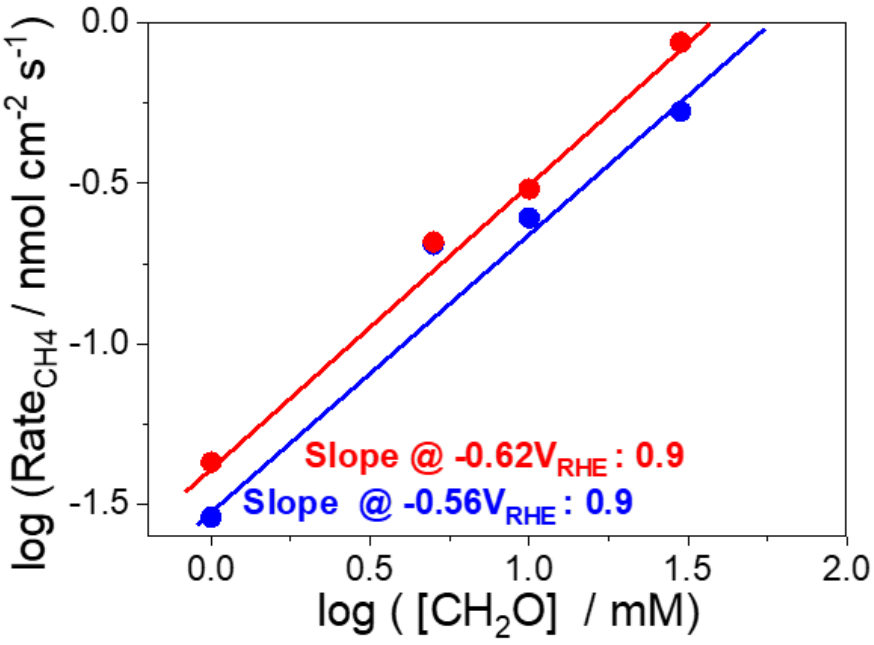

Figure S4- 8 Logarithm of CH_4 formation rate during CH_2ORR versus Logarithm of the CH_2O concentration in phosphate neutral buffer solution.

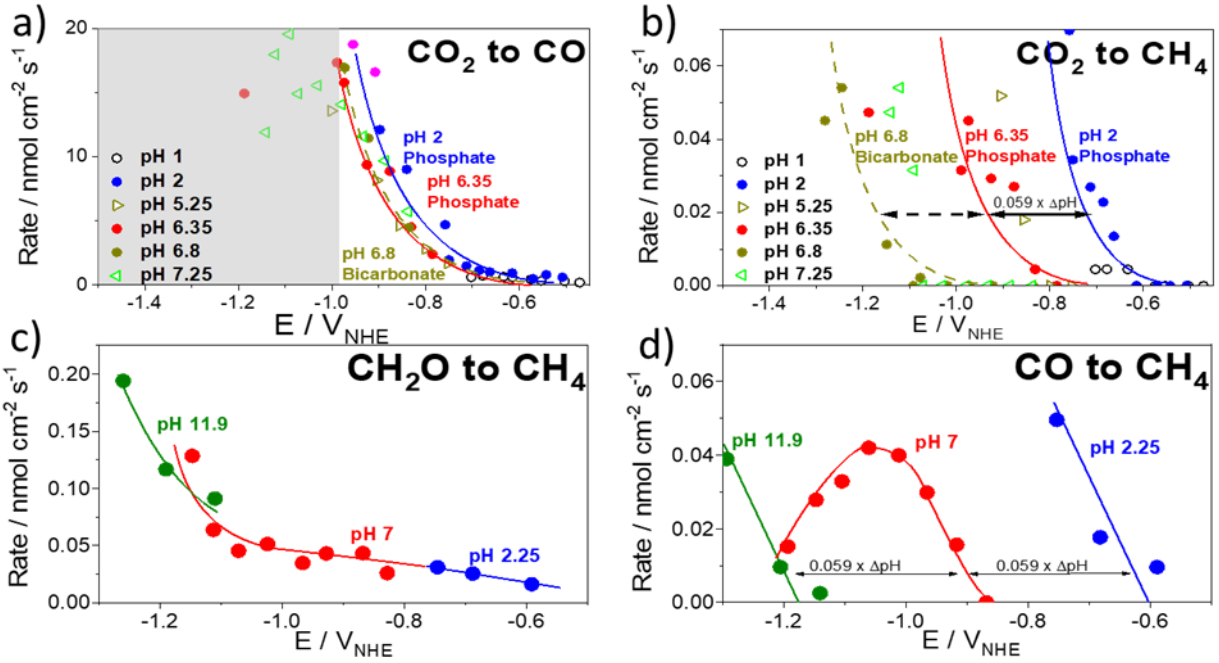

Figure S4- 9 Reaction rate of a) CO_2 reduction to CO, b) CO_2 reduction to CH_4, c) CH_2O reduction to CH_4, and d) CO reduction to CH_4 as a function of iR-free potential in NHE scale. Data in a) and b) are adapted from the work.[116]

Table of figures and schemes

Table of tables

List of Abbreviations

CO_2RR	(Electrochemical) CO_2 reduction reaction	HER	Hydrogen reduction reaction
atm	atmospheres	(P)XRD	(Powder) X-ray diffraction
M-N-C	Metal-Nitrogen-Carbon	H_{upd}	Hydrogen underpotential deposition
EA	Elemental analysis	ICP OES	Inductively Coupled Plasma Optical Emission Spectrometry
CE	Counter electrode	WE	Working electrode
REF	Reference electrode	NHE	Normal hydrogen electrode
RHE	Reversible hydrogen electrode	LSV	Linear sweep voltammertry
CA	Chronoamperometry	GDE / L	Gas diffusion electrode / layer
DFT	Density functional theory	MEA	Membrane electrode assembly
h	hours	min	minutes
ECSA	Electrochemical active surface area	DL	Double layer capacity
BET	Brunauer-Emmett-Teller	ORR	Oxygen reduction reaction
EDX	Energy dispersive X-ray spectroscopy	PEIS	Potentiostatic electrochemical impedance spectroscopy
GC-plate	Glassy carbon plate	(Non)-PGM	(Non)- Precious group metal
TEM	Transmission electron microscopy	HRTEM	High resolution TEM
XPS	X-ray photoelectron spectra	XAS	X-ray absorption spectra
XANES	X-ray absorption near edge spectroscopy	EXAFS	Extended X-ray absorption fine structure
QS	Quadrupole splitting	TPD	Temperature programmed desorption
PCET	Proton coupled electron transfer	GC	Gas chromatograph
HPLC	High performance liquid chromatograph	MFC	Micro flow cell
SEM	Scanning electron microscopy	RT	Room temperature
TOF	Turn over frequency	FE	Faradaic efficiency
iR	Current times resistance (ohmic drop)		

List of Chemicals

Name	Acronym	Purity/Concentration	Supplier
Ultra-pure water	Milli-Q water	16.8 MΩ cm	-
Methanol	MeOH	anhydrous, 99.9 %	Alfa Aesar
Ethanol	EtOH	100 %	VWR Chemicals
Isopropanol	iPrOH	100 %	VWR Chemicals
n-Propanol	nPrOH	100 %	VWR Chemicals
Nafion	-	5 wt%	Sigma Aldrich
Nafion membrane	-		Sigma Aldrich
Selemion membrane	-		AGC Eng. Co.
Nickel chloride hexahydrate	$NiCl_2 \cdot 6H_2O$	99.5 %	Sigma Aldrich
Iron chloride hexahydrate	$FeCl_3 \cdot 6H_2O$	99.5 %	Sigma Aldrich
Perchloric acid	$HClO_4$	70 % conc., 99.999 % trace metal bases	Sigma Aldrich
Sulfuric acid	H_2SO_4	95.0 %	VWR Chemicals
Hydrochloric acid	HCl	37.0 %	VWR Chemicals
Nitric acid	HNO_3	69.0 %	Merck
Phosphoric acid	H_3PO_4	85 wt%	Sigma Aldrich
Potassium hydroxide	KOH	99.99%	Sigma Aldrich
Potassium bicarbonate	$KHCO_3$	99.5%	Sigma Aldrich
Potassium dibasic phosphate	K_2HPO_4	99.95%	Sigma Aldrich
Potassium monobasic phosphate	KH_2PO_4	99.95%	Sigma Aldrich
Ammonium peroxodisulfate	$(NH_4)_2S_2O_8$	>98%	Merck
Formic acid	HCOOH	>95%	Sigma Aldrich
Formaldehyde	CH_2O	37wt %	Merck
Carbon dioxide	CO_2	99.999 %	Air Liquide
Hydrogen	H_2	99.999 %	Air Liquide
Carbon monoxide	CO	99.997 %	Air Liquide
Nitrogen	N_2	99.999 %	Air Liquide
Oxygen	O_2	99.998 %	Air Liquide
Argon	Ar	99.999 %	Air Liquide
Helium	He	99.999 %	Air Liquide

List of Publications during Ph.D. study

- ***Page 22-35, as Chapter 4 of this dissertation:***

Wen Ju, Alexander Bagger (co-first), Guangping Hao, Ilya Sinev, Ana Sofia Varela, Volodymyr Bon, Beatriz Roldan Cuenya, Stefan Kaskel, Jan Rossmeisl, and Peter Strasser, Understanding activity and selectivity of metal-nitrogen-doped carbon catalysts for electrochemical reduction of CO_2, Nature Communications, 2017, 8, 944.

- ***Page 36-46, as Chapter 5 of this dissertation:***

Tim Möller, Wen Ju (co-first), Alexander Bagger, Xingli Wang, Fang Luo, Trung Ngo Thanh, Ana Sofia Varela, Jan Rossmeisl, and Peter Strasser, Efficient CO_2 to CO Electrolysis on Solid Ni-N-C Catalysts at Industrial Current Densities, Energy & Environmental Science, 2019.

- ***Page 47-59, as Chapter 6 of this dissertation:***

Nathaniel D Leonard, Wen Ju (co-first), Ilya Sinev, Julian Steinberg, Fang Luo, Ana Sofia Varela, Beatriz Roldan Cuenya, and Peter Strasser, The chemical identity, state and structure of catalytically active centers during the electrochemical CO_2 reduction on porous Fe–nitrogen–carbon (Fe–N–C) materials, Chemical Science, 2018, 9, 5064–5073.

- ***Page 60-73, as Chapter 7 of this dissertation:***

Wen Ju, Alexander Bagger (co-first), Xingli Wang, Yulin Tsai, Fang Luo, Huan Wang, Tim Möller, Jan Rossmeisl, Ana Sofia Varela, and Peter Strasser, Unraveling mechanistic reaction pathways of the electrochemical CO_2 reduction on Fe-N-C single site catalysts, Submitted to ACS Energy Letters, accepted, 2019.